Master Thesis

Study of Light-Induced Phase Segregation in Mixed-Halide Perovskites

Emmanouil Fragkioudakis

Supervisor: Prof. Nikos Pelekanos

University of Crete
Department of Physics

Heraklion, September 2022

Abstract

Mixed halide perovskites are ideal materials for tandem solar cells (solar energy conversion), but they suffer from detrimental light-induced phase segregation, which can affect their optoelectronic performance. In the course of this thesis, the light-induced phase segregation in a $FA_{0.5}MA_{0.5}Pb(I_{0.5}Br_{0.5})_3$ thin perovskite film was investigated. Specifically, the time evolution of the emission spectra was studied at different laser irradiation conditions, such as excitation intensity (> 1 W/cm^2) and irradiation time. Optical spectroscopy measurements revealed the co-existence of three perovskite phases, a mixed halide phase, a bromide-rich phase, and an iodide-rich phase within the film, due to the phase segregation effect under light excitation. It was observed that at short irradiation times the photoluminescence (PL) from the iodide-rich phase dominated the PL spectra, while at long irradiation times its PL was significantly reduced and the PL from the bromide-rich phase was intensified. These variations in PL intensity at different irradiation times could be explained by effects such as, the accumulation of charge carriers at the potential minimum (the lowest energy gap), PL quenching and band filling. The light-induced phase segregation of $FA_{0.5}MA_{0.5}Pb(I_{0.5}Br_{0.5})_3$ perovskite was found to be suppressed, compared to other perovskite materials such as $MAPb(I_{0.5}Br_{0.5})_3$. In addition, it was found that strong PL quenching can affect the reversibility of the phase segregation, which is evidence for iodine expulsion (loss of iodine). Finally, the charge carrier recombination dynamics during phase segregation at different excitation intensities was investigated by time-resolved photoluminescence measurements.

Περίληψη

Οι περοβσκίτες μικτής περιεκτικότητας αλογόνου είναι ιδανικά υλικά για ηλιακές κυψελίδες πολλαπλής επαφής (μετατροπή ηλιακής ενέργειας), αλλά υποφέρουν από επιζήμιο οπτικά επαγόμενου διαχωρισμό φάσης, το οποίο μπορεί να επηρεάσει την οπτοηλεκτρονική τους απόδοση. Στο πλαίσιο της παρούσας διατριβής, διερευνήθηκε ο οπτικά επαγόμενος διαχωρισμός φάσης σε ένα $FA_{0.5}MA_{0.5}Pb(I_{0.5}Br_{0.5})_3$ λεπτό υμένιο περοβσκίτη. Συγκεκριμένα, μελετήθηκε η χρονική εξέλιξη των φασμάτων εκπομπής σε διαφορετικές συνθήκες ακτινοβόλησης με λέιζερ, όπως ένταση διέγερσης (> 1 W/cm^2) και χρόνος ακτινοβόλησης. Μετρήσεις οπτικής φασματοσκοπίας αποκάλυψαν τη συνύπαρξη τριών φάσεων περοβσκίτη, μια φάση μικτής περιεκτικότητας αλογόνου, μια φάση πλούσια σε βρώμιο και μια φάση πλούσια σε ιώδιο εντός του υμενίου, εξαιτίας του φαινομένου διαχωρισμού φάσης υπό διέγερση φωτός. Παρατηρήθηκε ότι σε μικρούς χρόνους ακτινοβόλησης η φωτοφωταύγεια από την πλούσια σε ιώδιο φάση κυριαρχούσε στα φάσματα φωτοφωταύγειας, ενώ σε μεγάλους χρόνους ακτινοβόλησης η φωτοφωταύγεια της μειώθηκε σημαντικά και η φωτοφωταύγεια από την πλούσια σε βρώμιο φάση ενισχύθηκε. Αυτές οι μεταβολές στην ένταση της φωτοφωτάγειας σε διαφορετικούς χρόνους ακτινοβόλησης θα μπορούσαν να εξηγηθούν από φαινόμενα όπως η συσσώρευση φορέων φορτίου στο ελάχιστο του δυναμικού (το χαμηλότερο ενεργειακό χάσμα), απόσβεση της φωτοφωτάγειας και πλήρωση ζωνών. Ο οπτικά επαγόμενος διαχωρισμός φάσης του περοβσκίτη $FA_{0.5}MA_{0.5}Pb(I_{0.5}Br_{0.5})_3$ βρέθηκε να είναι κατεσταλμένος, σε σύγκριση με άλλα περοβσκιτικά υλικά όπως το $MAPb(I_{0.5}Br_{0.5})_3$. Επιπλέον, διαπιστώθηκε ότι η ισχυρή απόσβεση της φωτοφωταύγειας μπορεί να επηρεάσει την αναστρεψιμότητα του διαχωρισμού φάσης, γεγονός που αποτελεί αποδεικτικό στοιχείο για αποβολή ιωδίου (απώλεια ιωδίου). Τέλος, η δυναμική της επανασύνδεσης φορέων φορτίου κατά τη διάρκεια του διαχωρισμού φάσης σε διαφορετικές εντάσεις διέγερσης διερευνήθηκε με χρονοεξαρτόμενες μετρήσεις φωτοφωταύγειας.

Acknowledgements

I want to thank my supervisor, Professor Nikos Pelekanos, for the extensive help, the useful instructions and meetings, and also for giving me this project. I also want to thank all the technical staff of the Microelectronics Group at the ITE-FORTH Institute, especially Mrs Maria Androulidaki, and the PhD candidates Manolis Manidakis, Nikos Hatzarakis, and Christine Saitanidou, for their contributions to this work. I am grateful to Manolis Manidakis, who fabricated and let me borrow the perovskite thin film for investigation, and to Mrs Maria Androulidaki and Nikos Hatzarakis for their intense support in the experimental work of this project.

Contents

Chapter 1

Introduction

Organic-inorganic hybrid mixed halide perovskites are potential candidates for low cost, efficient and high performance photovoltaic devices. Due to their tunable band gaps (i.e for $CH_3NH_3Pb(I_{1-x}Br_x)_3$ perovskites the energy band gap can be tuned from 1.6 to 2.3 eV at room temperature by varying the halide composition x, $0 \leq x \leq 1$), the long carrier lifetimes (several ns to a few μs), the long carrier diffusion lengths, the high photoluminescence quantum yields, the large absorption coefficients ($10^4 - 10^5$ cm^{-1}), the excellent defect tolerance, mixed halide perovskites can efficiently harvest the entire solar spectrum, leading to certified power conversion efficiencies (PCEs) which to date exceed 22% [1–8]. Noteworthy, mixed halide perovskites have already been employed for light-harvesting layers in tandem solar cells [5–7, 9].

Despite the unique properties and features, the progress in efficiency and other achievements, mixed halide perovskites exhibit long-term instability issue. In particular, moisture can lead to degradation of the perovskite through a series of chemical reactions [10]. In addition, photo-instabilities occur when the mixed halide perovskites are exposed to visible light irradiation, resulting in deformation of the mixed halide perovskite and degradation of the perovskite-based photovoltaic devices performance [11–24].

Through optical and structural measurements, this phenomenon has been attributed to light-induced halide phase segregation, which originates from ion migration and causes spectral shifts in the absorption and emission, indicating the deformation of the mixed halide phase and the formation of two new phases (a phase rich in the first compound and a phase rich in the second compound) within the parent mixed halide perovskite [16–22, 25–30].

Remarkably, this phenomenon is reversible. With the removal of the light

source, the partial segregated perovskite slowly recovers to its initial mixed phase [17].

Chapter 2

Organic-Inorganic Halide Perovskites

The chemical formula of perovskites is ABX_3 where A contains one of MA^+,FA^+,Cs^+ cations, with methylammonium MA^+=$CH_3NH_3{}^+$ and formamidinium FA^+=$CH(NH_2)_2^+$, B=Pb^{2+} or Sn^{2+} cation and X=I^-,Br^-,Cl^- where X is a halogen anion. For these B cations and X anions, A should be one of the cations mentioned above or a mix of them for double and triple cation perovskites (and not, for example Na or K) in order to achieve the desired tolerance factor to form a stable perovskite structure with phase stability at room temperature [31–34]. For the formation of a stabilized perovskite structure, the tolerance factor (t) should be within the range 0.8<t<1.0 and is given by:

$$t \;=\; \frac{R_A + R_X}{\sqrt{2}\cdot(R_B + R_X)} \tag{2.1}$$

where R_A,R_B and R_X are the radius of A,B cations and X anion, respectively. Usually double (or triple) cation halide perovskites are used by mixing those A cations, with X containing two of the three anions mentioned above in different fractions, hence the name mixed-halide perovskites. The crystalline structure of perovskites with chemical formula ABX_3 is depicted in Figure 2.1 which contains the three possible phases of a perovskite material. Organic-inorganic halide perovskites should appear in any of the three phases at room temperature, depending on the tolerance factor. By varying the temperature, halide perovskites can undergo phase transitions [35, 36].

The A cation is located at the centre of the structure and is surrounded by

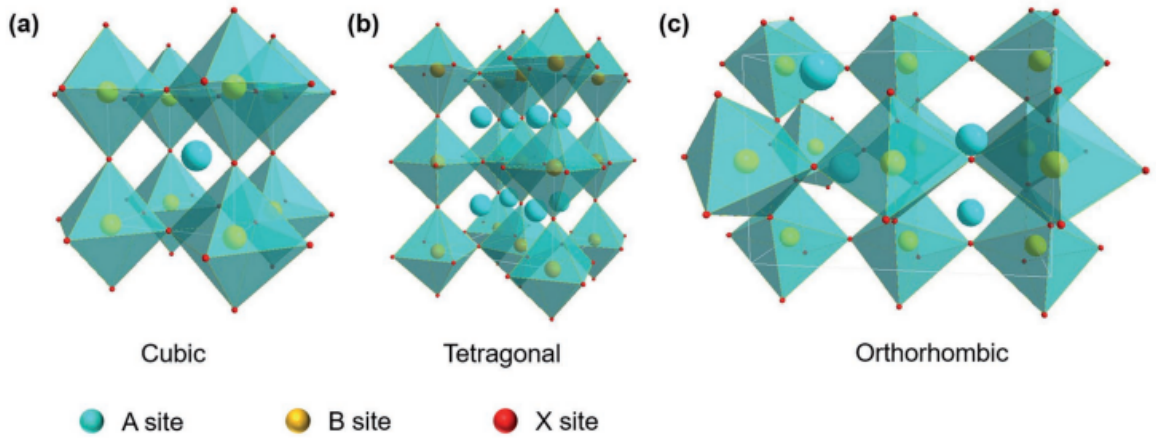

Figure 2.1: The crystal structures of perovskites for the three different phases,whence A,B and X ions are given above. *Source of the Figure :* [36]

eight corner-sharing [BX_6] octahedra with the B cation in the center and the 6 anions at the corners. Note that $MAPbI_3$ has a tetragonal lattice structure, $MAPbBr_3$ has a cubic crystal structure and the $CsPbI_3$ perovskite has an orthorombic structure, at room temperature [35, 37]. Finally, for x>0.2 the $MAPb(I_{1-x}Br_x)_3$ perovskites undergo a tetragonal-to-cubic phase transition, which may play a critical role in phase segregation and which will be revealed later on [17, 38].

2.1 Optical and Structural Properties of $APb(I_{1-x}Br_x)_3$ Perovskites

Absorption and X-ray diffraction (XRD) measurements demonstrate the tunable optical and structural properties of this class of materials.

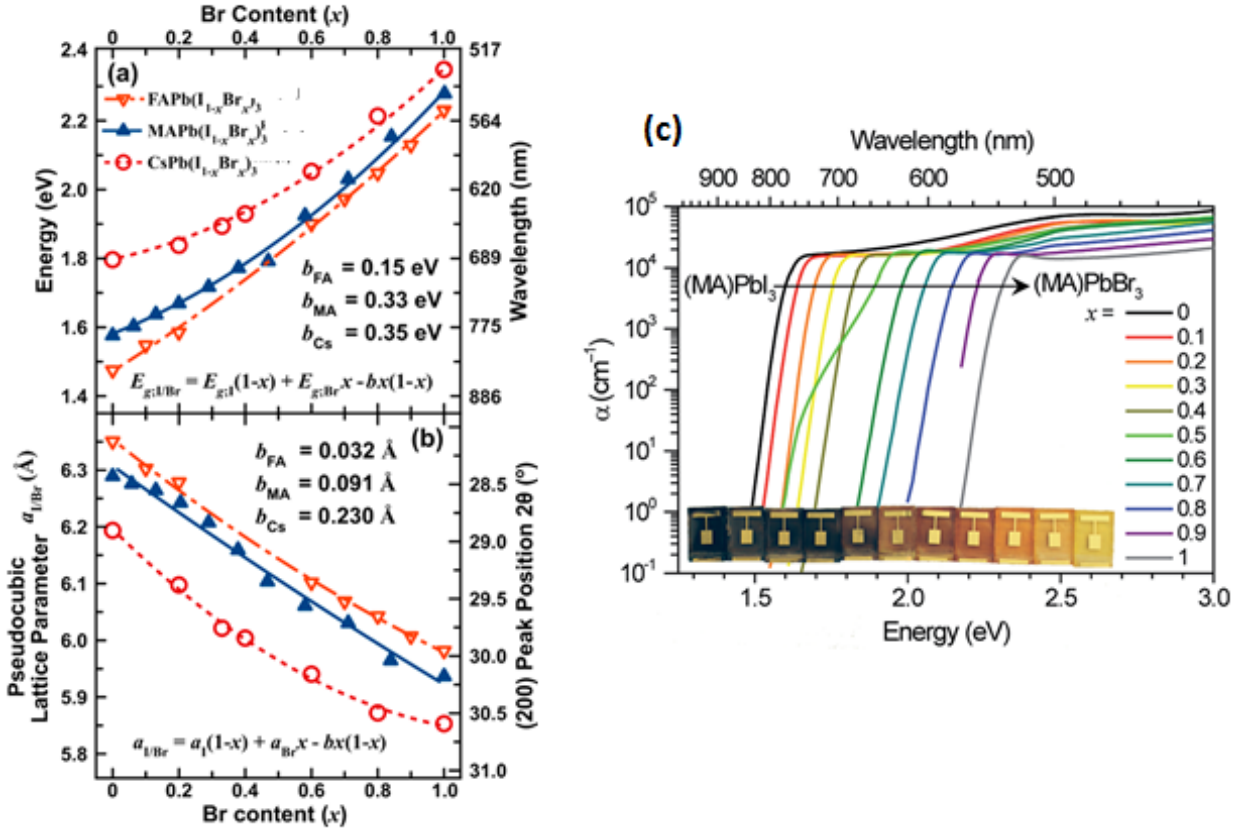

Figure 2.2: a) The energy band gap Eg(x) versus Br composition x and b) the pseudocubic lattice constant and the (200) peak position versus Br composition x, for $FAPb(I_{1-x}Br_x)_3$ (orange triangles), $MAPb(I_{1-x}Br_x)_3$ (blue triangles), $CsPb(I_{1-x}Br_x)_3$ (red circles) at room temperature. c) The absorption coefficient of $MAPb(I_{1-x}Br_x)_3$ versus energy(eV) by varying the Br composition x, at room temperature. c)Inset: photograph of $MAPb(I_{1-x}Br_x)_3$ devices for $0 \leq x \leq 1$ (from left to right). *Source of the Figure 2.2 a),b)* : [25]. *Source of the Figure 2.2 c)* : [17].

The broad range of values for the energy gap by varying the concentration of bromide x, in Figure 2.2a, combined with the high absorption coefficient values for a $MAPb(I_{1-x}Br_x)_3$ thin film shown in Figure 2.2c and the long carrier lifetimes, suggest that these materials could be excellent candidates for light-harvesting layers in solar cells. The respective energy band gap for A=FA^+, A=MA^+, and A=Cs^+ cations varies between x=0 and x=1 from 1.48eV to 2.28eV, 1.58eV to 2.38eV, and 1.80eV to 2.35eV, respectively [6, 17, 33]. The origin of the high energy differences is related to changes in average Pb-X bond distance, which is dictated by the ionic radius of the halide species [25, 39]. The bromide ion has a lower ionic radius than the iodide, thus the average bond distance of Pb-X reduces as x increases, leading to lattice contraction (smaller lattice constant) and a higher energy band gap, as one can confirm from Figure 2.2a,b.

Chapter 3

Effects of Light-Induced Phase Segregation on the Optical Response of Mixed Halide Perovskites

Light-induced phase segregation is a phenomenon which is often found in solid solutions or semiconductor alloys (or in other mixtures) of two components (A_xB_{1-x}) and has the ability to demix an alloy, which is initially in a stable mixed state at room temperature, by using light excitation. Due to the demixing, two new phases are formed, a phase rich in the first element(A) and a phase rich in the second chemical element(B) (instead of chemical elements, could be also compounds). The phenomenon arises from variations in the free energy of the system, specifically light excitation can increase the free energy of the system by providing the requisite energy to overcome the kinetic barriers for ion migration, leading to phase separation of the mixed phase into two phases whose exact compositions are defined by thermodynamics. The same procedure occurs also in our case when the mixed halide perovskite thin film is exposed to light illumination, and one way to track the phenomenon and its effects is via optical measurements(absorption,emission, etc) [16–22, 24, 26, 30, 38].

Moreover, halide phase segregation can occur even via current injection, external electric fields and inert build-in potentials in devices [11, 13, 40]. In our work, we examine only the mixed halide phase segregation induced by light soaking.

3.1 Spectral Changes in Emission

Primarily, Figure 3.1a depicts the time evolution of the emission (photoluminescence versus time) from a $MAPb(I_{0.5}Br_{0.5})_3$ thin film under continuous wave (CW) illumination with excitation intensity and excitation wavelength of 20 $mW{\cdot}cm^{-2}$ ($\sim$ 1/5 of the Sun's intensity) and 405nm, respectively [22].

The initial emission peak was at roughly 660nm (1.88eV) consistent with the equation in Figure 2.2a for x=0.5 [38]. We can observe (Figure 3.1a) that the emission from the mixed state ($\sim$ 660nm) reduces with time and two new emission peaks are forming with sufficiently different intensities, one peak at roughly 733nm which is consistent with emission from x$\approx$0.2 $MAPb(I_{0.8}Br_{0.2})_3$ film and one more peak at roughly 530nm. The two new features in the emission spectra denote the formation of I-rich and Br-rich phases within the film. The emission of the I-rich phase dominates in the emission spectra due to the favourable low energy band gap which behave as a trap for carriers who finally recombine there [17, 22].

In order to confirm that the observed changes in the $MAPb(I_{1-x}Br_x)_3$ perovskites do not occur due to the local heat, wide-angle X-ray scattering (WAXS) experiment were conducted and the results showed zero spectral shifts [30]. Earlier studies have shown that the final I-rich phase of phase segregated $MAPb(I_{1-x}Br_x)_3$ films is always consistent with emission from x$\approx$0.2 film, regardless of the initial concentration x of the films [17]. Specifically, a final emission at 730-760 nm has been universally observed [11, 17–22, 24, 26, 27, 30, 38, 41, 42]. This is a significant observation which the following models for phase segregation will try to rationalize. Figure 3.1c shows that the I-rich phase, even at low volume fractions can dominate the photoluminescence spectra due to the diffusion of the photo-generated carriers into these I-rich inclusions. The photo-generated carriers relax into lower energy states and facilitate radiative electron-hole recombination from the lowest band gap domains. The overall increase in emission spectra is due to the high photoluminescence efficiency of these I-rich inclusions in comparison to the rest phases (Br-rich and mixed phase) of the film [17]. At last, by plotting the intensity of the I-rich phase (from the emission spectrum) with

time, one can obtain the segregation rate $k_{forward,em}$ (s^{-1}).

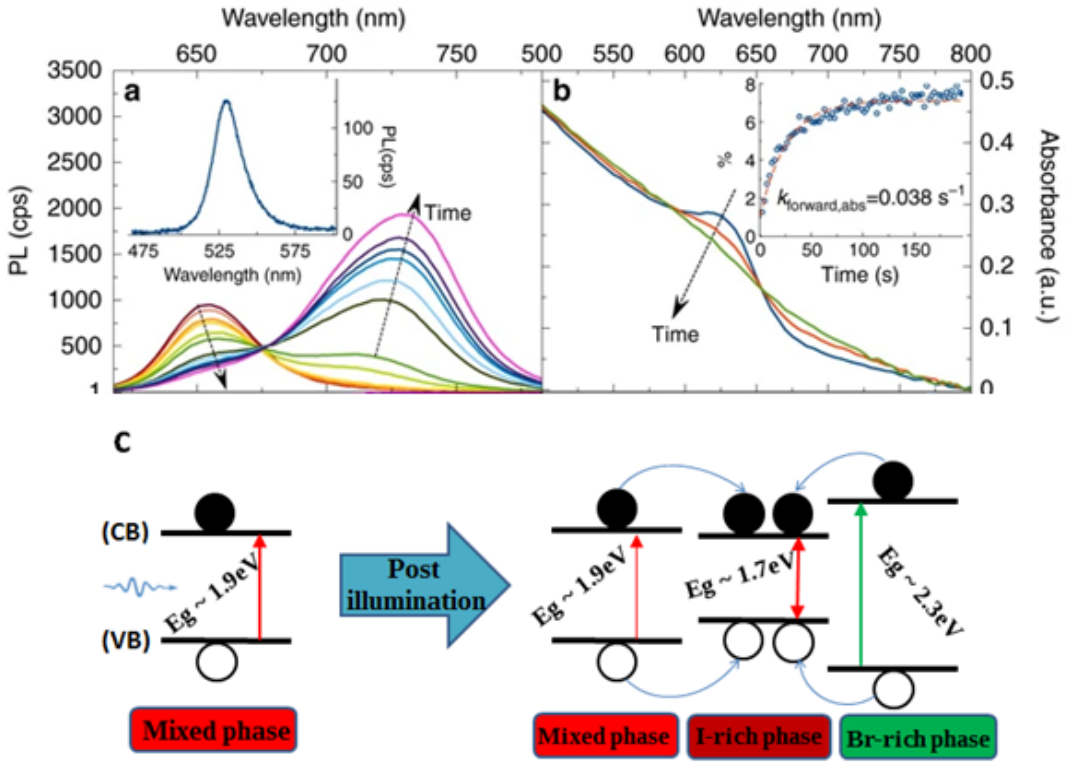

Figure 3.1: a) Photoluminescence versus wavelength for different time intervals over a period of 3sec for a $MAPb(I_{0.5}Br_{0.5})_3$ thin film under (CW) excitation with I_{exc}=20mW/cm^2 at λ=405nm. Inset: Emission peak at $\lambda\sim$530nm. b) The absorption spectra of $MAPb(I_{0.5}Br_{0.5})_3$ at different times of illumination with CW excitation (I_{exc}=25mW/cm^2, λ=405nm). The different times of irradiation are 0min(blue), 1min(red) and 30min(green). Inset: Absorption-based phase separation rate from absorption changes at λ=720nm where the dashed red line represents an exponential fit to the data. c) Schematic illustration of phase segregation caused by photo-generated charge carriers (black circles for electrons and white circles for holes), showing the co-existance of three different phases within the film, with their energy band gaps pointing out the preferred emission from I-rich phase(x$\approx$0.2) domains. *Source of the Figure 3.1 a),b)* : [22].

3.2 Spectral Changes in Absorption

The halide phase segregation can also be tracked by the changes in the absorption of illuminated MAPb$(I_{1-x}Br_x)_3$ thin films. In order to obtain Figure 3.1b, a (CW) laser with λ=405nm and I_{exc}=25W/cm^2 was used. Hence it depicts the changes in absorption at different irradiation times (before, during and after CW illumination) in a MAPb$(I_{0.5}Br_{0.5})_3$ thin film [22]. The first observation is that during 30 minutes of (CW) irradiation, the absorbance changed slightly and not in the same dramatic fashion that emission spectra did. Furthermore, one can observe the decreased band edge absorption at around $\sim$ 630nm and also the growth of a tail at around $\sim$ 700nm. The observed shifts in absorption wavelengths, compared to those in emission wavelengths (i.e the emission wavelength of the mixed phase peak is at $\sim$ 660nm while the absorption wavelength of the same peak is at $\sim$ 630nm) are caused by Stokes shift (see Figure 3.2).

The insert in Figure 3.1b shows that only 8% of the mixed phase converts into an I-rich phase, while other experimental works indicate 1,2 and 18% conversion [11,17,19]. Consequently, only a small fraction of the mixed phase undergoes phase segregation and despite the small fraction, the I-rich phase can dominate and cause dramatic changes in photoluminescence spectra due to the favourable energy band gap.

Moving forward, the following inequality should hold $k_{forward,em} > k_{forward,abs}$ (reminder: k is the phase segregation rate and can be measured either from the emission spectra changes or absorption spectra changes) due to the fact that the I-rich inclusions, apart from growing in fraction and size with respect to time, also collect the generated carriers from the different phases. A critical point, is that $k_{forward}$ depends on the excitation intensity I_{exc}, in general $k_{forward}$ increases as I_{exc} increases. The exclusive degree of dependence will be determined in the kinetic model description that follows. Another parameter that affects phase segregation is the thickness of the film and the excitation wavelength [30, 41]. Notably, thick films (280nm) exhibit faster phase segregation rates than thin films (70nm), while decreasing the λ_{exc} of the source also leads to faster segregation rates [30]. In addition, it is observed that

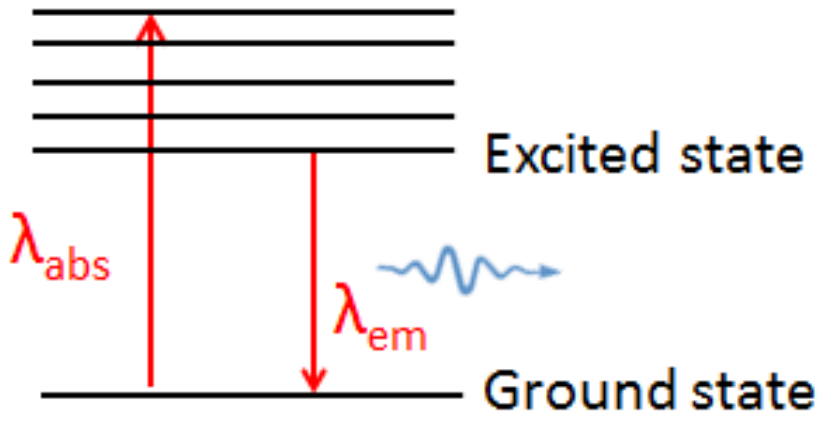

Figure 3.2: **Stokes shift.** Within the first excited state, there are different vibrational and rotational energy levels which are metastable and in about $\sim 10^{-13}$ sec (or a few ps) via internal conversion (non-radiative process) the excited carriers (which are excited at a higher energy level of the first excited state) relax into the lowest vibrational and rotational first excited state from where the carriers recombination occurs ($\lambda_{abs}<\lambda_{em}$). The arrows represent the energy difference of each transition and not the absolute value of its wavelength.

higher energy excitation (compared to an excitation energy near the band-edge) results in increased phase segregation rates [30]. That occurs due to excitation wavelength-dependent penetration depth, which results in higher carrier density for low penetration depths (low excitation wavelengths), but the fact that thicker films exhibit faster segregation rates than the thinner films remains confusing. Perhaps the influence of surface traps is more intense in thin films and this may lead to relatively slower segregation rates [30].

Finally, the most exciting and contingency fact is that the light-induced phase segregation is reversible when the light source is removed (under dark conditions). A complete recovery of all spectra features has been observed on time scales of several minutes ($\sim$ 5-30min, typically) [17–20,24,26,30,42]. The exact recovery time depends on the excitation intensity, the exposure time to irradiation, the quality of the film (crystallinity), the crystallite size and the temperature [17–19, 22]. The different time scales (minutes for recovery, seconds for phase segregation) reflect that there is a deeper mechanism behind

this, which to date remains elusive. An interesting perspective is that because the I-rich phase (x≈0.2) has a tetragonal lattice structure, the ion migration activation energies, in order to return to its initial lattice sites in the mixed phase, are higher than those in the cubic structure [17,30,38]. Also, as it will be explained later on, in the absence of illumination, the mixed phase of the perovskites is preferred, as dictated by thermodynamics at room temperature. Therefore, when the light source is removed, the system tends to recover to its initial mixed state, but perhaps there is a fundamental difference, between the transitions from cubic-to-tetragonal and from tetragonal-to-cubic. Adding to this, the feature at $\lambda \sim$ 740-750 nm is found in all $APb(I_{1-x}Br_x)_3$ perovskites (A=MA^+,FA^+,Cs^+ or mixed), despite the fact that structural changes (cubic-to-tetragonal) at x≈0.2 occurring only in the $MAPb(I_{1-x}Br_x)_3$ perovskite. Thus, the fact that the I-rich phase, in all $MAPb(I_{1-x}Br_x)_3$ perovskite films, forms at x≈0.2 due to structural transformation (cubic-to-tetragonal) and also affects the dark recovery kinetics of the system is controversial [43].

3.3 Spectral Changes in Transient Absorption

Another way to probe halide phase segregation is via transient absorption measurements [2, 17, 19, 44–46]. A schematic of the experimental setup is shown in Figure 3.3a, the pulsed laser with λ=387nm has a low excitation intensity in order to avoid phase segregation effects, while the (CW) laser with λ=405nm operates in order to induce phase segregation in the sample ($MAPb(I_{1.7}Br_{1.3})$). White light (usually a broad probe pulse) probes the changes in transient absorption. The time (in picoseconds) that the Figures indicate is the delay time between probe and pump(pulsed laser). Note that the pulsed laser excites carriers to the excited states and so the ground state is depleted from carriers, which results in a reduction in the band edge absorption compared to the initial absorption (without any pumping with

pulsed laser) leading to $\Delta A < 0$ (bleaching). In other words, $\Delta A > 0$ represents absorption from the excited states while $\Delta A < 0$ absorption from the band edge. The excited carriers can also absorb light to reach higher excited states. Consequently, in the transient absorption spectra one can see a mixture of the ground and excited states. Figure 3.3b shows the bleaching maximum at λ=625nm, which matches well with the absorption peak seen in the ground state absorption of the film(see Figure 3.1b), before (CW) laser irradiation [19]. As the delay between pump and probe increases in time, the electron-hole pairs recombine and so we see the change in absorption at the bleach peak decrease (in absolute magnitude). $\Delta A = \frac{A'-A}{A}$, where A is the initial absorption (before pump) and A' is the absorption after the pump with a pulsed laser.

Moving forward, Figure 3.3c shows that 1 min of (CW) laser irradiation is enough to form two new bleaches, around $\lambda \sim$530nm and $\lambda \sim$700nm. The new bleaches depict the I-rich and Br-rich phases. An important insight arises from Figure 3.3d (after 40min of irradiation) as we can see the well formed bleach at around 530nm (Br-rich phase), which was not so clear in Figure 3.3c and we observe that within 5ps (after pumping) the bleaching which corresponds to the Br-rich phase recovers while at the same time the bleaching maximum corresponding to the I-rich phase increases (in absolute magnitude). The excited behavior of preformed $MAPbI_3$, $MAPbBr_3$ thin films have revealed that neither has a bleaching maxima with a lifetime less than 1ns [19].

The difference in kinetic behavior and the fact that the decay of the Br-rich phase during the first 10ps (after pumping) matches the growth in the I-rich phase may indicate a pathway for energetic charge pairs from the Br-rich region to transfer into I-rich sites [19]. There is a clear evidence for that. At last, from Figure 3.3e one can observe the gradual decrease of the mixed phase bleaching maximum (at 650nm) and the growth of a new bleach at roughly 700nm (I-rich phase) with respect to time. The pump-probe delay was steadily 5ps and it probes the changes in transient absorption (at different time intervals) for the first 30 seconds of (CW) irradiation with higher excitation intensity I_{exc}=1.7W/cm^2.

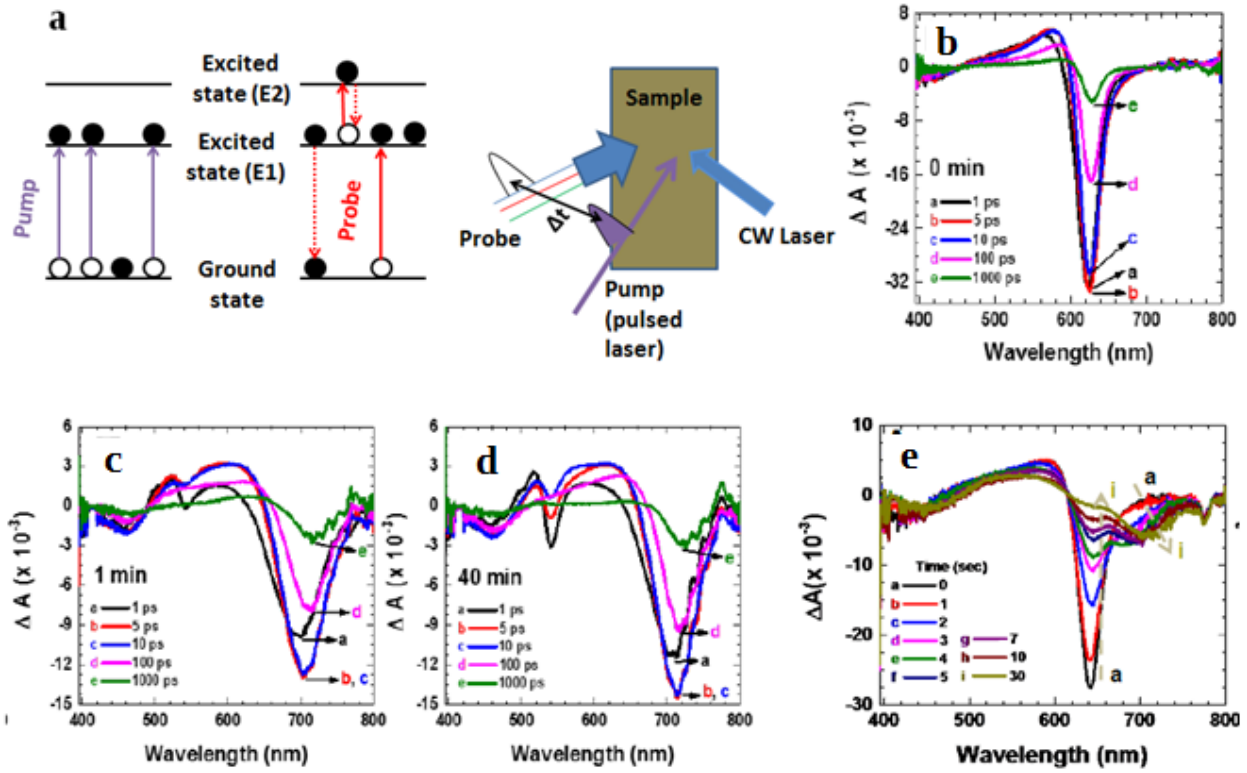

Figure 3.3: a) Schematic illustration of sample excitation for pump-probe transient absorption spectroscopy, an additional (CW) laser is used in order to induce phase segregation to the probed regions. b-d) Time-resolved difference absorption spectra of a $MAPbI_{1.7}Br_{1.3}$ film (x_{Br} ~0.43), with a pulsed laser(pump) at 387nm excitation wavelength and a 405nm (excitation wavelength) (CW) laser with I_{exc}=1.7W/cm^2. b) before (CW) laser irradiation, c) after 1min of (CW) laser irradiation and d) after 40min of (CW) laser irradiation. e) Femtosecond transient absorption spectra of $MAPbI_{1.7}Br_{1.3}$ film with 5ps delay between pump-probe, under irradiation of a 405nm excitation (CW) laser with I_{exc}=1.7W/cm^2. *Source of the Figure 3.3 (b-e)* : [19].

3.4 Light-Induced Structural Changes

The most convincing evidence that light induces halide phase segregation in $MAPb(I_{1-x}Br_x)_3$ perovskite thin films comes from X-ray diffraction (XRD) measurements that track structural changes under illumination. Figure 3.4b depicts the (200) reflection peak of $MAPb(Br_{0.6}I_{0.4})_3$ (x=0.6) at roughly 29.38° (pre-illumination) which splits into two new peaks at around 28.68°

and 29.55° after 5 minutes of white-light soaking at I_{exc}=50mW/cm^2 [17,25]. These two new peaks fit well with the original (200) reflection peaks from $MAPb(I_{0.8}Br_{0.2})_3$ (x=0.2) and $MAPb(I_{0.3}Br_{0.7})_3$ (x=0.7) thin films, as shown in Figure 3.4b. [17].

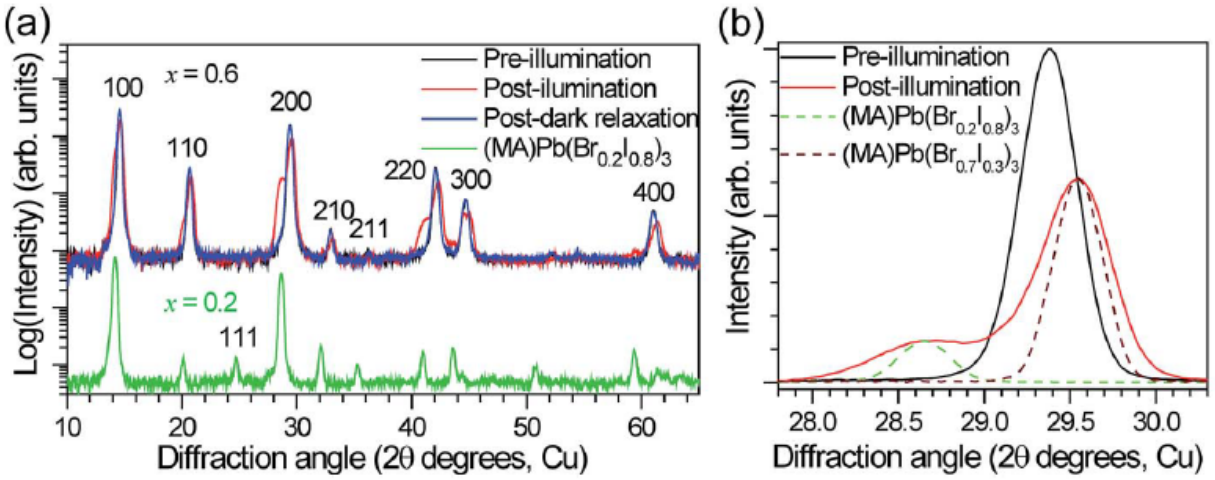

Figure 3.4: a) (XRD) pattern of a $MAPb(I_{0.4}Br_{0.6})_3$ (x=0.6) thin film before(black), after(red) white-light soaking for 5 minutes at I_{exc}=50mW/cm^2 and after 2 hours in the dark(blue), while the green (XRD) pattern is from a $MAPb(I_{0.8}Br_{0.2})_3$ (x=0.2) film for comparison. b) The (200) reflection peak of a $MAPb(I_{0.4}Br_{0.6})_3$ (x=0.6) film before(black) and after(red) white-light soaking for 5 minutes at I_{exc}=50mW/cm^2 while the (200) reflection peak of $MAPb(I_{0.8}Br_{0.2})_3$ (x=0.2) film (dashed green) and of $MAPb(I_{0.4}Br_{0.6})_3$ (x=0.6) film (dashed brown) are included for comparison. *Source of the Figure 3.4* : [17].

Also, the percentage of the I-rich phase that exists in the lattice is estimated to be 23%, while for the Br-rich phase the percentage is 77% [17]. Noticeably, all the XRD peaks recover to their initial positions (2ϑ position) under dark conditions (absence of visible light illumination), Figure 3.4a includes that information [17]. Also noteworthy, in the to-date literature, there are studies which are consistent with the measured shifts in XRD [47–49], as shown above, but on the other hand, there are studies which show negligi-

ble peak splitting from (XRD) measurements under illumination, only peak broadening has been observed, which is due to lattice strain [18, 30]. Consequently, (XRD) measurements seem to be sensitive to external parameters such as excitation intensity and wavelength, duration of irradiation and also to internal parameters such as film quality, grain size and film thickness [25].

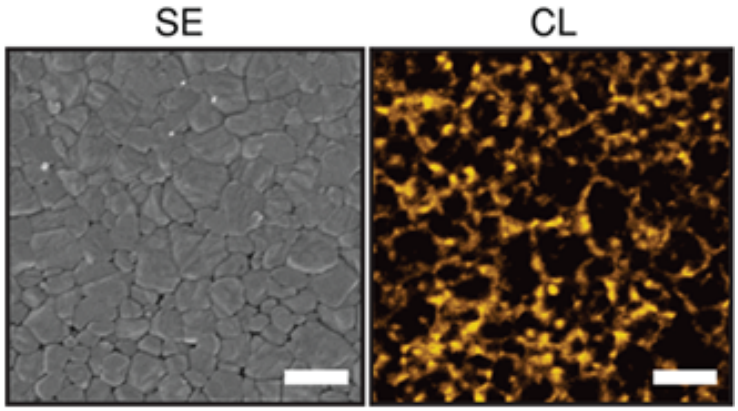

Figure 3.5: Secondary electron (SE) image and a Cathodoluminesence (CL) image of a $MAPb(I_{0.1}Br_{0.9})_3$ (x=0.9) thin film, collected after (405nm LED) light soaking for 5 minutes at I_{exc}=100mW/cm^2. The yellow-colored bright spots represent the signal from the I-rich clusters. The scale bar is 2μm. *Source of the Figure 3.5* : [20].

Finally, beyond (XRD) measurements there are also scanning electron microscopy(SEM)-based Cathodoluminesence (CL) and energy dispersive X-ray spectroscopy (EDXS) structural measurements which show that I-rich domains emerge at perovskite's grain boundaries (see Figure 3.5) [20, 30, 50–52], and X-ray photoelectron spectroscopy (XPS) measurements on $(FA_{0.85}MA_{0.15})Pb(I_{0.85}Br_{0.15})_3$ films which show that Br-rich regions instead emerge at crystal surfaces, pointing out that interfaces may be the preferred regions for halide phase segregation [25, 28].

Chapter 4

Carrier Dynamics and Suppressed Light-Induced Phase Segregation

4.1 Carrier Lifetimes in Halide Perovskites

The carrier density (n) rate of change is given by the following equation

$$-\frac{\mathrm{d}n}{\mathrm{d}t} = -G + k_1 \cdot n + k_2 \cdot n^2 + k_3 \cdot n^3 \tag{4.1}$$

where G is the carrier generation rate and k_1 is the first-order non-radiative recombination (Shockley-Read-Hall trapped-assisted recombination) and/or excitonic radiative recombination rate constant, k_2 is the second-order bimolecular radiative recombination (band to band) rate constant and k_3 is the third-order non-radiative Auger recombination rate constant [35, 53–55]. This equation is valid in the case where the density of electrons is equal to the density of holes and k_1, k_2, k_3 are constants.

In order to examine the carrier lifetime and its dependence on carrier density we can write the following equation for the total carrier lifetime

$$\tau_{o\lambda} = \frac{1}{k_1 + k_2 \cdot n + k_3 \cdot n^2} \tag{4.2}$$

obtained through the nondimensionalization of Eq.(4.1). Thus, we can define three effective lifetimes, $\tau_1 = \frac{1}{k_1}$ for the first-order recombination lifetime, $\tau_2 = \frac{1}{k_2 \cdot n}$ for the bimolecular recombination lifetime and $\tau_3 = \frac{1}{k_3 \cdot n^2}$ for the Auger recombination lifetime [55]. From the above assumptions, the τ_1, τ_2, τ_3 and $\tau_{o\lambda}$ lifetimes decrease when carrier density (n) increases while the τ_1 is approximately constant with increasing carrier density. Consequently, at low carrier density n=10^{13} cm^{-3} the first-order rate will have the shortest lifetime compared to the other two recombination lifetimes, which will be much larger [55]. When the carrier density is n=10^{17} cm^{-3} the three lifetimes will be comparable and at higher carrier density n>10^{18} cm^{-3} the Auger recombination lifetime will be the shortest and hence the dominant [55]. At room temperature, excitons are dissociated in perovskite materials due to the low binding energy (in the order of 0.2-0.3eV), and thus the first-order recombination rate exclusively refers to the monomolecular non-radiative recombination.

Finally, in time-resolved photoluminescence decay measurements (TR-PL), when more than one exponential is involved in the corresponding curve, we fit the following equation to the experimental curve, in order to evaluate the lifetimes

$$I(t) \;=\; \sum_i a_i \cdot e^{-\frac{t}{\tau_i}} \tag{4.3}$$

where a_i are the weighted amplitudes and τ_i are the corresponding lifetimes, with

$$\tau_{avg} \;=\; \frac{\sum_i a_i \cdot {\tau_i}^2}{\sum_i a_i \cdot \tau_i} \tag{4.4}$$

Thus, the photoluminescence quantum yield is defined as

$$(PLQY) \;=\; \frac{k_r}{k_r \;+\; \sum k_{nr}} \tag{4.5}$$

whence the radiative recombination rate is denoted by k_r and the non-radiative recombination rates are denoted by k_{nr}.

4.2 Mitigation of Light-Induced Halide Phase Segregation

In this part, we briefly review the most significant efforts to suppress light-induced halide segregation. An empirical method suggests that A-cation alloying, such as partial substitution of (MA^+) cation with (FA^+), or mixing (FA^+) with (Cs^+) cations, can suppress the phase segregation [5,11,21,56,57]. The improved stability was attributed to the reduction of electron-phonon coupling, which is a critical factor for phase segregation due to the fact that (FA^+) and (Cs^+) are less polar compared to (MA^+) [18, 20, 21, 24, 38].

Furthermore, improving the overall crystallinity (via morphological engineering) by applying a nonwetting hole-transporting layer to $MAPb(I_{1-x}Br_x)_3$ perovskite thin films, which enhances grain size, results in a reduced tendency for phase segregation [25, 27, 58]. The improved crystallinity may reduce the halide vacancies, which play a central role in phase segregation. Another reported procedure is the partial substitution of (Pb^{2+}) with (Sn^{2+}) which effectively suppresses the phase segregation. The reason for this is that (Sn^{2+}) is a smaller cation than (Pb^{2+}) which changes the internal bonding of BX_6 octahedra [42]. Also, application of external pressure, and alloying (Cl^-) with iodide and bromide anions, is found to minimize the phase segregation effects [59, 60]. Moreover, trap states passivation can reduce the amount of ion vacancies and suppress phase segregation [61, 62].

At last, close-packed nanocrystal films do not undergo phase segregation due to the significant reduction in the carrier diffusion length $l_{e/h}$ which is physically restricted in nanocrystals with domains size $\sim$ 10nm [22, 23].

Chapter 5

Theoretical Models for Light-Induced Phase Segregation

5.1 Phase Segregation Kinetics - Kinetic Model

In this part, we will turn our attention to the kinetics of phase segregation, emphasizing on the main processes which occur under light excitation, and finally we will derive useful expressions and define significant parameters, that have an impact on and affect the process of phase segregation. This model was proposed by Draguta et al. [22] whose supposed that when the phase separation occurs, three phases are formed (in total) and the fraction of each one is ϕ_{mix} for the mixed phase, ϕ_I for the iodide-rich phase and ϕ_{Br} for the bromide-rich phase. We can obtain then

$$\phi_{mix} \; + \; \phi_I \; + \; \phi_{Br} \; = \; 1 \tag{5.1}$$

assuming that $\phi_I = \phi_{Br}$ (phase segregation produces equal fractions of two different phases), then one can write

$$\begin{aligned} \phi_{mix} + 2 \cdot \phi_I \; &= \; 1 \; \Rightarrow \; \phi_{mix} \; + \; \phi_{ps} \; = \; 1 \\ &\Rightarrow \; \phi_{mix} \; = \; 1 \; - \; \phi_{ps} \end{aligned} \tag{5.2}$$

where ϕ_{ps} is the total fraction of phase-segregated domains ($\phi_{ps} = 2\phi_I$).

Moving forward, the first process that will be covered is carrier generation. The carrier generation rate in the excited state of the mixed phase ($(\mathrm{MAPb}(\mathrm{I}_{1-x}\mathrm{Br}_x)^*_3$, where asterisk denotes excited state) is given by

$$G \;=\; \frac{a \cdot I_{exc}}{h \cdot \nu_{exc}} \tag{5.3}$$

whence I_{exc} is the excitation intensity ($\mathrm{W}\cdot cm^{-2}$), a is the absorption coefficient (cm^{-1}) of the perovskite, h is the planck constant and ν_{exc} is the frequency of the incident photon, while the carrier density by assuming only generation is

$$N \;=\; G \cdot \tau \tag{5.4}$$

where τ is the carrier lifetime.

The second process refers to radiative recombination in the mixed phase which corresponds to emission. The radiative recombination rate is given by

$$R_1 \;=\; (QY) \cdot \phi_{mix} \cdot G \;=\; (QY) \cdot (1 - \phi_{ps}) \cdot G \tag{5.5}$$

where the (QY) denotes the external quantum yield [22].

Continuing, the third process refers to phase separation under light excitation and the rate of phase separation is taken to be first order to the generation rate :

$$R_2 \;=\; k_2 \cdot \phi_{mix} \cdot G \;=\; k_2 \cdot (1 - \phi_{ps}) \cdot G \tag{5.6}$$

where k_2 is a unitless constant.

The last process is the phase-segregation recovery in the absence of light excitation (dark). The recovery rate is

$$R_3 \;=\; k_3 \cdot \phi_{ps} \cdot n \tag{5.7}$$

where n is the average molar volume of the domains [22].

In the rate of change of ϕ_{ps}, only the rates R_2 and R_3 contribute, so we obtain then

$$n \cdot \frac{\mathrm{d}\phi_{ps}}{\mathrm{d}t} \;=\; R_2 \;-\; R_3 \tag{5.8}$$

The negative sign indicates that the rate R_3 tends to reduce ϕ_{ps} with time [22].

By substitution of R_2 and R_3 from Eq.(5.6) and Eq.(5.7) to Eq.(1.8), we have

$$\frac{\mathrm{d}\phi_{ps}}{\mathrm{d}t} \;=\; \frac{k_2 \cdot G}{n} \cdot (1 - \phi_{ps}) \;-\; k_3 \cdot \phi_{ps} \;=\; c_1 \;-\; c_2 \cdot \phi_{ps} \tag{5.9}$$

where $c_1 = \frac{k_2 \cdot G}{n}$ and $c_2 = c_1 + k_3$ [22].

The solution of this differential equation, using the initial condition $\phi_{ps}(0)$=0, is

$$\phi_{ps} \;=\; \frac{c_1}{c_1 + c_2} \cdot (1 - e^{-c_2 \cdot t}) \tag{5.10}$$

In the limit that phase segregation occurs on a faster timescale than recovery ($c_1 \gg k_3$), we have

$$\phi_{ps} \;\approx\; 1 \;-\; e^{-c_2 \cdot t} \tag{5.11}$$

$$\phi_I \;=\; \frac{\phi_{ps}}{2} \;\approx\; \frac{1 - e^{-c_2 \cdot t}}{2} \tag{5.12}$$

It is experimentally proven that the phase segregation rate, as a rate which increases the number of I-rich domains with time, and is calculated from the changes in the absorption spectra with respect to time, is much slower (2 orders of magnitude) than the rate of change of the I-rich phase emission, suggesting carrier diffusion from the mixed halide phase to the iodide-rich phase [22]. This suggestion is enhanced by density functional theory (DFT) calculations which indicate that mixed halide and iodide-rich conduction band edges are isoenergetic and that the iodide-rich phase has lower valence band edges than the mixed phase, suggesting hole diffusion as the dominant process taking place [22, 62, 63]. This implies that if within a volume, which is defined by the diffusion length $l_{e/h}$, there is an iodide-rich cluster, then the excited carriers of the mixed state will diffuse (due to the lower energy band gap) towards this cluster and recombine from there. Because the diffusion length is typically $l_{e/h}$=100nm (for $MAPb(I_{1-x}Br_x)_3$ films), the Einstein relation can be used to evaluate $\tau_{diff} = \frac{l_{e/h}^2}{D}$ with diffusion coefficient D=0.08cm^{2}s^{-1}. That gives τ_{diff}=1.25ns, which is much smaller than the value of carrier liftime $\sim$ 60ns in $MAPb(I_{1-x}Br_x)_3$ films [22]. As a result, I_{iodide} (from emission spectra) is proportional to the Poisson distributed probability (P) of carriers encountering at least one iodide domain upon diffusion [22]. The probability for the carriers to encounter a zero number of domains is $P_{none} = e^{-n_I}$, and so

$$P \;=\; 1 \;-\; P_{none} \;=\; 1 \;-\; e^{-n_I} \tag{5.13}$$

where n_I is the average number of iodide domains within the diffusion volume V_D, and by assuming $I_{iodide} \propto P$ one can obtain [22]

$$I_{iodide} \;=\; I_{sat} \cdot (1 \;-\; e^{-n_I}) \tag{5.14}$$

But,

$$n_I \;=\; \frac{V_D}{V_{avg}} \cdot \phi_I \tag{5.15}$$

where V_{avg} is the average volume of the iodide-rich domains.

Using the linear approximation of Eq.(5.12), we obtain

$$\phi_I \;\approx\; \frac{k_2 \cdot G}{2 \cdot n} \cdot t \tag{5.16}$$

by substitution we finally reach to the expression

$$\begin{aligned} \frac{I_{iodide}}{I_{sat}} \;&\approx\; [1 \;-\; e^{-\frac{V_D \cdot k_2 \cdot G}{2 \cdot V_{avg} \cdot n} \cdot t}] \;\Rightarrow \\ \frac{I_{iodide}}{I_{sat}} \;&\approx\; 1 \;-\; e^{-\; k_{forward,em} \cdot t} \end{aligned} \tag{5.17}$$

with

$$k_{forward,em} \;=\; \frac{V_D \cdot G \cdot k_2}{2 V_{avg} \cdot n} \tag{5.18}$$

which is experimentally estimable [22].

We are now interested in the intensity dependence of the phase segregation rate constant $k_{forward,em}$ which can be derived using a simple model in which the probability of creating a phase-segregated domain within the geometric volume V_D is the same irrespective of the number of carriers in this volume [22]. Consequently, we assume that the $k_{forward,em}$ is proportional to the

Poisson-distributed probability that at least one carrier exists within V_D [22]

$$k_{forward,em} \approx 1 - e^{-V_D \cdot N} \tag{5.19}$$

where $V_D \cdot N$ equals to the average number of carriers within the volume V_D, thus

$$k_{forward,em} = k_{sat} \cdot (1 - e^{-V_D \cdot N}) \tag{5.20}$$

and by substitution of Eq.(5.3),(5.4), we finally find

$$\boxed{k_{forward,em} = k_{sat} \cdot (1 - e^{-\beta \cdot I_{exc}})} \tag{5.21}$$

where $\beta = \frac{a \cdot \tau \cdot V_D}{h \cdot \nu_{exc}}$ and k_{sat} is a constant. If we evaluate (experimentally) the k_{sat}, β and the $k_{reverse,em}$ which is the recovery rate constant, then we can find a I_{th} threshold excitation intensity, below which phase segregation does not occur, from the condition $k_{reverse,em} \geq k_{forward,em}$ or by setting $k_{reverse}$ to be at least one order of magnitude higher than $k_{forward}$.

Consequently, the phase segregation rate can be tuned by varying the excitation intensity and the carrier diffusion lengths, a significant insight revealed from the current kinetic model.

Before closing this section, it is worth noting that while this model can explain the experimentally observed exponential dependence of $k_{forward,em}$ on I_{exc}, it is only accurate to the limit of low excitation intensities, where the linear dependence of carrier density N to I_{exc} is a good approximation.

5.2 Vacancy-Mediated Phase Segregation

This model suggests that the driving force for phase separation is the ion migration via existing vacancies in the lattice of halide perovskites [13,19,26,30]. There are three types of vacancies in a $MAPb(I_{1-x}Br_x)_3$ film, methylamonium vacancies (V_{MA}), (V_{Pb}) for lead vacancies and (V_I, V_{Br}) for anion vacancies which are supposed to have the same activation energies, $E_A(I) = E_A(Br)$. Activation energy is defined as the requisite amount of energy needed for the ions to overcome kinetic barriers and migrate to the closest vacant site. The vacancy activation energies of these species have been evaluated to be E_A=0.58eV for iodide vacancies, E_A=2.31eV for Pb^{2+} and E_A=0.84eV for (MA^+) in a $MAPbI_3$ film [13]. Consequently, vacancy-assisted diffusion of iodide anions is favourable [13]. The activation energies for vacancy-ion migration differ in perovskites with different A cations due to different lattice structures, volume, strain, ionic radius and density of crystal defects [5,13,27]. Depending on perovskite, the experimental range of values is 0.17-0.25eV for V_{Br} and 0.23-0.43eV for V_I [27, 64–66], whereas theoretical values for anion vacancies are 0.09-0.27eV for bromide vacancies and 0.08-0.58eV for iodide vacancies [13, 64, 67].

The diffusion coefficient of iodide ions is four orders of magnitude higher than that of (MA^+), hence we can assume negligible diffusion for the (MA^+) cation [13]. Also, halide ion mobility is known to be a significant factor in the performance of solar cells [5]. It also seems that the phase segregation rate (either calculated from changes in photoluminescence with time or from changes in absorption with time) increases linearly with respect to the vacancy concentration, which is reasonable due to the fact that as the concentration of vacancies increases, there is availability and migrating ions undergo fewer steps to associate with a Pb^{2+} center [29].

According to this model, the existence of an I-rich phase in the form of $MAPb(I_{0.8}Br_{0.2})_3$ (rather than $MAPbI_3$) occurs due to the kinetically trapped bromide anions within the I-rich region. In the growth process of the I-rich region, the iodide anions continuously infiltrate inwards and the most vacancies have been exported (meaning that when an anion occupies a vacancy

site, a new vacancy site is created in the site from where the anion escaped), a small concentration of Br^- within the I-rich region faces difficulties in escaping [29, 30].

Finally, a key factor for ionic conductivity is the level of intrinsic anion vacancies, which is sensitive to synthesis conditions and thermal processing routes [13].

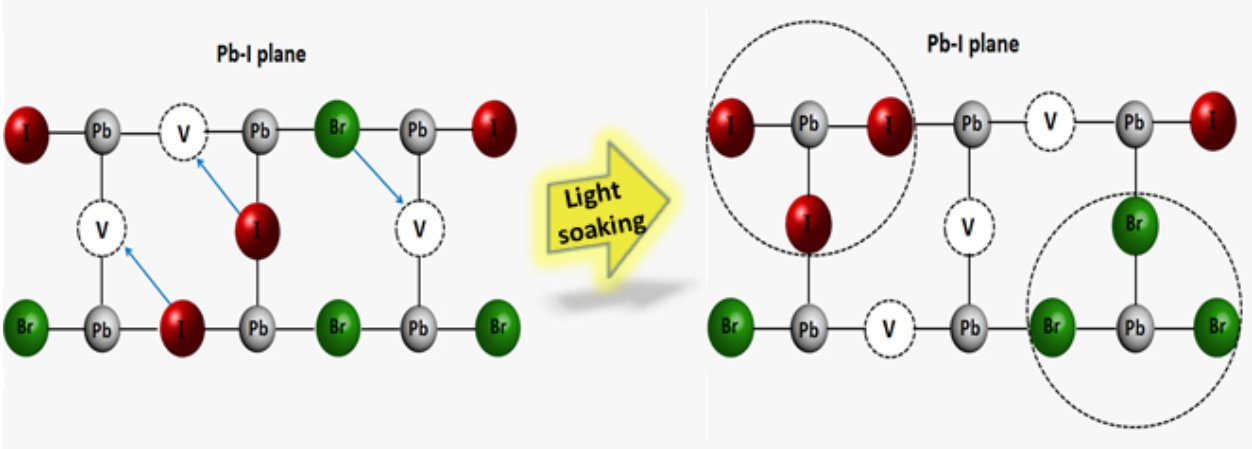

Figure 5.1: Schematic illustration of vacancy-assisted phase segregation under light excitation, which leads to the formation of I-rich and Br-rich domains. Only the halide vacancies in the Pb-I plane of mixed halide lead perovskite are involved.

5.3 Thermodynamic-based Unified Theory for Light-Induced Phase Segregation

We are going to describe the Unified Theory for light-induced halide segregation, suggested by Chen et al. [68], which makes some improvements to the previous models. The first thermodynamic model for halide phase separation was presented by Brivio et al. [16] which determined and calculated using first-principles the thermodynamic quantities (such as mixing energy, mixing entropy, Helmholtz free energy) of the system in the dark (absence of illumination). Afterwards, Draguta et al. [22] took it a step further by adding a new term, due to the excitation of the system, in the free energy (excited state). Chen et al. [68] recently proposed a unified theory based on those two earlier models but making some different assumptions, which led this theory to predict more precisely the behavior of a mixed halide perovskite under illumination conditions.

Preliminaries. To begin, we need to determine and define the corresponding thermodynamic variables, starting from the calculation of the total energies of the single-cation mixed halide lead perovskite of type $APb(I_{1-x}Br_x)_3$ (mixed state), E_{mixed}, E_{APbI_3}, E_{APbBr_3}. The mixing enthalpy (or internal energy) is then calculated using $\Delta U = E_{mixed}$ - (1-x)E_{APbI_3} - xE_{APbBr_3}.

Then we calculate the mixing entropy which for ideal mixing is :
ΔS_m = -k_β[xlnx + (1-x)ln(1-x)], where x is the bromide concentration.

Finally, we calculate the free energy of the system from

$$\Delta F(x,T) \;=\; \Delta U(x,T) \;-\; T \cdot \Delta S(x,T)$$

from which, therefore, we can construct the composition-temperature phase diagram. This is for the ground state of the system (without excitation).

Moving forward, the calculation of the total energies in mixed halide lead perovskites with chemical formula $APb(I_{1-x}Br_x)_3$ where A=MA^+,FA^+,Cs^+

starts with the construction of a periodic supercell of the pure I compounds containing 2 formula units (FU), with a 2x1x1 expansion of a pseudo-cubic perovskite building block [68]. Then follows the replacement of I anions by Br anions at different concentrations. The total number of possible configurations is 2^6=64 (two anions I^-,Br^-, six lattice sites). For the Cs cation perovskite with perfect Oh symmetry the three halide sites are equivalent, so the total number reduces to 21 [68]. Also, accounting for the deviation from Oh symmetry in case of the (MA^+) and (FA^+) cation perovskites leads to 36 inequivalent configurations. The total energy calculations are performed within Density-Functional Theory (DFT).The whole procedure is described in detail at Chen et al. [68] work.

In order to calculate the Helmholtz free energy within the quasi-chemical approximation (QCA) of binary alloying theory, we first need to calculate the configurational mixing enthalpies ΔU_j per formula unit (FU) which are given by

$$\Delta U_j \;=\; E_j \;-\; (1 \;-\; x)\cdot E_{APbI_3} \;-\; x\cdot E_{APbBr_3} \tag{5.22}$$

where j=1,..,J refers to inequivalent configurations, x is the relative Br concentration and E_j the total energies per (FU) of configuration j. The A-cation in this study will be one of the following MA^+,FA^+,Cs^+, $MA_{7/8}Cs_{1/8}$ or $FA_{7/8}Cs_{1/8}$. The values of j will be, J=36 for A=MA^+ or FA^+ and J=21 for A=Cs^+ as described above. The calculation of the energy of all possible configurations of the anions in a supercell was held within density functional theory (DTF) [68].

By applying the quasi-chemical approximation [69], one can obtain the change of the mixing enthalpy ΔU(x,T), mixing entropy ΔS(x,T) and Helmholtz free energy ΔF(x,T) as a continuous function of x and temperature T. The main idea of (QCA) is the decomposition of the perovskite lattice into microclusters, which can be treated independently [68, 69]. In the (QCA), the

thermal equilibrium fraction of microclusters with configuration j is given by

$$\overline{x_j} \;=\; \frac{g_j \cdot exp(\frac{n_j(Br)\cdot\mu_{Br} \;-\; \Delta U_j}{k_\beta \cdot T})}{\sum_j g_j \cdot exp(\frac{n_j(Br)\cdot\mu_{Br} \;-\; \Delta U_j}{k_\beta \cdot T})} \tag{5.23}$$

where g_j is the degerenacy and n_j(Br)=0,1,2,3 the number of Br anions per (FU) of the configuration while μ_{Br} is the Br chemical potential [68,69]. The chemical potential should be determined by the condition

$$\sum_j n_j(Br) \cdot \overline{x}_j \;=\; 3x \tag{5.24}$$

Finally, the change in mixing enthalpy and entropy per (FU) is given by

$$\Delta U(x,T) \;=\; \sum_j \overline{x_j} \cdot \Delta U_j \tag{5.25}$$

$$\Delta S(x,T) \;=\; -3k_\beta \cdot [(1-x)\cdot\ln(1-x) \;+\; x\cdot\ln x \;+\; \sum_j \overline{x_j} \cdot \ln(\frac{\overline{x_j}}{{x_j}^0})] \tag{5.26}$$

where ${x_j}^0 \;=\; g_j \cdot x^{n_j} \cdot (1-x)^{3-n_j}$

$$\Delta F(x,T) \;=\; \Delta U(x,T) \;-\; T\cdot\Delta S(x,T) \tag{5.27}$$

where $\Delta U(x,T)$ and $\Delta S(x,T)$ are given by Eq.(5.25) and Eq.(5.26) respectively. These equations are solved for different x and T values, numerically.

Note that, for condensed phases within the quasi-chemical approximation,

$\Delta U_{mix} \approx \Delta H_{mix}$ because the term which separates them is close to zero ($P \cdot \Delta V_{mix} \sim 0$).

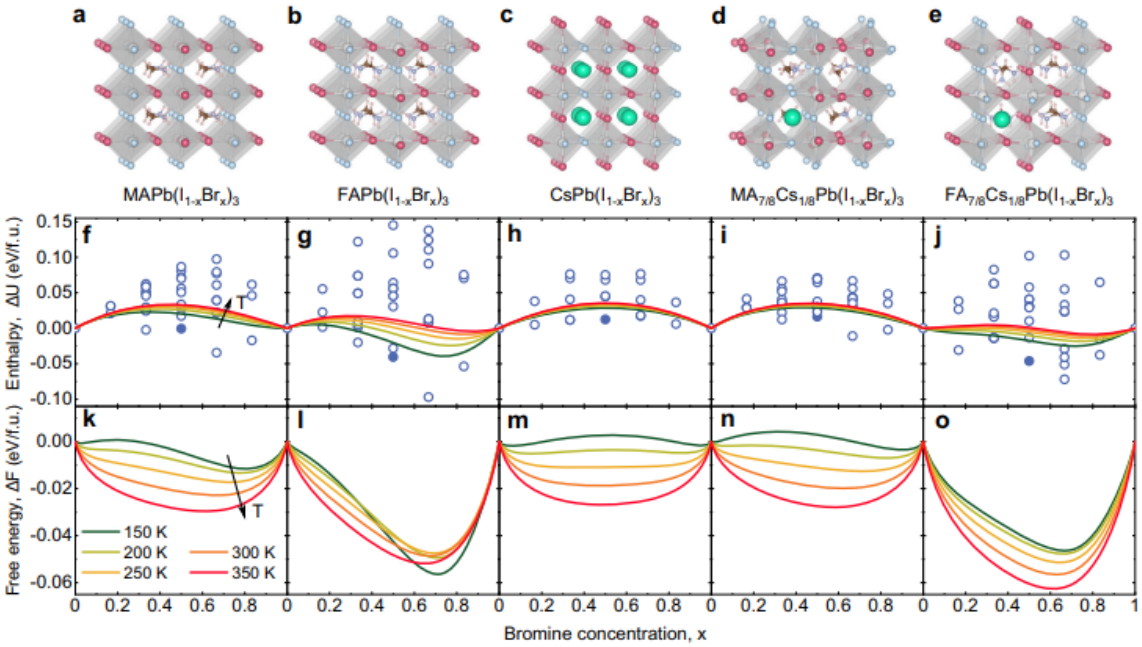

Figure 5.2: **(a-e) :** Atomic structures of the most stable configurations of the different compounds at x = 0.5, where red spheres depicts : I, blue spheres: Br, white spheres inside octahedra: Pb, green spheres: Cs. Cationic molecules in between octahedra: methylammonium (MA) or formamidinium (FA). **(f–j) :** Mixing enthalpy and free energy of lead mixed halide perovskites in the dark. Circles: values calculated for each mixed configuration. Filled circles: values for the most stable configurations at x = 0.5, displayed in (a–e). Curves: results for the quasi-chemical approximation (QCA) at different temperatures. **(k–o) :** Mixing free energy per (FU) as a function of Br concentration x. *Source of the Figure 5.2* : [68].

The first thing we notice in Figure 5.2(f-h), is that the width of the mixing enthalpy distribution ΔU (for different halide configurations) for the first three compounds (single-cation case), increases in the order Cs$\longmapsto$MA$\longmapsto$FA of increasing cation size [68]. This is due to the different sizes of the halide anions (r_I=2.20Ang > r_{Br}=1.96Ang [1,70]), the strain in the lattice for different halide configurations is best accommodated by $CsPb(I_{1-x}Br_x)_3$ followed by

$MAPb(I_{1-x}Br_x)_3$ and $FAPb(I_{1-x}Br_x)_3$ [68]. Note that, the above sequence for best accommodation originate from the following sequence of the ionic sizes r_{Cs}=1.67Ang < r_{MA}=2.17Ang < r_{FA}=2.53Ang and also the volume follows the same sequence $V_{Cs} < V_{MA} < V_{FA}$ and therefore the same occurs for the lattice constant. Another significant observation is that the free energy of all five compounds in the dark at room temperature is negative, confirming the stability of the perovskite mixed phase in the absence of illumination.

It is time to focus on the light-induced halide phase segregation. The consideration that the total free energy in the excited state (under illumination) $\Delta F^*(x,T)$, will be a combination of the mixing free energy in the dark $\Delta F(x,T)$ and the free energy of photocarriers in the presence of illumination, is a key component of this theory [68]. The excited carriers can reduce their free energy by funneling to low energy band gap domains, this can be the driving force for halide demixing [22]. If one combines it with the well-known insight that halide anions in hybrid halide perovskites are quite mobile, then one can reasonably assume that stochastic fluctuations in halide composition would spontaneously arise regions which are rich in iodide and have a lower energy band gap [68]. In other words, the lack of compositional uniformity (locally) combined with the long carrier diffusion lengths and lifetimes can lead to the accumulation of photo-generated carriers into these lower band gap regions and efficiently stabilize and enrich them. Accumulation of diffusing carriers in these regions will reduce their free energy, which can further be reduced by inward diffusion of iodide into these regions, leading to nucleation of an I-rich phase and consequently to phase separation [68]. From the above, it is obvious that the energy band gap differences of perovskites with varying compositions, play a central role.

Let us now define n as the density of photo-generated carriers (electrons,holes) per (FU) in the mixed phase perovskite with bromide concentration x. When $n << 1$, Boltzmann's distribution can be used for excited carriers. If we assume that phase separation occurs into two phases with Br concentration x_1 and x_2, the generated carriers will redistribute over these two phases according to the Boltzmann factors : $\exp(-\frac{Eg(x_1)}{k_\beta T})$ and $\exp(-\frac{Eg(x_2)}{k_\beta T})$ where Eg(x) is

the energy band gap as a function of bromide concentration x [68].

$$\boxed{\frac{n_2}{n_1} \;=\; exp(-\;\frac{Eg(x_2)-Eg(x_1)}{k_\beta T})} \tag{5.28}$$

whence n_1 and n_2 are the carrier densities in the two phases. Therefore, we can derive the formula for the mixing free energy of the excited state ΔF^* per (FU) under illumination

$$\boxed{\begin{array}{c}\Delta F^*(x_1,x_2,\phi_1,\phi_2,T) \;=\; \phi_1\cdot\Delta F(x_1,T) \;+\; \phi_2\cdot\Delta F(x_2,T)\\ +\; n_1\cdot\phi_1\cdot Eg(x_1) +\; n_2\cdot\phi_2\cdot Eg(x_2)\end{array}} \tag{5.29}$$

where ϕ_1 and ϕ_2 are the corresponding volume fractions of the two phases, respectively. Also, neglecting the small volume difference per (FU) between the two phases, the following conditions should hold : $\phi_1+\phi_2=1$ and $\phi_1\cdot x_1+\phi_2\cdot x_2=x$ [68].

The sum of the first two terms in Eq.(5.29) is the volume-weighted compositional mixing free energy in the dark, while the sum of the last two terms is the photocarrier contribution to the free energy [68]. Because the band gap difference between the I-rich and mixed phase is much larger in general than the thermal energy ($\sim$ 25meV at room temperature), even a low excitation intensity can result in a relatively large change in ΔF^*, according to Eq.(5.28) [68]. In steady state, the rate of photo-generated carriers per (FU) in the system should be equal to the sum of the rates of carriers annihilation by monomolecular and bimolecular recombination in the different phases [68]

$$\boxed{G \;=\; \phi_1\cdot(\frac{n_1}{\tau} \;+\; \frac{k\cdot n_1^2}{V}) \;+\; \phi_2\cdot(\frac{n_2}{\tau} \;+\; \frac{k\cdot n_2^2}{V})} \tag{5.30}$$

The Eqs.(5.28, 5.29, 5.30) are the basis of this unified theory for light-induced

halide segregation, and from Eqs.(5.28) and (5.30) one can calculate the carrier density n_1 and n_2, for a given G [68]. Then by substitution of n_1 and n_2 in Eq.(5.29) one can calculate the mixing free energy under illumination and can obtain the spinodal and binodal (for the phase diagram) for phase segregation. Before moving to the phase diagrams, we need to determine the difference in band gaps between the mixed and I-rich phase (which is assumed to be $APbI_3$). The formula (in eV) is

$$\Delta Eg(x) \;=\; Eg(x) \;-\; Eg(x=0) \;=\; a\cdot x \;+\; b\cdot x^2 \qquad (5.31)$$

where a,b are constants. The Eg(x), a and b for each lead halide perovskite of the form $APb(I_{1-x}Br_x)_3$, with A=MA^+,FA^+ or Cs^+ have been obtained from experiments [71–73] and are presented at Chen et al. [68]. The ΔEg at room temperature increases monotonically with x and for instance reaches the value 0.28eV at x=0.5 for $MAPb(I_{1-x}Br_x)_3$ perovskite [22].

Phase diagrams. The importance of a phase diagram lies in the fact that it contains the spinodal and binodal curves, from which we can extract information about when a mixture is unstable, metastable and stable with respect to temperature. Between the spinodal and binodal curves the mixture is metastable while above the binodal it is stable and below the spinodal curve it is unstable. To construct the x-T diagram, we first need to calculate the mixing free energy ΔF(x,T) at constant T. The spinodal points therefore will satisfy the $\frac{d^2\Delta F}{dx^2} = 0$ condition, whereas the binodal points are determined by the compositions with a common tangent. We follow the same procedure by varying the temperature. That is the case for the ground state (absence of illumination).

For the excited state the calculation of these points,curves is more complicated. In this case, in order to find the binodals one should consider the possibility, starting from the mixed phase with concentration x, of lowering the free energy by demixing through nucleation of a phase with concentration $x_2 \neq x$ with a small volume fraction δφ=φ_2 [68]. Then one has to calculate the

difference in free energy between the demixed state : $\Delta F^*(x_1, x_2, 1-\delta\phi, \delta\phi, T)$ and mixed state : $\Delta F^*(x, x, 1, 0, T)$. When $\delta\Delta F^*<0$, the demixed state has lower free energy than the mixed phase, hence for a given carrier density n, one can find the binodals by looking in x-T phase space for a value of x_2 of a nucleated-phase for which $\delta\Delta F^*=0$ [68].

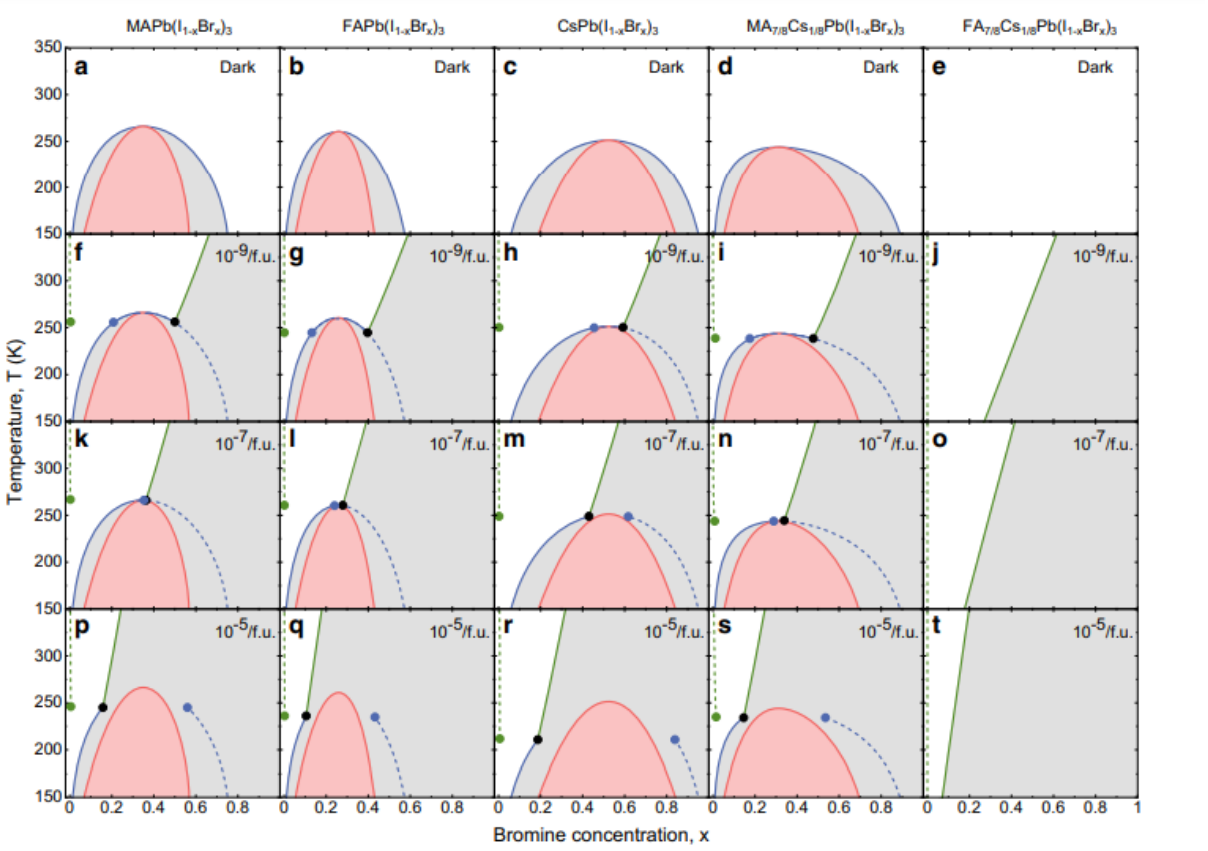

Figure 5.3: **(a-e) :** Phase diagrams in the dark of the different compounds in the temperature window 150–350 K. **(f–t) :** Phase diagrams for excited carrier densities n = 10^{-9}, 10^{-7}, and 10^{-5} per (FU) where red lines: spinodals separating the metastable (grey) and unstable (pink) regions, full blue and green lines: binodals separating the stable (white) and metastable regions, with the blue (green) lines indicating the compositional (light-induced) binodals. Compositional binodals are the corresponding binodals in the dark. When entering the metastable region by crossing the compositional (light-induced) binodals, nucleation of a phase with a Br concentration indicated by the dashed blue (green) lines becomes favourable. The dots indicate the possible coexistence of three phases: the parent phase (black dots) and two types of nucleated phases with different Br concentration (blue and green dots). *Source of the Figure 5.3* : [68]

On the other hand, to find the spinodals one should consider the possibility to decrease the free energy by generating a volume fraction φ of a phase with a slightly different concentration x_2=x+δx [68]. The free energies in the demixed state can now be written as $\Delta F^*(\frac{x-\phi\cdot\delta x}{1-\phi}, x+\delta x, 1-\phi, \phi, T)$ [68]. By taking the difference in free energy $\delta\Delta F^*$ to be equal to zero, one can determine the spinodals in x-T phase space. For a more detailed analysis, one should read the work of Chen et al. [68].

Figure (5.3 a-e) shows that the miscibility gaps which occur under a critical temperature T_c (above the T_c, the mixed phases are stable) are far away from the room temperature, which means that the mixed compounds should be thermodynamically stable at room temperature in the dark. The last compound has T_c <150K. It is worth mentioning that the older model by Brivio et al. [16] predicted T_c=343K for $MAPb(I_{1-x}Br_x)_3$, instead the current model predicts T_c=266K, which agrees with the experimental results which show that the $MAPb(I_{1-x}Br_x)_3$ does not separate at room temperature, reflecting the improvements this model has taken into consideration. We mention that $n = 5 \cdot 10^{-7}$/f.u corresponds to an illumination intensity of one sun (I=100mW/cm^2). From the x-T diagrams, we observe that the spinodals (red line) only slightly change with increasing carrier density, in contrast to the binodals, which change dramatically with increasing n. The most significant observations one can make from the phase diagrams are summarized below :

1. By increasing the carrier density n, which reflects the increasing excitation intensity, the range of Br concentration x contained within the miscibility gap increases, which indicates that by increasing the excitation intensity, the two phases that will be established will have slightly different concentrations (x_1,x_2)
2. There is a threshold carrier density below which phase separation does not occur

Several experimental works, including ours (as shown in the following section) are in agreement with the observation number 1), as all have found a redshift to the emission peak of the I-rich phase with increasing excitation intensity. The second observation 2), is consistent with the experimental findings [74] and this is the reason that the current theoretical model stands out

compared to the earlier models [16, 22]. Note that, this model is applicable to the onset of phase separation and it is not applicable to extremely high carrier densities (such as at 2000 sun illumination intensity) because of the Boltzmann approximation's breakdown.

In summary, this model has made necessary improvements compared to the previous models, which makes it accurate for predicting the behavior of the system under illumination, but there is still one assumption which is not correct and should be taken into consideration. This assumption has to do with the energy band gap of the mixed phase, the pure I and Br phases which is assumed to be temperature independent. This is an approximation because the semiconductor's energy band gap changes with respect to temperature. Despite that, the term that contributes to the free energy of the system only under illumination does have a dependence on temperature via the photo-generated carrier density.

5.4 Polaron-assisted Light-Induced Phase Segregation

In this theoretical model proposed by Bischak et al. [20], stabilized polarons are considered to play a major role in phase separation. It is suggested that the high ionicity of the perovskite lattice combined with low electron-hole binding energies results in the formation of polarons due to carrier localization at stochastically created I-rich domains. This induces lattice strain which in turn induces iodide migration to the polaron region, leading to an accumulation of iodide that causes I-rich domains to grow in sizes of $\sim 8-10$nm. Polarons have short lifetimes, so continuous excitation is needed (or high repetition pulsed lasers) for stabilization and for a steady-state concentration of polarons [20].

Hybrid perovskites also have reported high values of static dielectric constant which results in strong electron-phonon coupling and large polarizabil-

ities which in turn results in low electron-hole binding energies [20,34,75,76]. The theoretical description of this model starts with the assumption that phase segregation of the halide anions follows the landau theory with strain and excess charge and satisfies the Flory-Huggins solution theory :

$$H_c \;=\; \int_r a \cdot \phi(r) \cdot [1-\phi(r)] \;+\; T \cdot [\phi(r) \cdot \ln \phi(r) \;+\; [1-\phi(r)] \cdot \ln[1-\phi(r)]] \tag{5.32}$$

where T is the temperature, ϕ is the local concentration of iodide relative to bromide. The second term is the mixing entropy assuming ideal mixing. The first term is the mixing enthalpy in Flory-Huggins theory. According to this theory the difference in the mixing energy can be written as

$$\begin{aligned} \Delta H_{mix} \;&=\; N \cdot z \cdot X_A \cdot X_B \cdot (e_{AB} \;-\; \frac{e_{AA}+e_{BB}}{2}) \;=\; a \cdot X_A \cdot X_B \\ \Rightarrow \Delta H_{mix} \;&=\; a \cdot X_A \cdot (1 \;-\; X_A) \end{aligned} \tag{5.33}$$

from where the a can be extracted as

$$a \;=\; N \cdot z \cdot (e_{AB} \;-\; \frac{e_{AA}+e_{BB}}{2}) \tag{5.34}$$

whence z depends on the crystal structure, N is the total number of the atoms(molecules) and e_{AB}, e_{AA} and e_{BB} is the energy of the A-B bond, A-A bond and B-B bond respectively, while the A and B are two atoms(or molecules). The term $N \cdot z \cdot X_A \cdot X_B$ represents the total number of the A-B bonds, while the remaining term (in parenthesis) is the energy increment for each A-B bond, taking into account that each of the A-B bonds occurs at the expanse of the other two bonds. In our case $X_A = \phi(r)$. Moving forward the

strain field that will be used is in the following form

$$H_1 \;=\; \int_r \frac{K \cdot \Sigma^2(r)}{2(1-\nu)} \tag{5.35}$$

where Σ is the local strain, K is bulk modulus in the mixed phase and ν is Poisson's ratio [20].

Adding those terms with one more bilinear to strain field term, to the Hamiltonian of the system which by integrating out the strain fields and expanding ϕ around 0.5, they finally derive the following equation for the Hamiltonian in the ground state

$$H \;=\; \int_r m \cdot [\phi(r) - \frac{1}{2}]^2 \;+\; u \cdot [\phi(r) - \frac{1}{2}]^4 \tag{5.36}$$

where $m = 2T - a - \frac{2 \cdot K \cdot n^2}{1-\nu}$ and $u = \frac{4T}{3}$ [20].

The free energy can be determined by evaluating the Hamiltonian within mean field theory, by setting

$$\frac{dH}{d\phi(r)} \;=\; 0$$

then ΔF(x)=H[$\phi(s)$] where $\phi(s)$ are the solutions of the equation above.

Moreover, in order to evaluate the contribution that comes for optical irradiation, we need to add another term to the Hamiltonian. By following the deformation potential theory for electron-phonon interactions [20, 77], the lowest order coupling between excess charge density and the strain and

composition fields is used [20]

$$H_{eff} \;=\; \int_r a \cdot \Sigma(r) \cdot \left|\psi(r)\right|^2 \;+\; \epsilon \cdot \phi(r) \cdot \left|\psi(r)\right|^2 \tag{5.37}$$

where a is a dimensionless electron-phonon coupling constant and ϵ is the energetic bias of an excess charge to localize on the I-rich regions while $\left|\psi(r)\right|^2$ is the excess charge density [20]. The final formula of the Hamiltonian in the excited state with $\epsilon = 0$ is

$$H \;=\; \int_r m \cdot [\phi(r) - \frac{1}{2}]^2 \;+\; u \cdot [\phi(r) - \frac{1}{2}]^4 \;-\; g \cdot \left|\psi(r)\right|^2 \cdot [\phi(r) - \frac{1}{2}] \tag{5.38}$$

where $g = 2a|n|$ and $n = \frac{dlna}{d\phi}$. In order to evaluate the free energy, the phase diagram and the extent of demixing, the mean field approximation can be used as done before for the ground state [20].

The theoretical formalism above was applied to a $MAPb(I_{0.1}Br_{0.9})_3$ perovskite film. The results are shown in Figure (5.4).

From the phase diagram (x-T diagram, Figure 5.4) we observe that the miscibility gap at room temperature dictates the phase segregation of the mixed state into two phases, one phase with x$\sim$0.2 (x is the Br concentration). This is consistent with the previous experimental findings which show that the I-rich phase of all segregated $MAPb(I_{1-x}Br_x)_3$ films, independent of x, is comparable to x$\sim$0.2 ($MAPb(I_{0.8}Br_{0.2})_3$ at room temperature [17]. The phase diagram also confirms that the $MAPb(I_{1-x}Br_x)_3$ films are unstable under illumination at room temperature for wide range of x concentration. In the Figure (5.4 c) we notice that, by lowering the constant a of coupling, it is possible to mitigate the phase segregation at room temperature. In order to confirm that, they composed a $CsPb(Br_{0.1}I_{0.9})_3$ film. Since caesium (Cs^+) is less polar than methylammonium (MA^+), the corresponding electron-phonon coupling of the system is expected to be reduced. The re-

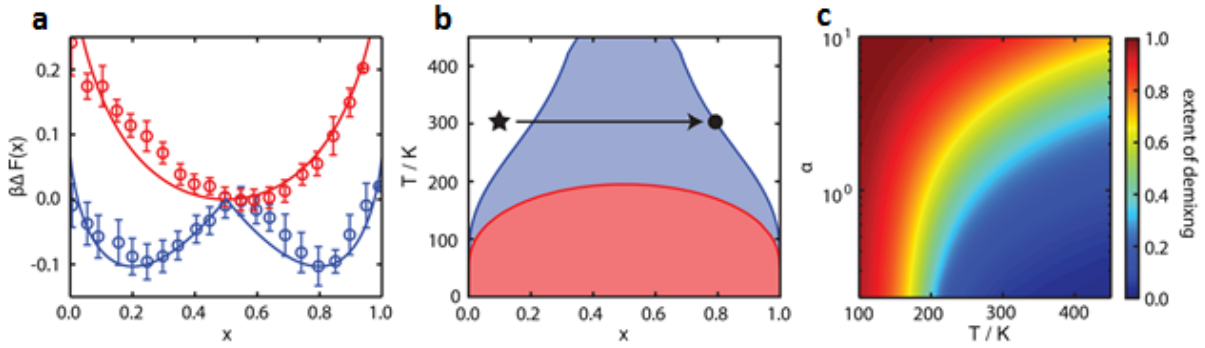

Figure 5.4: a) Free energies per unit cell for $MAPb(I_xBr_{1x})_3$ with varying composition in the ground (red) and photoexcited (blue) states, computed from MD simulations (circles) and mean field theory (solid lines). (b) Mean field theory temperaturecomposition phase diagram in the ground (red) and photoexcited state (blue) with the path through the phase diagram from initial state (star) to demixed state (circle) observed experimentally. Areas beneath the red and blue coexistence curves indicate demixed states. (c) The extent of demixing (i.e., purity of demixed regions found by tracing the blue coexistence curve in b) as a function of electronphonon coupling and temperature, computed from mean field theory in the photoexcited state. *Source of the Figure 5.4* : [20]

sults show as expected a smaller phase segregation rate than the one obtained from $MAPb(I_{1-x}Br_x)_3$ films [20].

To conclude, this theory considers polaron-induced deformation field as the driving force for halide phase segregation. Upon light excitation the weakly bound electron-hole pairs (E_x ~0.03eV [54]) dissociate and the free charge carriers deform the surrounding lattice through strong electron-phonon coupling, which enables the anion migration and leads to the formation of Br-rich and I-rich phases. The carriers are localized in the phase with the lowest energy band gap, forming polarons which continuously accumulate more iodide into these clusters.

The continuous growth of these clusters stops when they reach a maximum size which is determined by the deformation region of the polaron, and also, the number of clusters is limited by the number of photo-generated carriers. The model also uses simulations which have predicted an average size for I-rich domains roughly 8nm and a binding energy for the polaron roughly 0.08eV [20].

5.5 The Role of Cohesive Energy in Light-Induced Phase Segregation

Following the thermodynamic model based on nucleation, Wang et al. [23] consideration was to add the cohesive energy at interfaces as an extra contribution to the free energy of the system. With this assumption, the free energy can be described as

$$\Delta G_{dark}(x,T) \;=\; \frac{4}{3}\pi\cdot r^3\cdot[\Delta h_{mix}(x,T) - T\cdot\Delta s_{mix}(x,T)] - r^2\cdot\sum_i c_i W_i \quad (5.39)$$

where the first two terms are the volumetric enthalpy and entropy respectively, and the third term refers to all cohesive energies, W_i and c_i are coefficients [23].

After optical illumination, the localized polarons bring in excessive strain energy (ΔG_s) and the difference in free energy in the excited state is given as

$$\Delta G_{light}(x,T) \;=\; \Delta G_{dark}(x,T) \;+\; \frac{4}{3}\pi\cdot r^3\cdot\Delta g_s(x) \quad (5.40)$$

where x is the bromide concentration and Δg_s is the strain energy per volume. The following Figure (5.5) shows how the excited carriers cause local distortion to the lattice.

The strain energy (per volume) is given by [23]

$$\begin{aligned}\Delta g_s \;=\; 4\mu_{mix}(\frac{\delta}{a})^2 \;-\; (1-x)\cdot 4\mu_I\cdot(\frac{(a+\delta)-a_I}{a_I})^2 \\ -\; x\cdot 4\mu_{Br}\cdot(\frac{(a-\delta)-a_{Br}}{a_{Br}})^2\end{aligned} \quad (5.41)$$

where a, a_I and a_{Br} are the initial lattice constants for the pseudo-cubic lattice of $CsPb(I_{1-x}Br_x)_3$, $CsPbI_3$ and $CsPbBr_3$ respectively, in dark, $\mu_{mix}, \mu_I, \mu_{Br}$ are the shear modulus of $CsPb(I_{1-x}Br_x)_3$, $CsPbI_3$ and $CsPbBr_3$ respectively, notice that all of these parameters are determined through experiments in $CsPb(I_{1-x}Br_x)_3$ films , and at last δ is the shrink or expand of the lattice constant after light excitation. A value of δ=0.15Ang was used.

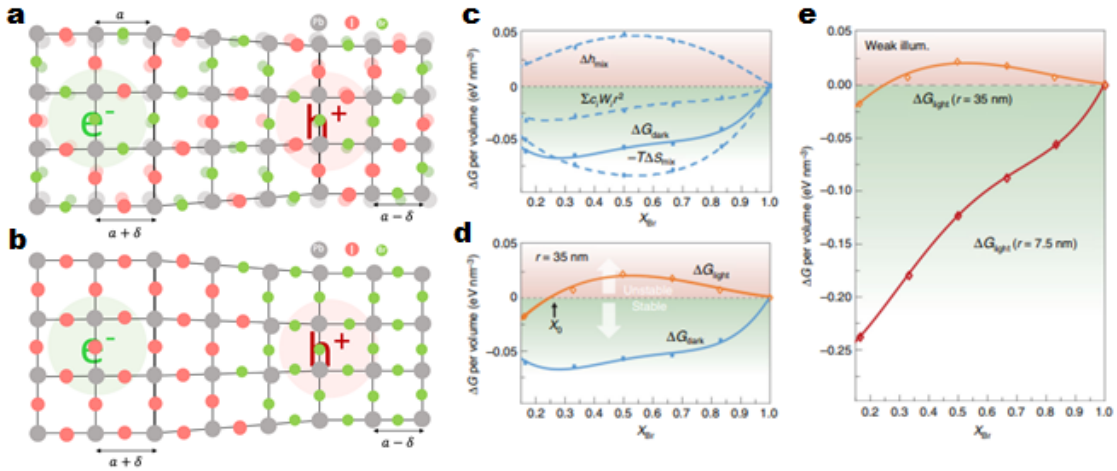

Figure 5.5: **a-b)** Schematic illustration of the distortion of the lattices in the presence of photo-generated carriers. **a)** In the ground state (dark) the lattices were displayed by the faded-colored dots with pseudo-cubic lattice constant a while under light excitation, the lattices were distorted due to the interaction of the free carriers with the lattices (forming polarons) leading to the change of lattice constant $a \pm \delta$. **b)** The photo-induced distortion in the lattices would drive the smaller Br^- anions to the lattice-compressed region and the larger I^- anions to the lattice-expanded area to release the localized strain energy. **c)** The calculated ΔG_{dark} per volume (solid line) is negative regardless of the Br content. The dashed lines show the calculated volumetric enthalpy Δh_{mix}, volumetric entropy term $T\Delta s_{mix}$, and the cohesive energy. A relatively large grain size was used here (r = 35 nm). **d)** Under illumination, the calculated free energy ΔG_{light} becomes partially positive assuming the same grain size. A threshold composition x$\sim$ 0.3 divides the mixed-halide perovskites into stable (I-rich) and unstable (Br-rich) regions. **e)** To mimic the experimental conditions of the $CsPb(Br_xI_{1-x})_3/Cs_4Pb(Br_xI_{1-x})_6$ composites, a small grain size (r = 7.5 nm) was assumed and the cohesive energy was considered. *Source of the Figure 5.5* : [23]

The mixing enthalpy and entropy were calculated in the same way as in the previous models, the only difference is that the current model assumes ideal mixing in entropy (without a term proportional to $\overline{x_j} \cdot \ln \overline{x_j}$, see Eq.(5.26)). The cohesive energies were evaluated from (DFT) calculations. For instance, the cohesive at the $CsPbBr_3/CsPbI_3$ interface is given by

$$W_1 \;=\; \frac{E_{CsPbI_3+CsPbBr_3} \;-\; (E_{CsPbI_3} + E_{CsPbBr_3})}{2A} \tag{5.42}$$

where $E_{CsPbI_3+CsPbBr_3}$ is the total energy at the ground state, E_{CsPbI_3} and E_{CsPbBr_3} are the total energies of the individual pure compounds at the ground state, while A is the relaxed interfacial area. The cohesive energy W_1 was evaluated to have a value of $W_1 = 0.43eV \cdot nm^{-2}$ at the $CsPbI_3/CsPbBr_3$ interface.

Figure (5.5 a) depicts the lattice distortion caused by polarons, followed by a change in the lattice constant $a \pm \delta$ (shrink or expand), where Figure (5.5 b) shows that the distortion in the lattice would drive the bromide anions, which are smaller and have less mass compared to iodide anions, to the lattice-compressed region and the iodide anions to the lattice-expanded region, releasing the localized strain energy [23].

The diagrams in figure 5.5(c-e) were obtained, by applying the theoretical model described above, in the following two systems, the first consists of a typical $CsPb(I_{1-x}Br_x)_3$ film and the second contains nanocrystals of $CsPb(I_{1-x}Br_x)_3$ embedded in the $CsPb(Br_xI_{1-x})_6$ matrix.

In the case of the $CsPb(I_{1-x}Br_x)_3$ film, only one cohesive energy is assumed and comes from the $CsPbBr_3/CsPbI_3$ interface before and after illumination while for the domain size (grain size) the value of r=35nm was used. On the other hand, in the case of nanocrystals, the $CsPb(Br_xI_{1-x})_3/Cs_4Pb(I_{1-x}Br_x)_6$, $CsPbBr_3/CsPbI_3$ and $CsPbBr_3/Cs_4Pb(I_{1-x}Br_x)_6$ interfaces are assumed, which further increase the total cohesive energy and a value of r=7.5nm for the domain size of nanocrystals was used. The domain sizes were experimentally evaluated, and weak illumination is relatively near the intensity of one Sun [23].

From Figure (5.5 c-e) one can observe that under light excitation at room temperature, the film is unstable and phase separation occurs, but the nanocrystals instead (with the same conditions) remain stable under weak illumination. These were confirmed by photoluminescence measurements in these specific samples [23]. These results are attributed to the different sizes of the domains r. While all the terms in the free energy are proportional to the volume of the domains ($\propto r^3$), the cohesive energy is a function of the area ($\propto r^2$) and this means that the interface-to-volume ratio is sufficiently large for the smaller domain size, which leads to the domination of the cohesive energy over the total energy of the system and which can eliminate the photo-induced phase segregation [23]. Notice that the total free energy includes the cohesive energy with a minus sign because the cohesive energy at interfaces is not in favor of segregating the mixed halide perovskite phase, but instead reduces the total free energy. Large cohesive energies can effectively suppress and eliminate the phase segregation.

Consequently, the only way to make the cohesive energy dominate the total energy is by reducing the domain size. Under strong illumination, the excessive lattice strain will be of greater magnitude and could still provoke phase separation by shifting the free energy (ΔG_{light}) into the positive region where $\Delta G_{light} > 0$.

Chapter 6

Experimental Methods

In the experiments of this work, a $FA_{0.5}MA_{0.5}Pb(I_{0.5}Br_{0.5})_3$ perovskite thin film was used. The perovskite solution was spin-coated on a glass substrate, forming a perovskite layer, which was annealed at 65^0C for 5 minutes. The resulting sample has a thickness of 370nm.

The photoluminescence (PL) measurements were performed by exciting the sample with a 325nm (CW) laser of power 25mW, focused to a diameter of 100µm. The excitation source is a He-Cd laser. In order to vary the incident power density, neutral density filters (ND) were applied. The emission of the sample is collected with a converging lens and guided to the entrance slits of a spectrograph with 600 grooves/nm diffraction grating and a CCD camera, after passing through a long pass UV filter (350nm), which blocks the excitation laser scattering. The emission (PL) spectra were recorded using the liquid-nitrogen-cooled CCD camera.

For the reflectance measurements, a Halogen lamp (200-1100 nm) was used to probe the sample. The sample's reflection is collected with a converging lens and guided to the same spectrograph. In order to obtain the reflectance, we compare the reflection intensity of the sample to the reflection intensity of a reference sample (a mirror with 99% reflectivity), by dividing the two intensities. The angle between the incident light and the unit vector perpendicular to the plane of the sample, is a few degrees near (normal incidence).

The time-resolved photoluminescence measurements were performed with a time-correlated single photon counting (TCSPC) system, and by exciting the sample with a 410nm pulsed femtosecond laser with an 80MHz repetition rate, focused by a microscope objective to a diameter of 2µm.

For the temperature control in the temperature-dependent measurements,

we make use of a closed cryostat with a manually operated temperature controller. The sample was mounted to a copper cold finger, in the vacuum.

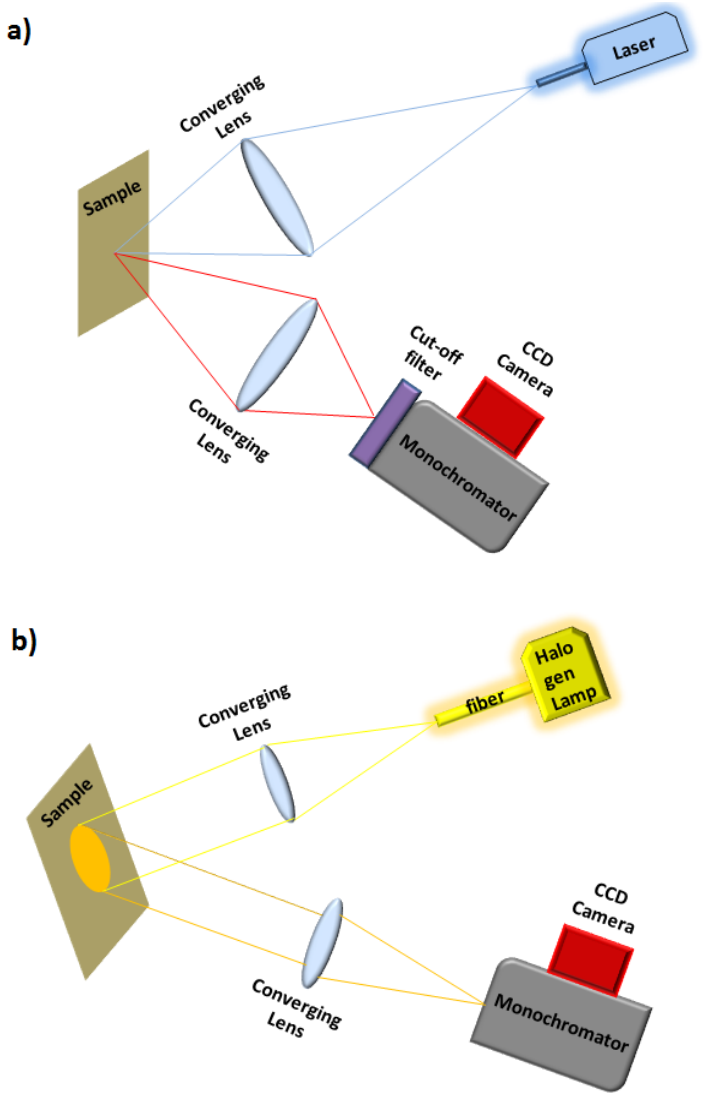

Figure 6.1: Schematic illustration of the experimental setup for a) PL measurements and b) Reflection measurements.

Chapter 7

Experimental Results

7.1 Emission characteristics of $FA_{0.5}MA_{0.5}Pb(I_{0.5}Br_{0.5})_3$ Perovskite Thin Film

In this part, we focus on the optical response of a $FA_{0.5}MA_{0.5}Pb(I_{0.5}Br_{0.5})_3$ thin film, presenting some of the main features of such a class of material.

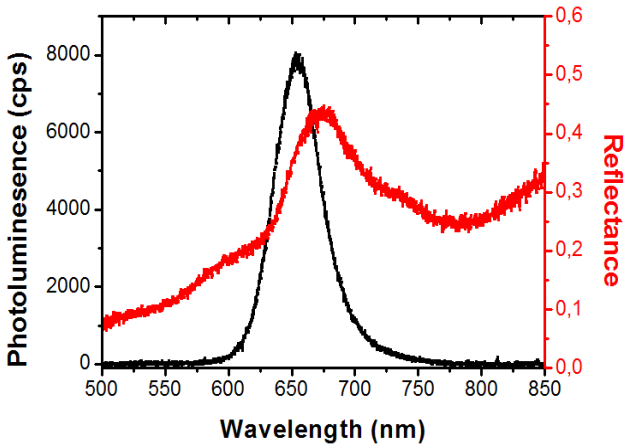

Figure 7.1: Photoluminescence (black line) and Reflectance (red line) spectra of a $FA_{0.5}MA_{0.5}Pb(I_{0.5}Br_{0.5})_3$ thin film, at room temperature. The PL spectra obtained by exciting the sample with a (CW) UV laser with 325nm excitation wavelength and 3.2W/cm^2 excitation intensity. The PL spectrum is obtained by 1sec exposure.

To begin with, the energy band gap of this perovskite should lie at $\sim$ 1.90eV (650nm) at room temperature, based on the corresponding experimental measurements of the $MAPb(I_{0.5}Br_{0.5})_3$ and $FAPb(I_{0.5}Br_{0.5})_3$ energy band gaps, shown in Figure 2.2a) (in Section 2.1). In Figure (7.1), we notice the emission wavelength at around 650nm, which is in agreement with the aforementioned statement. The reflectivity spectrum is also marked by an excitonic feature at 650nm, confirming that the PL emission is of excitonic near-band gap origin.

7.1.1 Temperature-dependent Photoluminescence

Here, we present the photoluminescence spectra of the $FA_{0.5}MA_{0.5}Pb(I_{0.5}Br_{0.5})_3$ thin film with varying temperature, using a 325nm (CW) laser with excitation intensity of $I_{exc} = 3.2$ W/cm^2, as excitation source. In Figure 7.2(a,c), we observe the red shift of the energy band gap with decreasing temperature. The energy band gap of semiconductors can be shifted by varying the temperature due to the expansion or contraction of the crystal lattice and the electron-phonon interaction, which is influenced by changes in the temperature. According to these effects, Varshni derived an empirical expression for the temperature-dependent energy band gap, which describes the reduction of the energy band gap with increasing temperature. This is inconsistent with our experimental results, which are in accordance with the literature, and is attributed to the positive band gap deformation potential ($a_\nu = \frac{\partial E_g}{\partial ln v}$, where v is the volume) of hybrid perovskites [78]. In addition, perovskites undergo phase transitions with respect to temperature, which also induce spectral shifts. Furthermore, in Figure 7.2a) we observe two emission peaks at low temperatures, which are also observed in $FA_{0.5}MA_{0.5}PbI_3$ perovskite and are attributed to bound (acceptor/donor) and free exciton radiative recombination [79].

Moreover, in Figure 7.2b), we observe the decreasing emission intensity of the main peak by increasing the temperature, in a non-linear fashion. This is likely to occur due to non-radiative mechanisms related to the presence of defects. Shallow states yield at low temperatures due to the enhanced

capability of trapping charge carriers, due to the reduced mobility of carriers. At low temperatures, the mobility of charge carriers increases due to the reduced density of phonons, while it decreases due to shallow states, which can efficiently trap carriers.

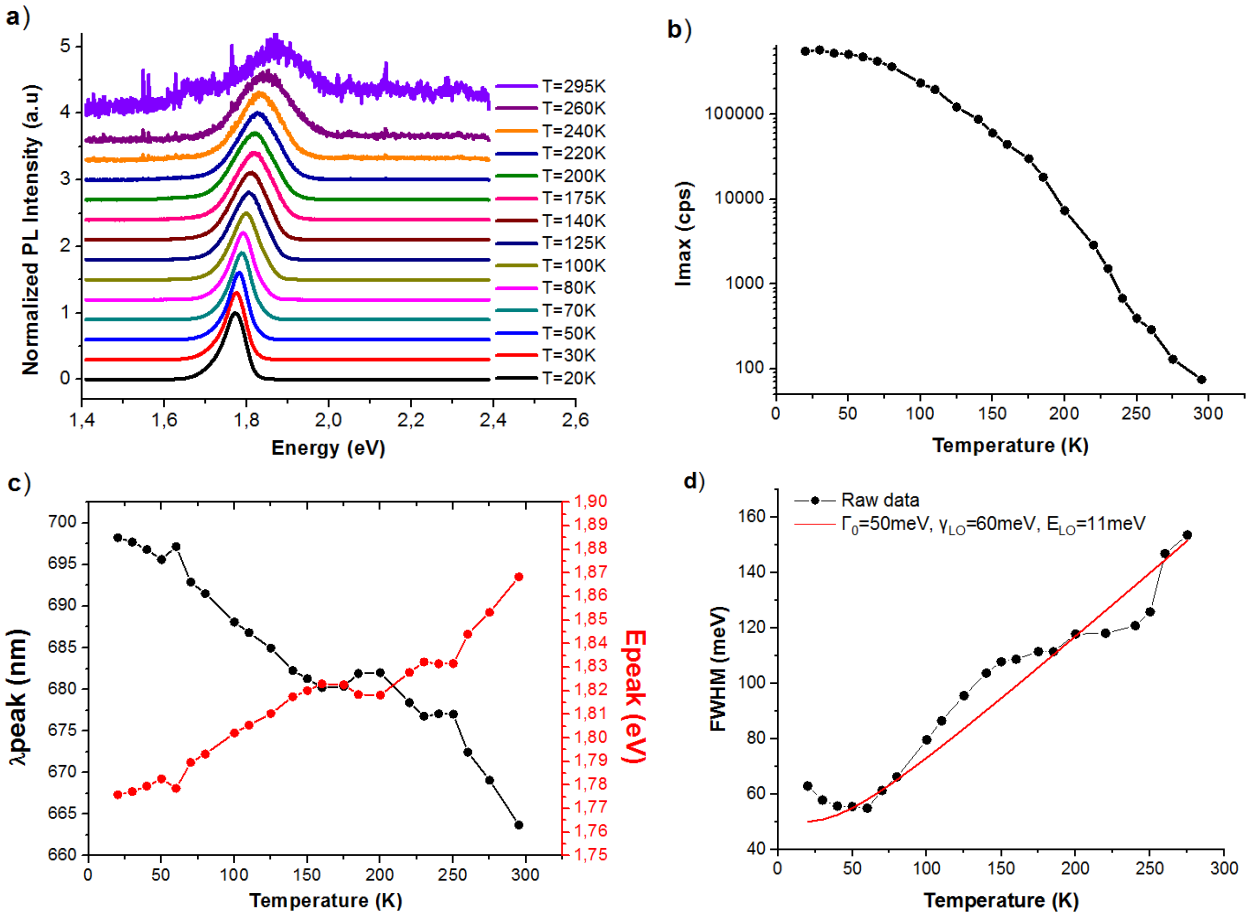

Figure 7.2: Temperature-dependent emission characteristics of $FA_{0.5}MA_{0.5}Pb(I_{0.5}Br_{0.5})_3$ perovskite film, using a (CW) laser at 325nm excitation wavelength with excitation intensity of $3.2W/cm^2$. a) Normalized PL intensity spectra at various temperatures (from 20K to 300K), which are vertically plotted for clarity, b) PL intensity of the emission peak as a function of temperature, c) Position of the emission peak in the energy (wavelength) axis as a function of temperature, d) Full width at half maximum (FWHM) of the emission peak as a function of temperature. The raw data is represented by black dots, while the red line represents the total PL linewidth $\Gamma(T)$ (main text) using the typical values mentioned in the main text.

At room temperature instead, the thermal energy allows them to overcome the small potential barrier of a shallow state, so the carriers are detrapped and are more prone to non-radiative traps. Hence, shallow states can enhance the PL intensity with decreasing temperature. Also, excitons, which are dissociated at room temperature, is another mechanism reducing the PL intensity at high temperatures. Additionally, in Figure 7.2c), we observe an abrupt change in the energy of the main PL peak at around 250K, which may indicate a phase transition. Notice that the $FA_{0.5}MA_{0.5}PbI_3$ perovskite also exhibits a cubic to tetragonal phase transition at 250K [79].

Finally, the full width at half maximum (FWHM) increases with decreasing temperature, as is shown in Figure 7.2d). This behavior is in accordance with that of other studied hybrid perovskites in the literature [35, 75, 80]. The PL linewidth broadening with respect to temperature is attributed to the inhomogeneous broadening due to imperfections, strain inhomogeneities, and the homogeneous broadening that arises from longitudinal optical (LO) phonon (Frohlich) scattering. The first mechanism is constant (Γo) with respect to temperature, while the latter is temperature-dependent and follows the Bose-Einstein distribution $\gamma_{LO}/[e^{E_{LO}/kT}\text{-}1]$, where γ_{LO} is the charge carrier-phonon coupling strength, while E_{LO} is the energy of a (LO) phonon, which depends on the frequency, and k is the Boltzmann's constant. The final PL linewidth $\Gamma(T)$ can be expressed as

$$\Gamma(T) = \Gamma o + \frac{\gamma_{LO}}{e^{\frac{E_{LO}}{kT}} - 1}$$

These are the two main contributions to the total PL linewidth $\Gamma(T)$. The contribution from scattering due to acoustic phonons is found to be weak ($\sim$ 20% of the total linewidth at room temperature) and thus negligible [75]. Typical values (in the literature) for γ_{LO} and E_{LO} are $\gamma_{LO} \approx$40meV for $FAPbI_3$ and $MAPbI_3$, and $\gamma_{LO} \approx$60meV for $FAPbBr_3$,$MAPbBr_3$, while the E_{LO} ranges from 11meV to 15meV in these perovskite materials.

7.1.2 Fluence-dependent Photoluminescence

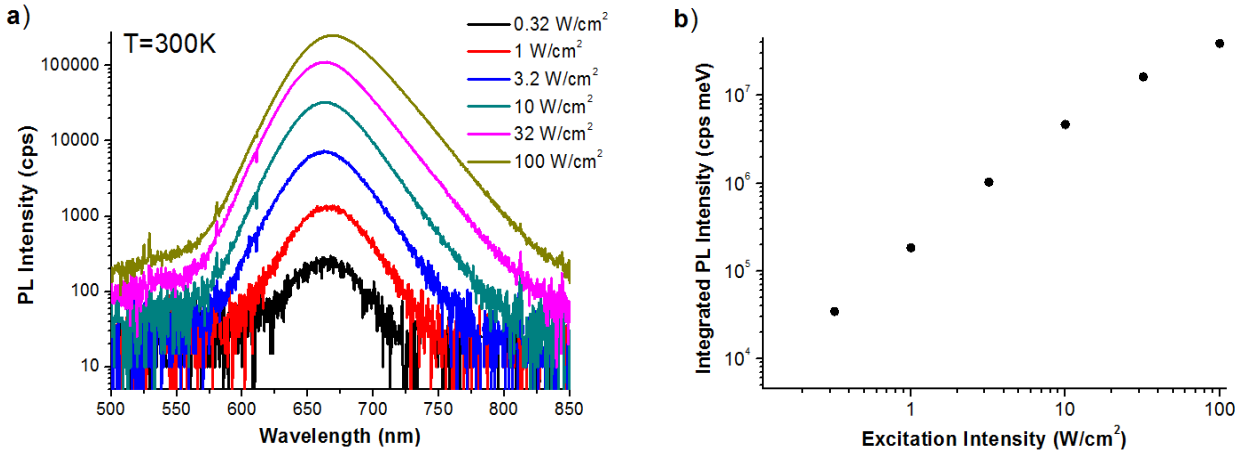

Figure 7.3: a) Excitation intensity dependence of the photoluminescence PL intensity of the perovskite film, using a (CW) laser with 325nm excitation wavelength, b) Integrated PL intensity of the emission peak at various excitation intensities.

In the absence of non-radiative recombination centers, the PL peak intensity increases linearly with increasing excitation intensity. In comparison, Figure 7.3b) shows a non-linear dependence of PL peak intensity on the excitation intensity, at room temperature, confirming the existence of the non-radiative recombination centers in the $FA_{0.5}MA_{0.5}Pb(I_{0.5}Br_{0.5})_3$ perovskite.

7.1.3 Photoluminescence (PL) Mapping

In this part, we performed PL measurements at different positions in the sample with a constant excitation intensity of $3.2 W/cm^2$ at room temperature, in order to observe possible shifts in the PL peak wavelength and

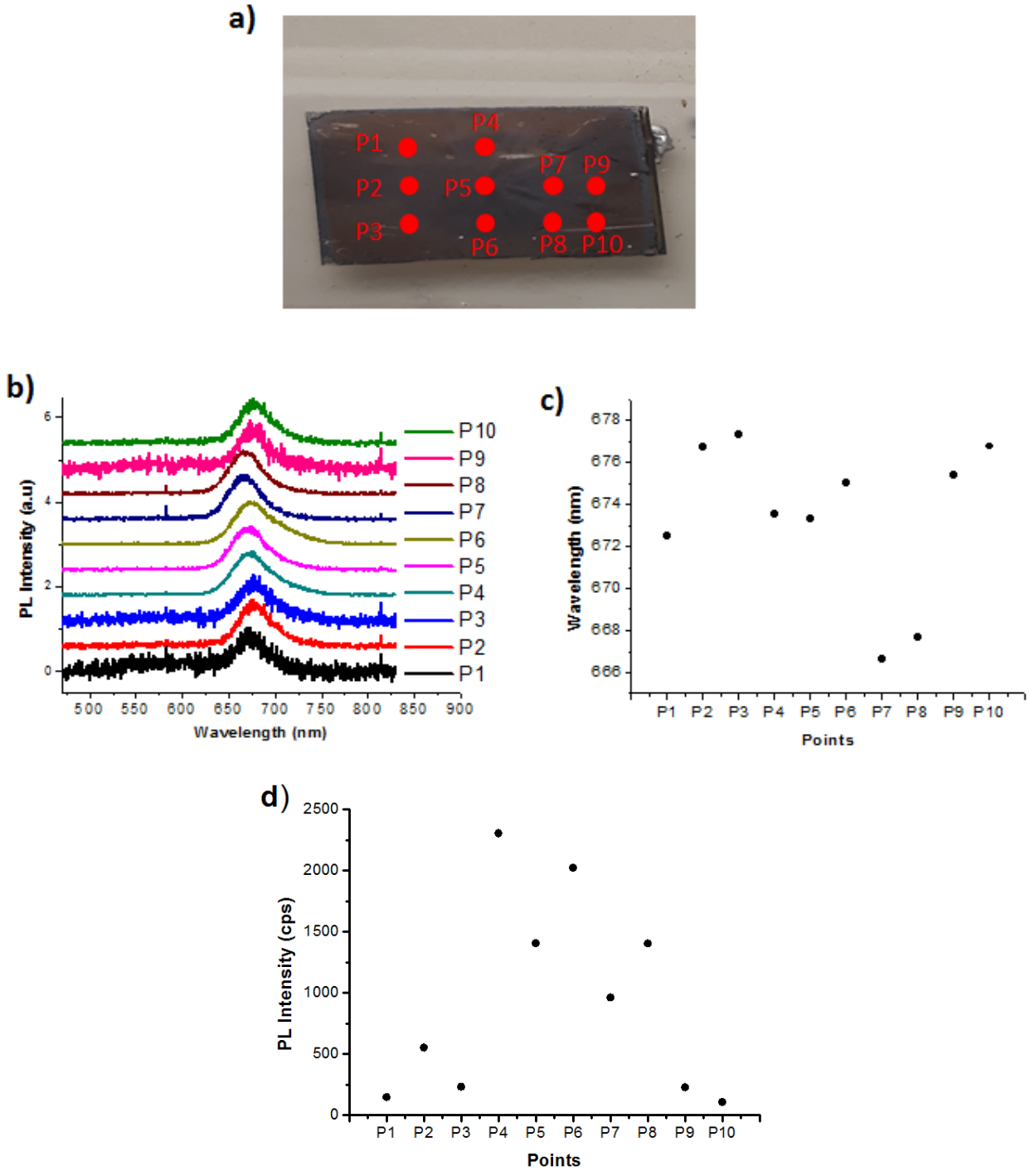

Figure 7.4: Photoluminescence (PL) mapping is performed at different positions in the $FA_{0.5}MA_{0.5}Pb(I_{0.5}Br_{0.5})_3$ thin film, using a (CW) laser at 325nm excitation wavelength with $3.2W/cm^2$ excitation intensity. a) Image of the $FA_{0.5}MA_{0.5}Pb(I_{0.5}Br_{0.5})_3$ perovskite film, which depicts the selected points for PL mapping. The distance between neighboring points is about 5-10mm, b) Normalized PL intensity spectra at different positions in the film, c) PL emission peak wavelength at different points in the perovskite thin film, d) PL intensity of the emission peak at different points.

intensity. Figure 7.4 shows a macroscopic inhomogeneity, with a maximum shift of ∼10nm in the PL peak wavelength of the $FA_{0.5}MA_{0.5}Pb(I_{0.5}Br_{0.5})_3$ perovskite, which reflects the composition inhomogeneity across the sample. Furthermore, there are intensity variations from point to point, which reflect the sample inhomogeneity in terms of crystallinity and defect density. Inhomogeneity on such a macroscopic scale is commonly observed in perovskite films. It is worth noting that there may be some errors in the measurements due to the limitation in exposure time to light, which makes it difficult to record the maximum possible signal.

7.2 Emission Dynamics of $FA_{0.5}MA_{0.5}Pb(I_{0.5}Br_{0.5})_3$ Thin Film During Light-Induced Phase Segregation at Various Excitation Levels

In this section, we examine the time evolution of photoluminescence (PL) spectra in a $FA_{0.5}MA_{0.5}Pb(I_{0.5}Br_{0.5})_3$ perovskite thin film under light-soaking at various excitation intensities, with a 325nm excitation (CW) laser source, at room temperature.

Figure 7.5 shows the time evolution of PL spectra for a variety of excitation intensities. The total time interval of photoirradiation is 100 seconds. We can observe the co-existence of three perovskite phases within the film due to the phase segregation effect: mixed halide phase (at around 650nm), I-rich phase (at around 770nm), and Br-rich phase (at around 525nm). We also notice the differences in PL spectra at the corresponding times caused by the different excitation intensities. For instance, in Figure 7.5a, we observe the emission from the mixed and I-rich phases, with the mixed phase being dominant at earlier times, while at later times the I-rich phase emission is dominant. The emission of the Br-rich phase has insignificant PL intensity counts. In figure 7.5b instead, we observe the co-existence of the three phases with a significant emission intensity from the Br-rich phase, while the higher emission intensity corresponds to the I-rich phase, after a time interval of 100 seconds. Finally, in Figures 7.5c and 7.5d, we observe a significant emission intensity from the three phases at earlier photoirradiation times, while at later times the emission from the Br-rich phase becomes dominant (especially in Figure 7.5d). Moreover, we observe a gradual shift in the emission wavelength of the I-rich phase, with respect to time, which indicates the gradual increase of the iodide content in the I-rich regions until it reaches a maximum value, which has already been mentioned in the theoretical background. Noteworthy, the emission from the mixed perovskite phase decreases with respect to time, due to phase segregation, but does not vanish, indicating the partial phase segregation of the mixed phase. This result is in agreement with the experimental studies, shown in the introductory sections.

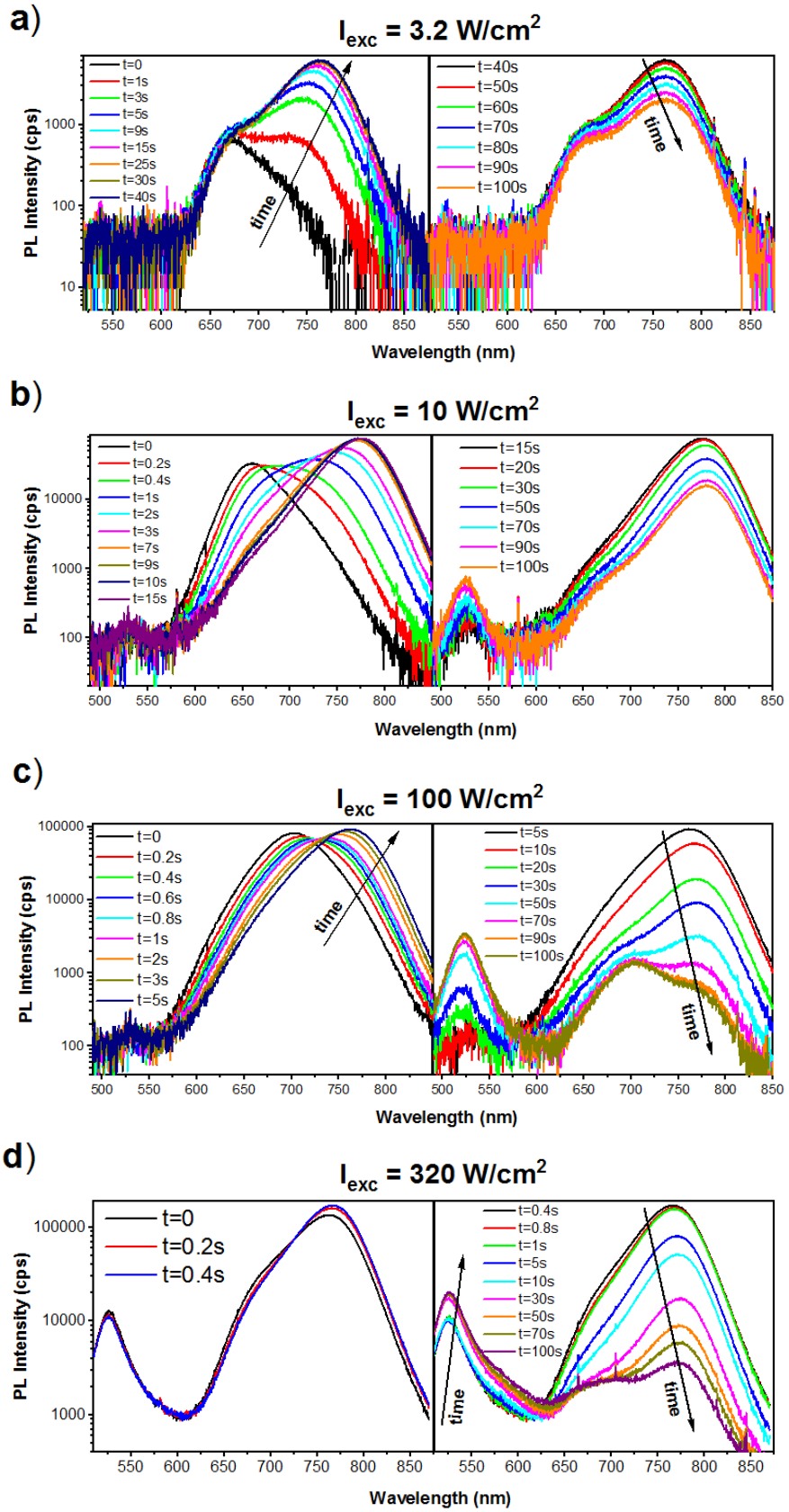

Figure 7.5: Time evolution of photoluminescence (PL) spectra of a $FA_{0.5}MA_{0.5}Pb(I_{0.5}Br_{0.5})_3$ perovskite thin film, excited by a 325nm (CW) laser at excitation intensity of a) 3.2W/cm^2, b) 10W/cm^2, c) 100W/cm^2 and d) 320W/cm^2, for a time interval of 100 seconds, at room temperature.

In order to examine the differences in emission spectra and to reveal the underlying mechanisms behind them, a more detailed analysis of the corresponding PL spectra, follows in the next figures.

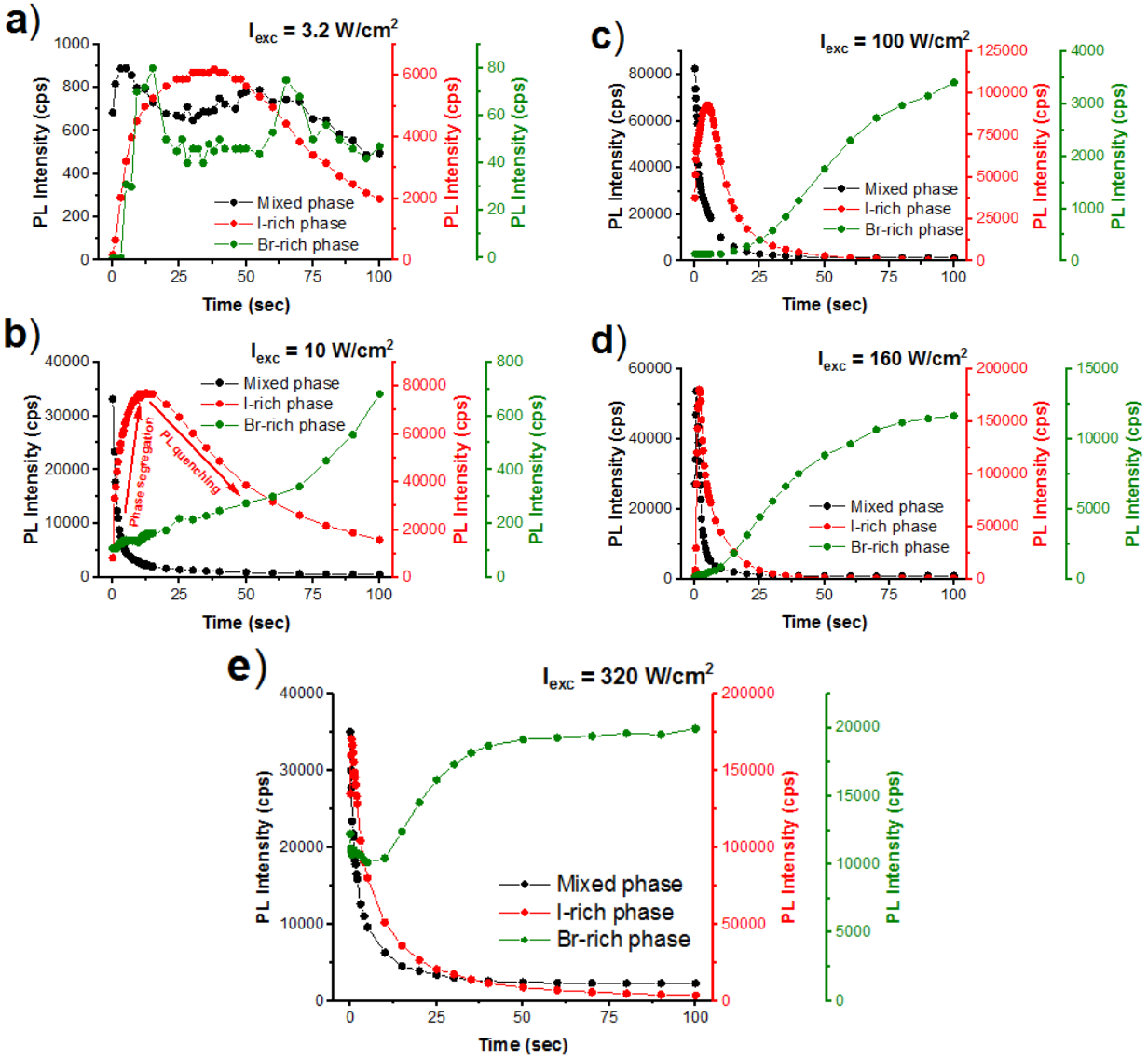

Figure 7.6: Photoluminescence (PL) intensity of the peaks that correspond to the Br-rich phase (green dots), Mixed phase (black dots), and I-rich phase (red dots) as a function of photoirradiation time, at excitation intensities of a) 3.2W/cm^2, b) 10W/cm^2, c) 100W/cm^2, d) 160W/cm^2 and e) 320W/cm^2.

Figure 7.6, shows the time evolution of the PL intensity of the three phases for different excitation intensities. In this Figure, we observe a specific behavior that is the same for each excitation intensity, but with different rates of change. Initially, in each case, the emission from the I-rich perovskite phase increases exponentially in intensity and dominates in the (PL) emission spectra. This is in accordance with the kinetic dynamics of phase segregation, discussed in the theory sections. When the intensity of the I-rich phase emission reaches a maximum value, it starts to decrease exponentially in intensity at a rate that is strongly dependent on the excitation intensity. The PL intensity quenching of the I-rich phase with the lowest energy band gap (potential minimum), gives rise to the Br-rich phase emission peak to increase in intensity and under condition dominate in the PL spectra. In Figure 7.6a we observe that the emission from the Br-rich phase fluctuates at low PL intensity counts, and at the time interval of 100 seconds, there is no increase in the emission, in contrast to the high excitation intensity cases in Figure 7.6(b-e). In order to explain that, we first need to focus on the Br-rich phase emission behavior at different excitation intensities. In Figure 7.6(b-e) we observe that when the emission from the I-rich phase starts to decrease with respect to time, it is not accompanied by an immediate increase in Br-rich phase emission but instead there is a delayed growth in the Br-rich phase emission. Specifically, we observed that only when the PL intensity from the I-rich phase is reduced to one fourth of the maximum PL intensity of the I-rich phase ($I \leq \frac{I_{MAX}}{4}$) approximately, we get a continuous increase in the Br-rich phase emission with time.

In order to further examine this observation, we increased the duration of photo-irradiation from 100 seconds to 300 seconds, while we also reduced the excitation intensity from 3.2W/cm^2 to 1.6 W/cm^2. In figure 7.7a we observe that the PL intensity of the I-rich phase is reduced to a value of 33% of I_{MAX} at t=100s and I_{exc}=1.6 W/cm^2, while in the case of I_{exc}=3.2 W/cm^2, the PL intensity is dropped to a value of 32% of I_{MAX} at t=100s. At t=130s (in the case of 1.6W/cm^2) the PL intensity of the I-rich phase is further reduced to a value of 24% of I_{MAX} and at this time the Br-rich phase emission intensity starts to increase. Thus, this means that if we extend the duration of photo-irradiation, there will be a continuous growth

of the Br-rich phase emission in intensity with respect to time, even at the low excitation intensities regime. Consequently, the Br-rich phase emission depends on the PL intensity quenching of the I-rich phase, which in turn depends on the quality of the film and the excitation intensity, and as such, there is a threshold excitation intensity below which the PL quenching rate of the I-rich phase emission is so low that it cannot lead to emission intensities of $I_{I-rich} \leq \frac{I_{MAX}}{4}$ in the limit of $t \to \infty$ and hence it cannot lead to an increase in the Br-rich phase emission, which will be constant (or fluctuate) at low PL intensity counts. This is a significant experimental result obtained by the current experimental work.

Figure 7.7b illustrates the observed mechanisms that take place during light-induced phase segregation. After the formation of Br-rich and I-rich phases within the film, the first stage includes the accumulation of photo-generated carriers in the potential minimum of the I-rich phase, which leads the emission of the I-rich phase to be dominant in the PL spectra. Afterwards, the second stage includes the band-filling effect and the PL intensity quenching of the I-rich phase, which under condition (relevantly high PL quenching rate) leads to the charge carrier recombination in the Br-rich phase and the corresponding emission becoming dominant in the PL spectra. The band-filling effect of the I-rich phase has also been reported in [41].

Moving forward, Figure 7.8 depicts the exponential fits to the experimental data. This allows us to obtain the phase segregation rate and the PL quenching rate at various excitation intensities. At low excitation intensities, we fit an exponential in the form of $I = I_{MAX}(1 - e^{-k_{forward,em}\ t})$, in order to evaluate the phase segregation rate, following the standard kinetic model that was presented in the theoretical part. At high excitation intensities, the experimental data is best fitted by an exponential in the form of $I = I_a - I_b(e^{-k_{forward,em}\ t})$. In order to obtain the (PL) quenching rate, we fit an exponential decay curve to the data, which is in the form of $I = I'_a + I'_b(e^{-k_{quenching}\ t})$, which can fit well to the data, at low excitation intensities. At the high excitation intensity regime, a double exponential decay curve is fitted to the data, due to the insufficient fit of a single exponential decay curve to the data. The results are shown in table 7.1.

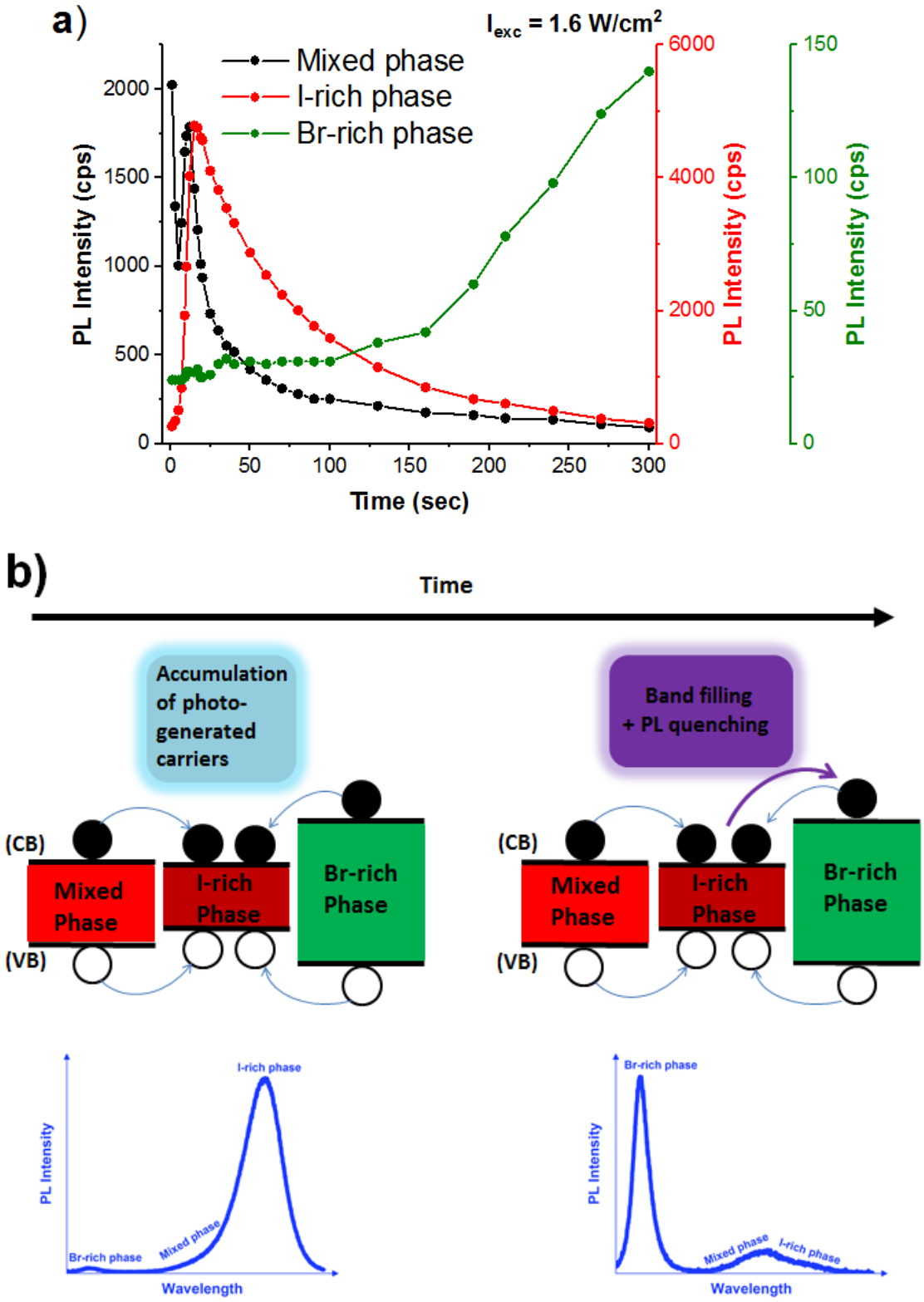

Figure 7.7: a) Photoluminescence (PL) intensity of the peaks that correspond to the Br-rich phase (green dots), Mixed phase (black dots) and I-rich phase (red dots) as a function of photo-irradiation time, at excitation intensity of 1.6W/cm^2, for a time interval of 300 seconds. b) A Schematic illustration of the mechanisms that affect the emission spectra of a phase-segregated perovskite thin film with time.

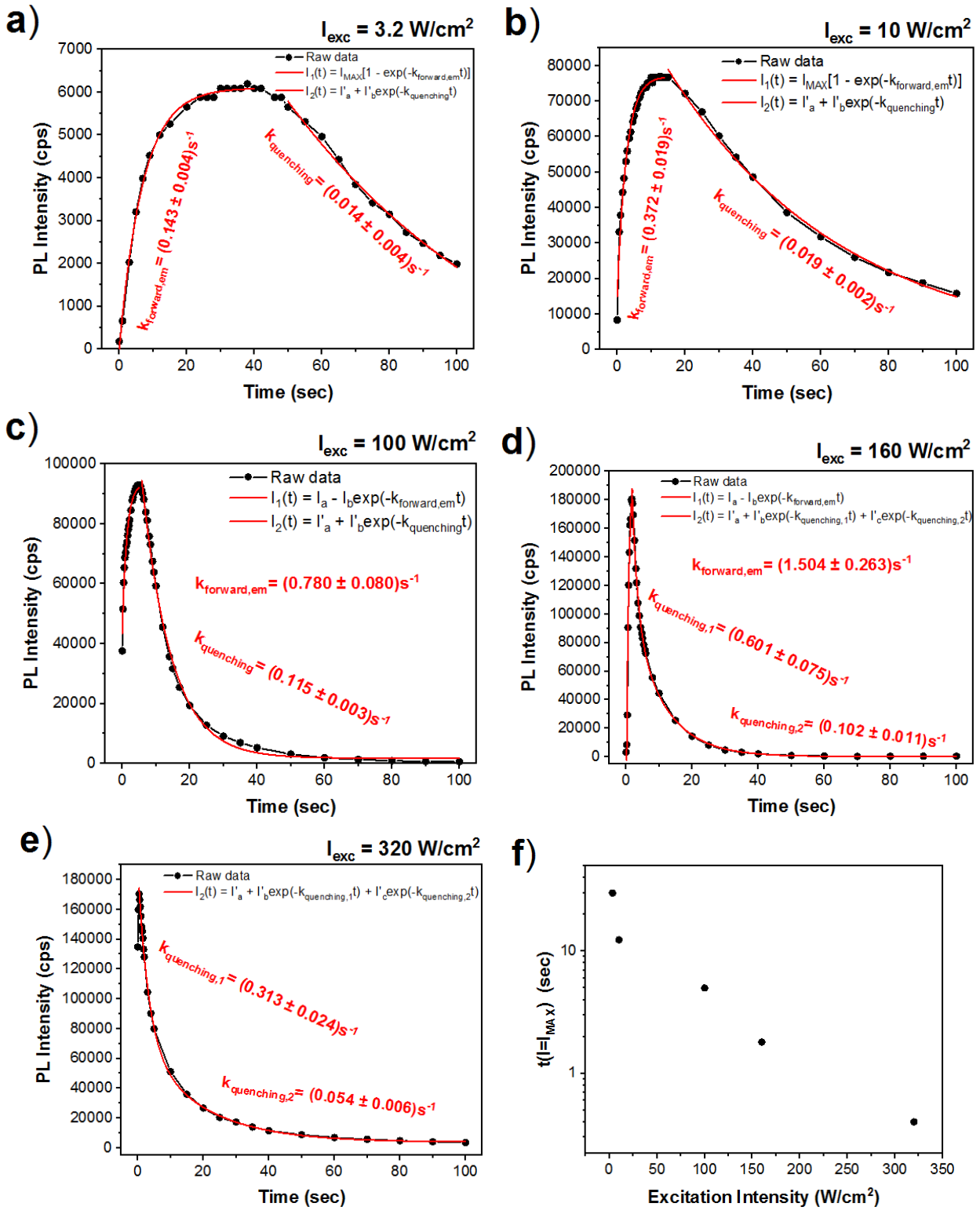

Figure 7.8: **(a-e):** Photoluminescence (PL) intensity of the peak, which corresponds to the I-rich phase of a phase segregated $FA_{0.5}MA_{0.5}Pb(I_{0.5}Br_{0.5})_3$ perovskite film, as a function of time, at various excitation intensities. Black dots correspond to the PL experimental data, while the red lines correspond to the exponential fittings as described in the text. **f)** The time at which the PL intensity of the I-rich phase reaches its maximum value as a function of excitation intensity.

I-rich phase			
Excitation Intensity	**Phase segregation rate** ($k_{forward,em} \pm \delta k_{forward,em}$) ($s^{-1}$)	**PL quenching rate** ($k_{quenching,1} \pm \delta k_{quenching,1}$) ($s^{-1}$)	**PL quenching rate** ($k_{quenching,2} \pm \delta k_{quenching,2}$) ($s^{-1}$)
3.2 W/cm^2	0.143 ± 0.004	0.014 ± 0.004	(−)
10 W/cm^2	0.372 ± 0.019	0.019 ± 0.002	(−)
100 W/cm^2	0.780 ± 0.080	0.115 ± 0.003	(−)
160 W/cm^2	1.504 ± 0.263	0.601 ± 0.075	0.102 ± 0.011
320 W/cm^2	(−)	0.313 ± 0.024	0.054 ± 0.006

Table 7.1: Phase segregation and PL quenching rates at various excitation intensities, obtained by exponential fits to the PL experimental data of the I-rich perovskite phase.

Remarkably, the phase segregation rate of the $FA_{0.5}MA_{0.5}Pb(I_{0.5}Br_{0.5})_3$ perovskite thin film is much lower than the phase segregation rate of a $MAPb(I_{0.5}Br_{0.5})_3$ perovskite thin film as reported in the literature, indicating that the double cation (FAMA) perovskite can efficiently suppress the halide phase segregation, in agreement with other experimental studies in the subject, which are mentioned in the theoretical background. For comparison purposes, the phase segregation rate of a $MAPb(I_{0.5}Br_{0.5})_3$ thin film at excitation intensity of 20 mW/cm^2 is approximately 0.71 s^{-1} (evaluated by [22]), while in our case this segregation rate occurs at an excitation intensity of roughly 100 W/cm^2 and the minimum value which is evaluated in our work is $k_{forward,em} = 0.14 s^{-1}$ at $I_{exc} = 3.2$ W/cm^2. Notice that the methodology

for extracting the value of phase segregation rate in $MAPb(I_{0.5}Br_{0.5})_3$ was the same.

Moreover, in Figure 7.8, we observe that by increasing the excitation intensity, the PL quenching rate increases, and interestingly it splits into two rate components, indicating that as the excitation intensity increases, there are likely more than one mechanism that contribute to the PL quenching effect. Finally, Figure 7.8f suggests an exponential dependence of the time at which the PL intensity of the I-rich phase reaches its maximum value, which is dependent on the phase segregation rate, as a function of excitation intensity. This exponential dependence of phase segregation rate on the excitation intensity, is predicted from the kinetic model in the theoretical background and is experimentally observed in [22].

Finally, it is worth noting that the observed experimental condition $I \leq \frac{I_{MAX}}{4}$ which was found at the relevantly low excitation intensity regime, was also tested in a second $FA_{0.5}MA_{0.5}Pb(I_{0.5}Br_{0.5})_3$ thin film, using the same excitation intensity, confirming this result. Even though reproducible experimental result, its origin remains ambiguous and might also depend on other factors, such as film preparation, quality of the film, and excitation intensity.

7.3 Photoluminescence Quenching Effect

In general, there are two plausible mechanisms that might be responsible for the observed photoluminescence quenching of the light-induced I-rich phase in the $FA_{0.5}MA_{0.5}Pb(I_{0.5}Br_{0.5})_3$ thin film. A gradual increase in the non-radiative recombination of charge carriers, in the I-rich phase, accompanied by a reduction in the radiative charge carrier recombination, is necessary to explain the reduced emission intensity and the PL quenching. A possible mechanism that can lead to PL quenching, is the degradation of the crystal lattice of the I-rich perovskite phase at high intensities. In the previous analysis, we observed that the PL quenching of the I-rich phase could increase the emission from the Br-rich phase. This is a significant insight that can be used to clarify the mechanism behind the observed PL quenching. An increase in the non-radiative carriers recombination, in the I-rich phase, would still provoke accumulation of photo-generated carriers in the I-rich phase due to its favourable energy band gap and the emission of the Br-rich phase should not increase with time. This implies that a mere increase in non-radiative recombination in the I-rich phase, cannot explain the increased emission of the Br-rich phase. On the other hand, a reduction in the number of I-rich regions within the film, instead, accompanied by the band filling effect, which can easily occur when the total number of I-rich regions is reducing with time, could efficiently lead to an increased emission in the Br-rich phase. Notice that the $MAPbI_3$ perovskite is known for its PL quenching behavior, especially at high excitation intensities. Specifically, previous works have shown that atmospheric molecules such as O_2 and N_2 (mainly the O_2) can be adsorbed on iodide vacancies (and Pb vacancies), on the perovskite surface, during light irradiation, leading to passivation of defects (PL enhancement), but also leading to increased electron-hole non-radiative recombination (deep-level defects) and PL quenching [81–83]. Other related works have shown that when a perovskite is in contact with a liquid solvent (or electrolyte solution), the iodine anions of the I-rich perovskite phase migrate and selectively dissolve into the solution, leading to an iodine expulsion that causes the depletion of iodine from the perovskite film, during

light irradiation [84–86]. The final phase-segregated perovskite is a Br-rich perovskite, and the process of iodine expulsion is irreversible. This process is also attributed to the halide anion migration of mixed halide perovskites, and contributes to the PL quenching effect by inducing crystal damages (decomposition of the I-rich phase) and by reducing the number of I-rich regions within the film.

In order to examine the influence of the surrounding atmosphere on the PL quenching effect of the I-rich phase emission, we conducted (PL) measurements in the $FA_{0.5}MA_{0.5}Pb(I_{0.5}Br_{0.5})_3$ thin film inside a cryostat. We mounted the perovskite thin film on a copper cold finger of a closed cryostat, which was connected with a vacuum pump, as mentioned in the experimental methods. We then illuminated the perovskite film with a UV Lamp with 385nm excitation wavelength and an excitation intensity of roughly 40 W/cm^2, at room temperature. The spot diameter on the film was 90 μm. The lamp was connected to a microscope with a PL camera, through which we also obtained PL images. Initially, the perovskite film was excited by the UV Lamp for 21 minutes in the air, in order to induce phase segregation. After 21 minutes of light excitation, the iodide-rich phase emission intensity is sufficiently reduced compared with earlier irradiation times, due to the PL quenching effect, while the Br-rich phase emission intensity is increased, as Figure 7.9a shows. At this time, we opened the vacuum pump and we conducted PL measurements over time.

At first, we observe the annihilation of the emission spectra after 5-6 minutes in vacuum. We conclude that chemical reactions between the perovskite and atmospheric molecules, are essential due to the efficient passivation of perovskite defects, which reduces the density of defect states and leads to PL enhancement. Moreover, we obtain a significant insight from Figure 7.9a, which shows that in the early times in vacuum, the emission from the I-rich phase immediately increases, which may reveals that the underlying mechanism of the PL quenching is related to the I-rich perovskite phase interaction with air molecules (such as O_2) or moisture.

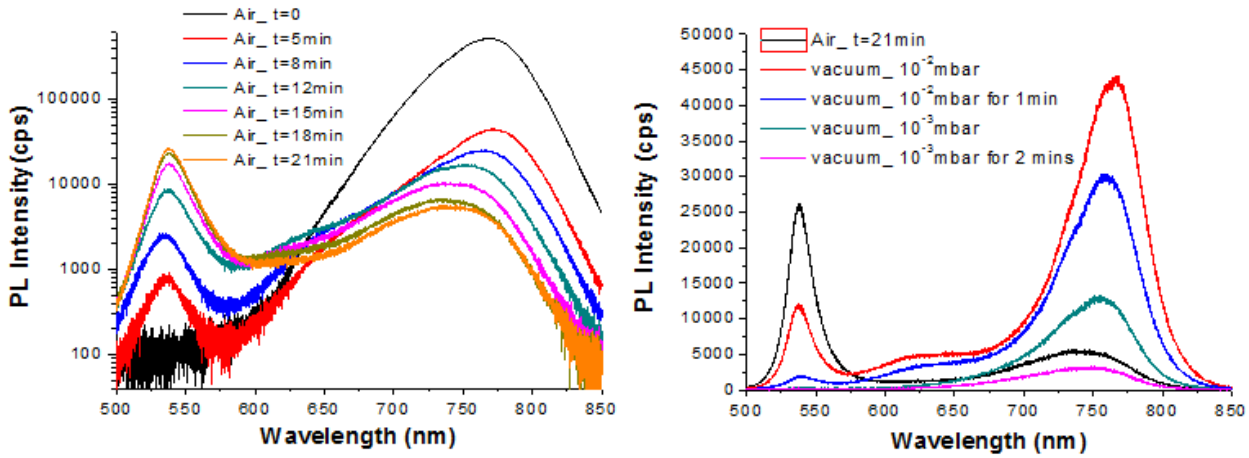

(a)

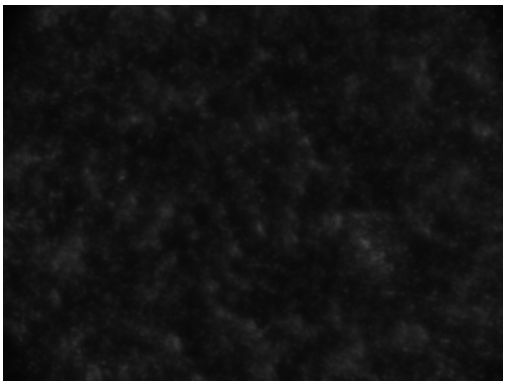

(b) t=21min in Air

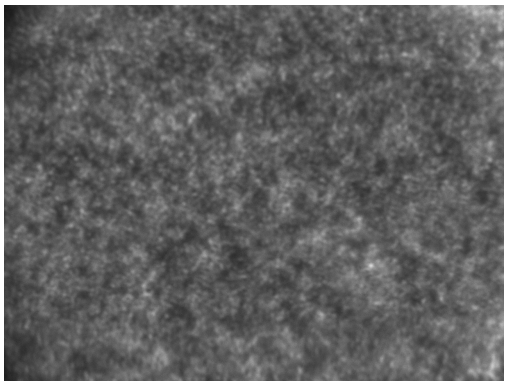

(c) 10^{-2}mbar in vacuum

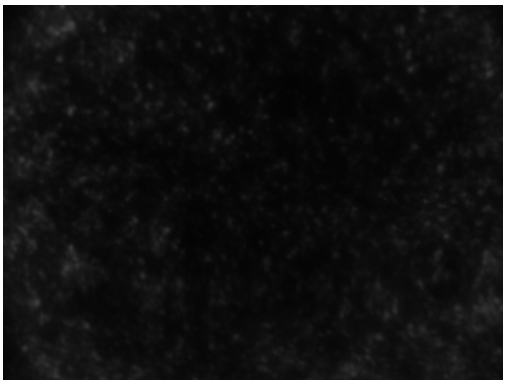

(d) 10^{-3}mbar in vacuum

(e) 10^{-3}mbar in vacuum for 2min

Figure 7.9: a) Time evolution of $FA_{0.5}MA_{0.5}Pb(I_{0.5}Br_{0.5})_3$ PL spectra, excited by a UV Lamp at 385nm excitation wavelength with 40W/cm^2 excitation intensity, at pressure of one atmosphere (left) and at pressure of 10^{-2}mbar, 10^{-3}mbar in vacuum (right). (b-e): PL images from an optical microscope with a PL camera, which is connected with the UV Lamp, at different photo-irradiation times in air and in vacuum. The images depict the 90x90μm^2 area of the UV Lamp's spot on the perovskite film.

In addition, it has been reported in the literature, that variations in the pressure can provoke changes in the phase segregation characteristics, such as changes in the phase segregation rate and in the final composition of the Br-rich and I-rich phases, which originate from the change in the enthalpy of the system due to the term $P\Delta V$. Thus, it is more likely that variation in pressure induces further phase segregation, which results in an increased number of I-rich domains within the film. The rise of the PL peak, which corresponds to the I-rich perovskite phase, originates from further phase segregation within the film. This result underlines the sensitivity of the phase segregation to pressure variations, and implies that this should be taken into account in the evaluation of the free energy of the system. In conclusion, it is still unclear if the observed quenched PL of the I-rich phase upon light excitation originates from the interaction of the perovskite with air molecules or moisture. A proposed experiment is to add a layer on top of the perovskite film, such as for example polymethyl methacrylate (PMMA) (in order to exclude the atmospheric effect) and study the emission behavior over time.

In the next experiment, we excite the $FA_{0.5}MA_{0.5}Pb(I_{0.5}Br_{0.5})_3$ perovskite thin film with a (CW) laser at 325nm excitation wavelength and 32 W/cm^2 excitation intensity, in order to induce halide phase segregation and we record the PL spectra at different irradiation times. At time $t=t_2$, the emission from the Br-rich perovskite phase is more intense compared to the emission from the I-rich phase due to the PL quenching of the I-rich phase emission with time (see Figure 7.10). For $t\geq t_2$ we increase the excitation intensity to 100 W/cm^2, in order to further excite the perovskite, which in turn leads to the further generation of Br-rich and I-rich domains within the film. In this way, we manage to increase the density of I-rich domains within the film, at a time of $t_3=t_2+dt$. As we can observe in Figure 7.10, the increased density of I-rich domains within the film led to an increase in I-rich phase emission and a decrease in Br-rich phase emission, indicating the partial diffusion of photo-generated charge carriers in the Br-rich phase into the newly generated I-rich domains in which they finally recombine. The emission from the I-rich perovskite phase also increases at $t=t_3$ due to higher excitation intensity, which leads to a higher concentration of charge carriers in the I-rich

perovskite phase. For $t=t_4 > t_3$, we observe once more, the PL quenching of I-rich phase emission, which is accompanied by an increase in Br-rich phase emission. This experiment reflects the strong dependence of the Br-rich emission on the I-rich emission behavior and enhances the possibility of an existing PL quenching mechanism that reduces the number of I-rich phase domains within the film.

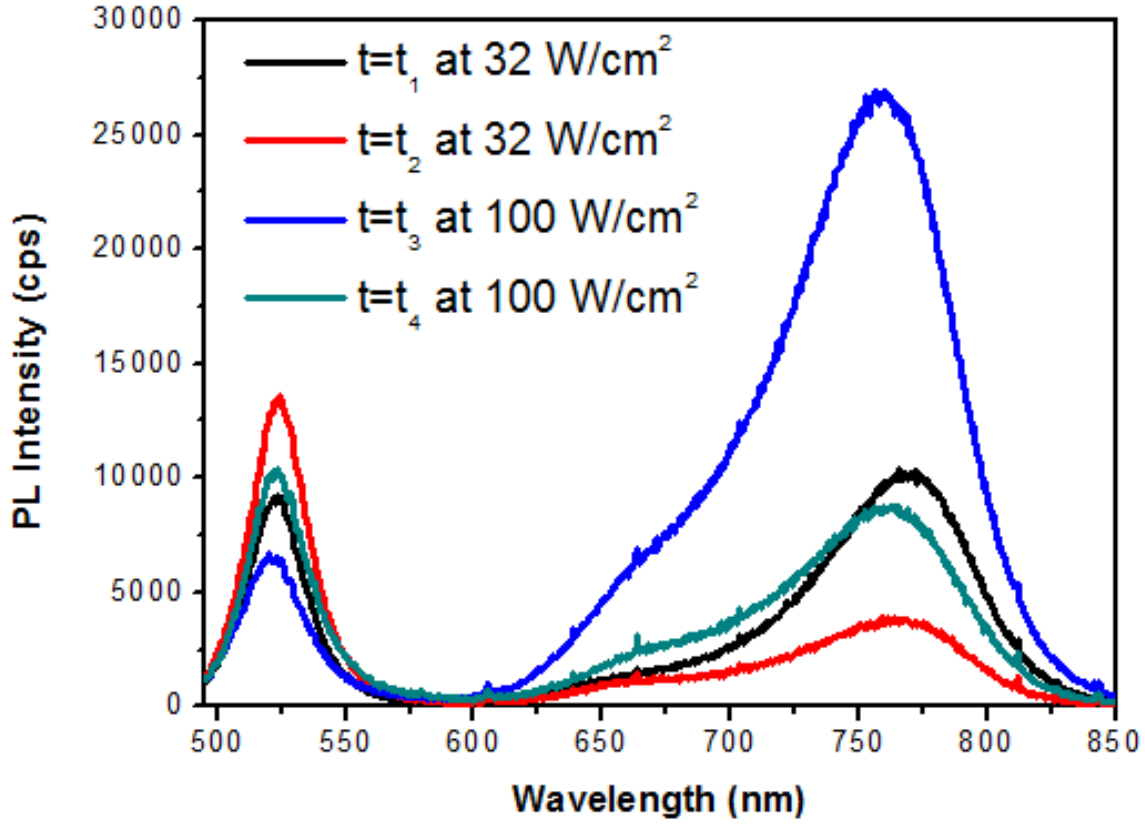

Figure 7.10: PL spectra of a phase-segregated $FA_{0.5}MA_{0.5}Pb(I_{0.5}Br_{0.5})_3$ perovskite film at different photo-irradiation times and different excitation intensities. At the times t_1,t_2 ($t_2 > t_1$) the excitation intensity is 32W/cm^2, while at the time $t_3=t_2+dt$ the excitation intensity is changed to 100W/cm^2, until the time $t_4 > t_3$.

Electron-hole radiative recombination in the Br-rich phase.

Based on the analysis and results, presented in section 7.2 and in the current section, we conclude that the two aforementioned mechanisms (atmospheric effect, decomposition of the I-rich phase) which could lead to PL quenching of the I-rich phase are likely to occur in the $FA_{0.5}MA_{0.5}Pb(I_{0.5}Br_{0.5})_3$ perovskite film, upon light excitation, especially in the high excitation regime, where we have observed (in the previous section) that a double exponential function fits better to the PL experimental data. Notice that, the main difference between the two PL quenching mechanisms is that the increased non-radiative recombination decay due to the photo-induced chemical reactions of the I-rich perovskite phase with air molecules is, with respect to time, reversible under dark conditions, while the expulsion of iodine from the I-rich phase, is an irreversible process. Thus, in the next section, we examine the reversibility issue in order to confirm that the PL quenching of the I-rich phase at least partially originates from iodine expulsion, which may occur due to a remaining solvent on the perovskite surface. A residual solvent on the perovskite surface, reflects the sensitivity of the phenomenon to the material processing and preparation. Particularly, factors such as temperature and time of thermal annealing play a major role, and a further research on this subject is essential in order to avoid the degradation of the perovskite film. Another evidence for iodine expulsion, would be the reduction of the I-rich phase absorption with irradiation time. Consequently, in this section, we observed that pressure variations could induce further phase segregation to the already phase-segregated perovskite film, however,no clear evidence was found to declare that the atmospheric effect has an impact on the PL quenching observed in air, when the perovskite sample was placed in vacuum. To the contrary, ambient air could only enhance the PL. We also clarified the main features of the possible mechanisms, which could provoke the quenching of the photoluminescence, and we deduced that further research on this subject needs to be done in order to answer the question: why do photo-generated charge carriers facilitate radiative recombination in the Br-rich perovskite phase at longer light excitation times, rather than diffuse and finally recombine in the I-rich perovskite phase, which is energetically favored?

7.4 Phase Segregation Recovery Kinetics

In this part, we turn our attention to the phase segregation recovery kinetics in a $FA_{0.5}MA_{0.5}Pb(I_{0.5}Br_{0.5})_3$ thin film. Specifically, we will attempt to evaluate the reverse phase segregation rate, which corresponds to the recovery rate, from the emission spectra. The recovery rate $k_{reverse,em}$ is strongly dependent on the excitation intensity and the exposure to illumination time. Thus, in most experimental studies on the subject, which can be found in the literature, the recovery rate is evaluated at low excitation intensities ($\leq$1 W/cm^2) and at photo-irradiation times ranging from 1min to 30min, and in the majority of cases, the time needed for the phase segregated perovskite to recover to its initial mixed halide phase, in the absence of light, was in the range of 30min to 1-2hours. Instead, we followed a different approach. We wanted to evaluate the phase segregation recovery rate, after the PL emission quenching of the I-rich phase and the rise of the Br-rich phase in emission spectra had taken place. Hence, we used high excitation intensities in order to accelerate the above mechanisms, to occur at short illumination times.

Moving forward, we will briefly describe the process we followed in order to evaluate the recovery rate. Firstly, we irradiated the perovskite film with a (CW) laser at 325nm excitation wavelength with 3.2W/cm^2 excitation intensity for a time interval of 1 second, in order to collect an initial PL measurement, before we used a higher excitation intensity and induced phase segregation. Continuing, we excited the sample with 32W/cm^2 and 160W/cm^2 excitation intensities for 60s and 30s, respectively. Finally, we left the sample in the dark (absence of light) and we periodically measured its (PL) emission spectrum at different times, by using an excitation intensity of 3.2W/cm^2 for 1s (the time needed to acquire PL spectra). This excitation for such short time is incapable of provoking further phase segregation due to the low segregation rate, estimated in section 7.2. The results are shown in Figures 7.11 and 7.12. In general, we observe a tendency toward recovery. Specifically, in Figure 7.11, we observe the partial recovery to the initial mixed perovskite phase at a time of $\approx$ 190min ($\approx$3.2 hours, after closing the light source). The recovery process seems to saturate, since the PL

intensity of the mixed phase remains constant after some time at a lower PL intensity, in comparison to the PL intensity before the halide phase segregation occurred. In the case of 160W/cm^2 excitation intensity (Figure 7.12), we observe a tendency to fully recover to its initial PL spectra before phase segregation occurs. Now, in order to evaluate the recovery rate in each case, we plot the PL intensity of the mixed perovskite phase as a function of time, at an excitation intensity of 3.2W/cm^2. The results are shown in Figures 7.11c and 7.12c. In the case of lower excitation intensity and long irradiation time, we observe a similar kinetic behavior as in the phase segregation effect but at different time scales, and now is the mixed perovskite phase emission, which increases exponentially, while in the phase segregation was the I-rich perovskite phase, which behaved in this way. Furthermore, in Figure 7.11c, we fitted a single exponential in the form of $I(t)=I_1- I_2e^{-k_{reverse,em}t}$ to the experimental data and we evaluated the phase segregation recovery rate as $\mathbf{k_{reverse,em} = (0.52 \pm 0.08)\cdot 10^{-3}\ s^{-1}}$, which is one order of magnitude lower than the typical values, which exist in the literature, at the low excitation intensity regime.

In the second case of higher excitation intensity and shorter irradiation time(Figure 7.12c), interestingly, we observe a linear behavior of the PL intensity with time from 60min to 280min under dark conditions.

Summarizing, we monitored the kinetics of phase segregation recovery in the absence of light for two different excitation intensities and times of irradiation, and we observed the recovery to the initial mixed perovskite phase before phase segregation occurred, but at a slightly shifted (identical) emission wavelength and lower emission PL intensity, in the case of lower (higher) excitation intensity. Specifically, in the first case (I_{exc}=32W/cm^2), we observe recovery to a slightly blue-shifted emission suggesting less I-atoms in the recovered mixed phase and to a significantly lower PL intensity, with a low phase segregation recovery rate, while in the second case (I_{exc}=160W/cm^2) the phase segregated perovskite recovers to its initial emission wavelength of the mixed halide phase and also tends to return to its initial PL intensity in a linear fashion. We estimate that the recovery rates are of the same order of magnitude, and we speculate that the long-term irradiation, might be more harmful for the perovskite sample in terms of recovering, and also that the

recovery of the perovskite is likely to have different dependence on the excitation intensity and the irradiation time. Notice that as the irradiation time increases, more crystallites undergo phase segregation, while as the excitation intensity increases, the density of the phase segregated domains within the film also increases, indicating that both conditions lead to an increased number of phase segregated domains. However, the observed reversibility of the phenomenon, indicates that the free energy of the system in the presence and absence of illumination are different and depend on the illumination time.

Finally, it is worth noting that the observed recovery at a significantly lower PL intensity (20% of initial intensity), compared to its initial, and in a slightly shifted emission wavelength (Figure 7.11), are evidences for iodine expulsion during the phase segregation process at long irradiation times, which could easily occur if there is residual solvent on the surface of perovskite thin film. I also observed that positions in the film, which were excited with high excitation intensity for a long irradiation time, could not recover even after days in the absence of light. Therefore, an amount of solvent on the perovskite surface is the most prominent cause, which can explain the observed PL quenching of the I-rich perovskite phase and the rise of Br-rich phase emission, as well as the observed partial recovery of the phase segregated perovskite to its initial mixed halide phase. Hence, the PL quenching effect of the I-rich perovskite phase can considerably affect the recovery of the phase-segregated film. For a future work, it would be useful and meaningful to examine, if the recovery rate remains constant, for constant $I_{exc} \cdot t_{irrad}$ products with different I_{exc}, t_{irrad} values as initial conditions.

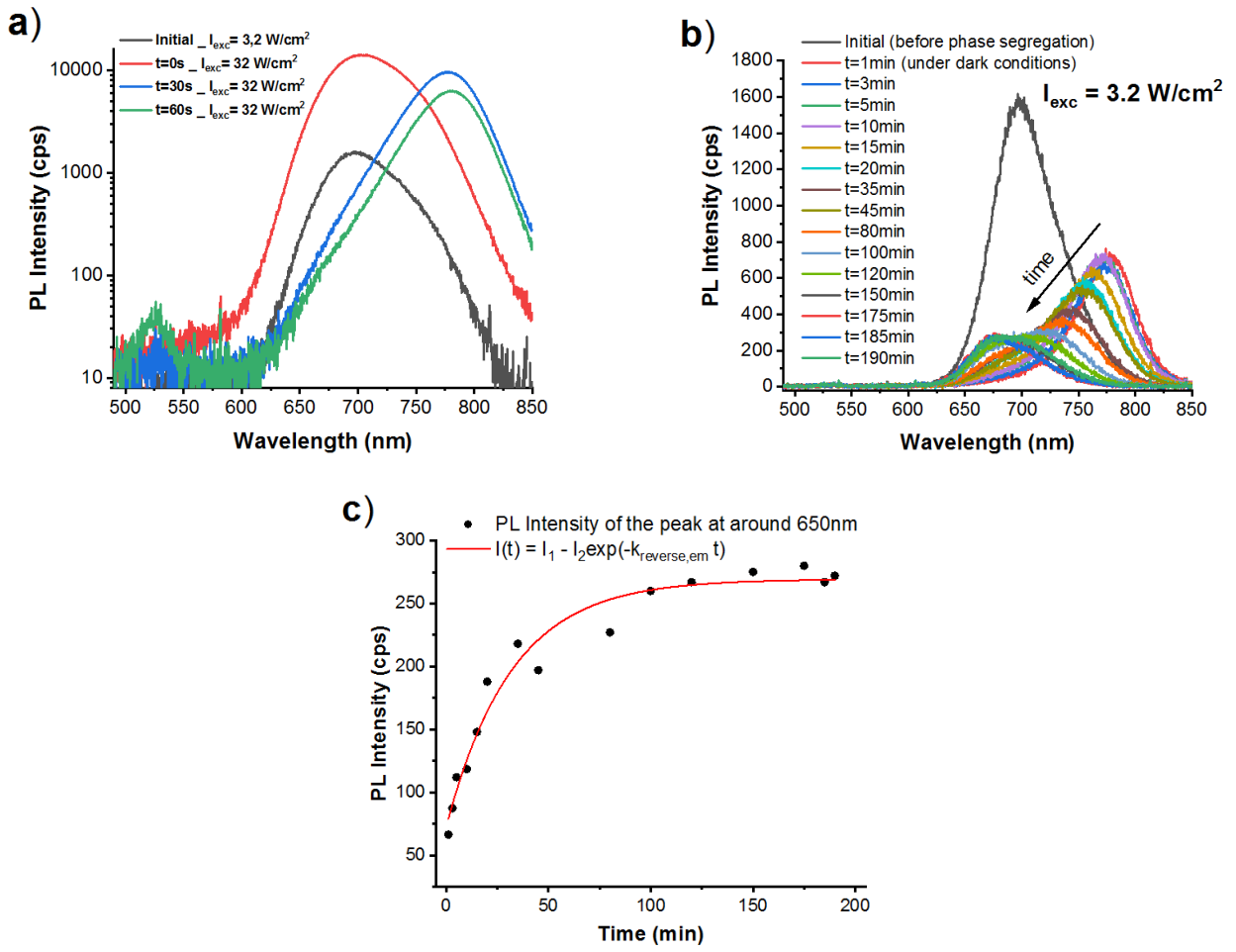

Figure 7.11: a) Photoluminescence (PL) spectra of $FA_{0.5}MA_{0.5}Pb(I_{0.5}Br_{0.5})_3$ thin film excited at I_{exc}=3.2W/cm^2 (initial) before phase segregation occurred, and at I_{exc}=32W/cm^2 at different times during phase segregation. b) PL spectra of $FA_{0.5}MA_{0.5}Pb(I_{0.5}Br_{0.5})_3$ thin film at I_{exc}=3.2W/cm^2 and at different times in the dark (absence of light). c) PL intensity of the peak which corresponds to the mixed halide phase, as a function of the time the sample was left in the dark. Black dots correspond to the experimental data, while the red line corresponds to the exponential fitting of the experimental PL data.

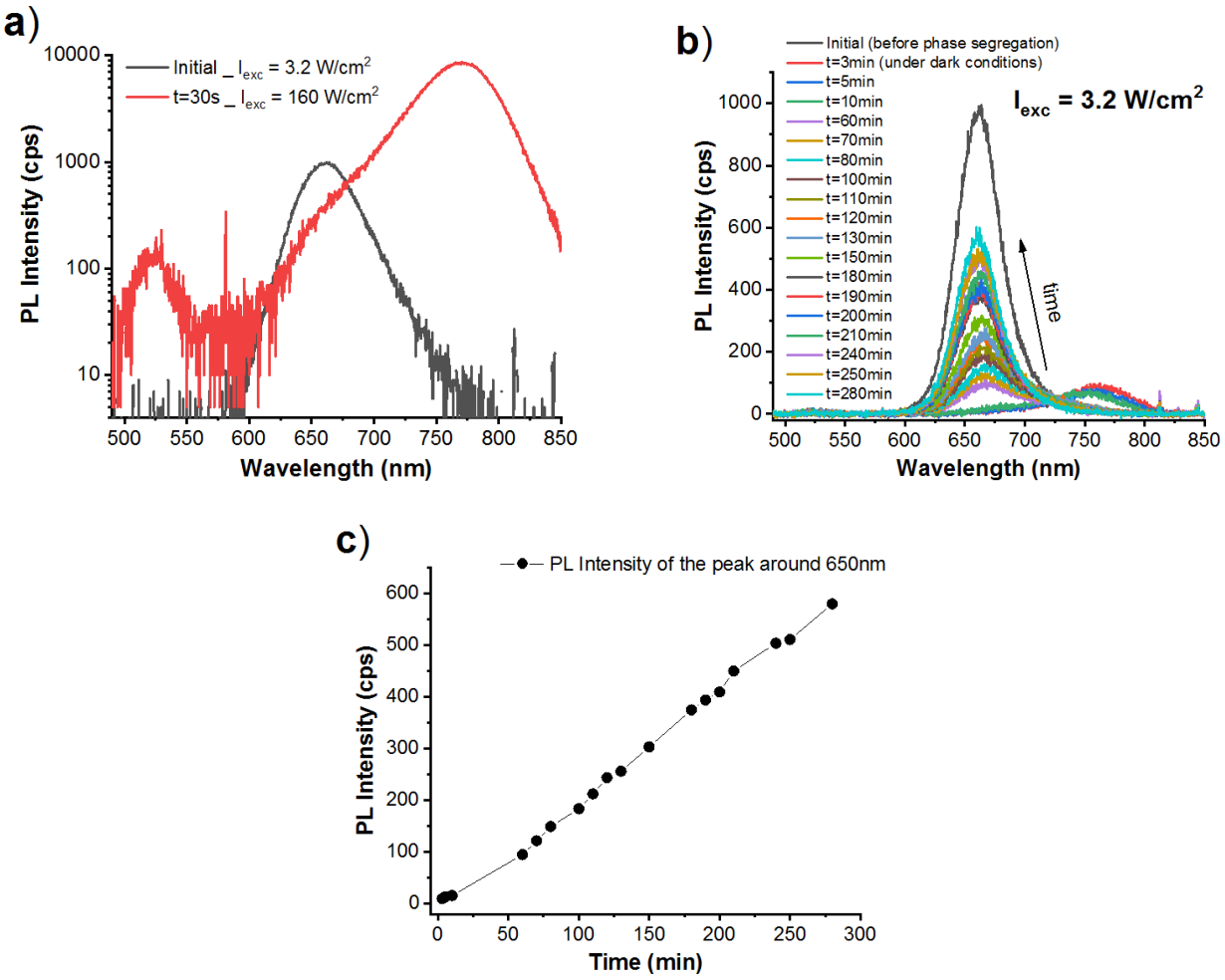

Figure 7.12: a) Photoluminescence (PL) spectra of $FA_{0.5}MA_{0.5}Pb(I_{0.5}Br_{0.5})_3$ thin film excited at I_{exc}=3.2W/cm^2 (initial) before light-induced phase segregation, and at I_{exc}=160W/cm^2 following phase segregation. b) Recovery PL spectra of $FA_{0.5}MA_{0.5}Pb(I_{0.5}Br_{0.5})_3$ thin film at I_{exc}=3.2W/cm^2 and at different times in the dark. c) PL intensity of the peak at 650nm, which corresponds to the mixed halide phase, as a function of the time the sample was left in the dark.

7.5 Spectral Changes in Reflection

In the current experiment, we expose the $FA_{0.5}MA_{0.5}Pb(I_{0.5}Br_{0.5})_3$ perovskite thin film under 325nm (CW) laser excitation for a certain time in order to induce halide phase segregation, while at the same time we monitor the changes in the reflection spectra. A description of the experimental setup follows. A Halogen lamp emits white light through a fiber to the sample, while at the same time a (CW) laser with 325nm excitation wavelength excites the sample. A monochromator, which is connected with a CCD camera detects and analyzes the reflection light from the sample, after passing through a converging lens and a slit with 50μm width and 50μm height, in order to maximize the ratio of the incoming signal from the phase-segregated region to the total incoming signal, which corresponds to the total exposed area. The reflectance is calibrated by using a 99% reflecting mirror. When we measure the reflection from the sample following different exposure times to (CW) laser irradiation, we turn off the (CW) laser to ensure that the detected signal exclusively corresponds to the sample's reflection. At last, the laser spot size on the sample is roughly 100μm, while the white light spot size is around 2mm. The sample's PL and reflection are collected by a lens and focused to a diameter of roughly 80μm and 1.6mm, respectively. Since the final spot diameter from the phase-segregated area is larger than the corresponding width of the entrance slit, we can detect the signal from the phase-segregated area exclusively and minimize the incoming signal from the surrounding exposed area. Finally, for the first measurement at (t=0), we measure the reflection of the sample before the operation of the (CW) laser. The results are shown in Figure 7.13.

Interestingly, when the sample was exposed for 120 seconds upon (CW) laser excitation with $3.2 W/cm^2$ excitation intensity, negligible changes in the reflection spectra were observed, as shown in Figure 7.13(a,c), while for the same excitation intensity and exposure to irradiation time, the changes in the PL spectra were significant and decisive. This can be attributed to the relatively slow rate of change of the absorption (and hence the reflection) spectra, compared to the rate of change of the PL spectra, as mentioned in the the-

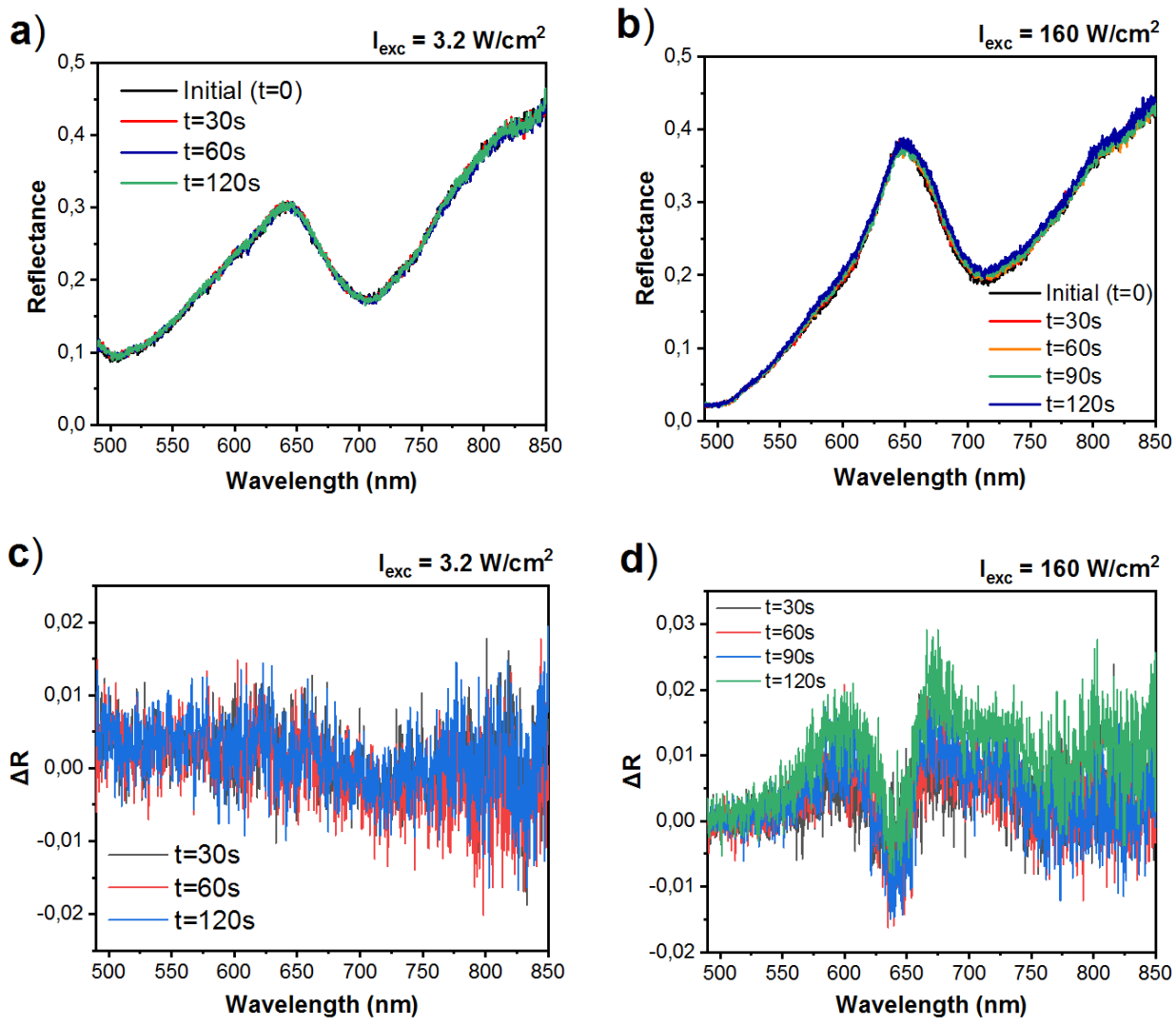

Figure 7.13: **(a,b):** Reflection spectra of $FA_{0.5}MA_{0.5}Pb(I_{0.5}Br_{0.5})_3$ perovskite thin film at different laser irradiation times. The phase segregation is induced by exciting the sample with a 325nm (CW) laser at a) I_{exc}=3.2W/cm^2 and b) I_{exc}=160W/cm^2, while the reflection spectra are acquired periodically with the laser turned off. The black line (initial t=0) corresponds to the initial reflection spectrum, before phase segregation occurs. **(c,d):** variations in the reflection spectra $\Delta R = R(t) - R(t=0)$ at different laser irradiation times, at c) I_{exc}=3.2W/cm^2 and d) I_{exc}=160W/cm^2.

oretical background. On the other hand, in Figure 7.13(b,d), at 160W/cm^2 excitation intensity, the changes in the reflection spectra with respect to time of laser irradiation, are noticeable. Specifically, Figure 7.13(c,d) shows the reflection changes $\Delta R = R(t) - R(t=0)$, at different times of irradiation with a

(CW) laser, which induces halide phase segregation in the sample. In Figure 7.13d, we observe the reduced reflection at approximately 650nm, which corresponds to the mixed halide perovskite phase of the $FA_{0.5}MA_{0.5}Pb(I_{0.5}Br_{0.5})_3$ film, while at the same time we observe the increased reflection at approximately 580nm and 730nm, which correspond to the formation of Br-rich and I-rich phases within the film, respectively. The observed changes are in the order of 1 to 2% in agreement with previous experimental works on the subject, which are mentioned in the theoretical part.

Lastly, we notice that the PL quenching effect, which is prominent in the PL spectra at the time scales used in this experiment, is not observed in the reflection spectra at the irradiation time of ≈120sec. This effect should reduce the absorption (and thus the reflection) of the I-rich perovskite phase with time due to the iodine expulsion. We claim that the PL quenching of the I-rich phase takes more time to be observed in the reflection spectra due to the lower rate of change of the reflection spectra with time, compared to the rate of change of the corresponding PL spectra. In fact, it needs hours of laser irradiation in order to observe a reduction in the absorption of the I-rich phase, as shown in [84].

In conclusion, we conducted reflection measurements with time in order to monitor the changes in the reflection spectra due to the halide phase segregation effect, and we confirmed that the phase segregation indeed induces spectral changes in the reflection, changes which are small in absolute magnitude (approximately 1 to 2%), and smooth with time, in comparison to the dramatic changes in the PL spectra, and which apparently lead to lower phase segregation rates, compared to the corresponding rates that were extracted from the emission spectra. We speculate that such small changes in reflection spectra combined with the noisy signal (large fluctuations) observed in Figure 7.13(c,d) may be due to insufficient signal detection from the phase-segregated region, meaning that the detected signal comes mainly from the exposed area around the phase-segregated region. Since only a small portion of the detected signal corresponds to the phase-segregated region, the experiment may not be conclusive.

7.6 Charge Carrier Recombination Dynamics

In this part, we conducted time-resolved photoluminescence measurements in order to study the carrier dynamics in the $FA_{0.5}MA_{0.5}Pb(I_{0.5}Br_{0.5})_3$ perovskite thin film, during halide phase segregation. The instruments used in this experiment are mentioned in the experimental methods. We excite the $FA_{0.5}MA_{0.5}Pb(I_{0.5}Br_{0.5})_3$ perovskite film with a pulsed laser at 410nm excitation wavelength and 49W/cm^2 excitation intensity for approximately 15 minutes. The laser spot on the film has a diameter of 2μm. After 15 minutes of irradiation at 49W/cm^2, we conduct PL spectroscopy measurements and time-resolved PL measurements on the phase segregated perovskite thin film at various excitation intensities. Figure 7.14(a,b) shows the PL intensity of each perovskite phase (Br-rich, mixed and I-rich phases) at various light excitation intensities. The Br-rich pervoskite phase corresponds to the PL peak at 535nm, while the I-rich phase corresponds to the PL peak at 780nm.

Moving forward, we have to notice that in such complex materials, it remains challenging to clarify all the physical mechanisms, which are involved and dictate any of the decay time components of a PL peak. This is definitely not trivial. However, by exploiting the results from previous works in other perovskite materials and the qualitative analysis, which was made in section 4.1, we managed to empirically identify the physical mechanisms behind the observed fast and slow decay time components of each PL peak. As we mentioned in section 4.1, at low excitation intensities the first-order (monomolecular) recombination process is dominant, which in these perovskite materials mainly consists of a non-radiative recombination via recombination centers (SRH traps). The first order monomolecular recombination is expected to be constant with variations in excitation intensity. On the contrary, the second order bimolecular recombination is carrier density-dependent and hence, depends on the excitation intensity, as mentioned in the theoretical background. Figure 7.14(c,d) shows the time-resolved photoluminescence of the PL peaks at 535nm and 780nm, which correspond to the Br-rich and I-rich phases, respectively, at different excitation intensities. Furthermore, Figure 7.14(e,f) depicts the decay times of each PL peak as a function of excitation

intensity. The decay times were extracted by the corresponding exponential fits to the data, as shown in Figure 7.15. The time-resolved PL curves of the Br-rich phase could be fitted by two exponentials, while the corresponding curves of the I-rich phase could be fitted by a mono-exponential function. In addition, we observe that the slow decay component τ_2 of the Br-rich phase and the decay time of the I-rich phase are fluence-dependent and as such, we attribute them to band-to-band radiative charge carrier recombination. The fast decay component τ_1 of the PL peak that corresponds to the Br-rich phase, on the other hand, only slightly changes (a few picoseconds) with variations in excitation intensity, so we speculate that it originates from some carrier diffusion process out of the Br-rich phase region. Moreover, the rising delay of the peak, which corresponds to the I-rich phase, in Figure 7.14d), indicates carrier injection from the Br-rich and mixed-halide phases to the I-rich phase. The maximum of the TRPL intensity (I-rich phase) occurs at different times after excitation, depending on the excitation intensity. With increasing excitation intensity, the fast decay component τ_1 varies from 0.82ns to 0.63ns, while the slow decay component varies from 7.6ns to 3.4ns, in the Br-rich phase. In the I-rich phase, instead, the decay time varies from 8.7ns to 2.1ns with increasing excitation intensity. Finally, in Figure 7.15(f,g), for the I-rich phase, we notice that for excitation intensities higher than 24 W/cm^2, the mono-exponential decay fit to the data becomes insufficient, and a multi-exponential decay curve is in fact needed in order to obtain the PL decay time.

Summarizing the above analysis, we conducted time-resolved PL measurements in order to investigate the charge carrier recombination dynamics in both Br-rich and I-rich inclusions within the perovskite film, and we deduced that the dominant charge carrier recombination process is the bimolecular (band-to-band) radiative recombination. However, in order to study deeply the recombination dynamics, we need to further investigate the decay times of the PL peaks, which correspond to the Br-rich and I-rich inclusions, versus temperature and at different irradiation times.

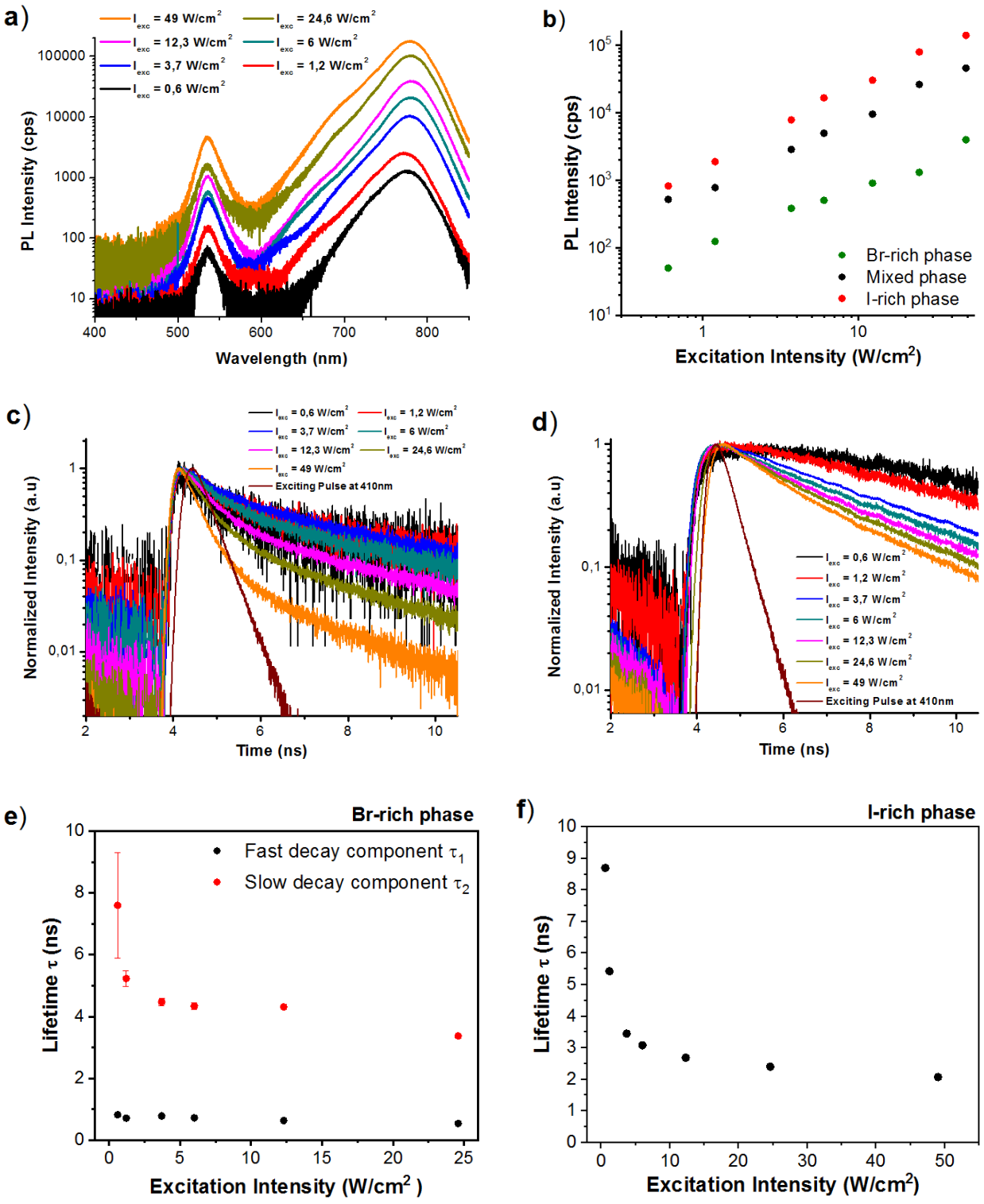

Figure 7.14: a) PL spectra of a phase-segregated $FA_{0.5}MA_{0.5}Pb(I_{0.5}Br_{0.5})_3$ perovskite film, excited with a 410nm pulsed laser at different light excitation intensities. b) PL intensity of the peaks, which correspond to the Br-rich, mixed and I-rich phases at various excitation intensities. (c,d): Time-resolved photoluminescence decay curves of c) the Br-rich phase and d) the I-rich phase, at different light excitation intensities. (e,f): Fast and slow-component decay times of the PL peaks, which correspond to the Br-rich and I-rich phases, as a function of excitation intensity. The fast decay component corresponds to the charge carrier diffusion, while the slow decay component corresponds to the radiative recombination.

a)

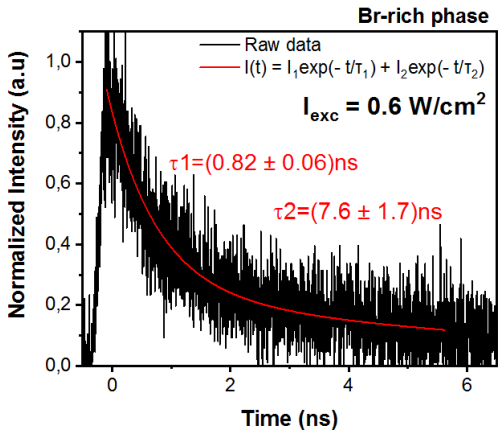
Br-rich phase
Raw data
I(t) = I1exp(- t/τ1) + I2exp(- t/τ2)
Iexc = 0.6 W/cm2
τ1=(0.82 ± 0.06)ns
τ2=(7.6 ± 1.7)ns
Normalized Intensity (a.u)
Time (ns)

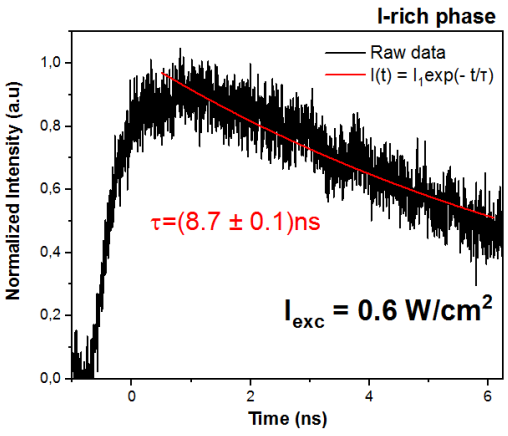
I-rich phase
Raw data
I(t) = I1exp(- t/τ)
τ=(8.7 ± 0.1)ns
Iexc = 0.6 W/cm2
Normalized Intensity (a.u)
Time (ns)

b)

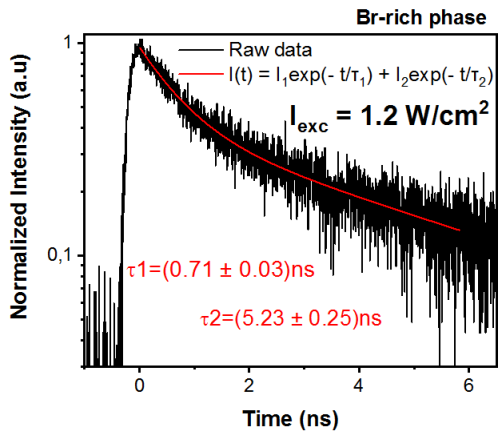
Br-rich phase
Raw data
I(t) = I1exp(- t/τ1) + I2exp(- t/τ2)
Iexc = 1.2 W/cm2
τ1=(0.71 ± 0.03)ns
τ2=(5.23 ± 0.25)ns
Normalized Intensity (a.u)
Time (ns)

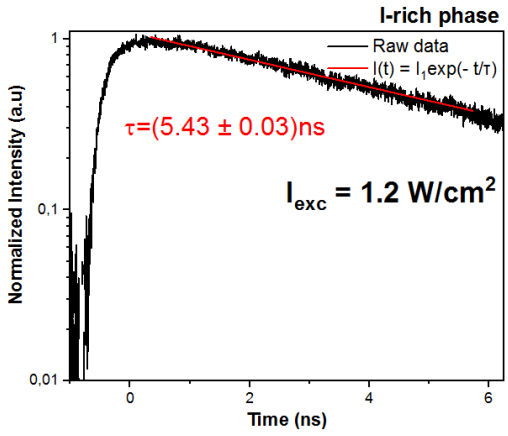
I-rich phase
Raw data
I(t) = I1exp(- t/τ)
τ=(5.43 ± 0.03)ns
Iexc = 1.2 W/cm2
Normalized Intensity (a.u)
Time (ns)

c)

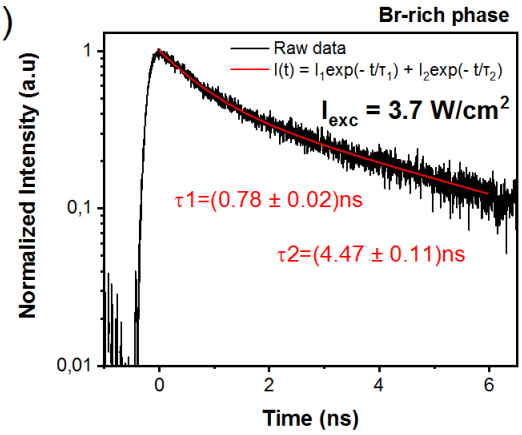
Br-rich phase
Raw data
I(t) = I1exp(- t/τ1) + I2exp(- t/τ2)
Iexc = 3.7 W/cm2
τ1=(0.78 ± 0.02)ns
τ2=(4.47 ± 0.11)ns
Normalized Intensity (a.u)
Time (ns)

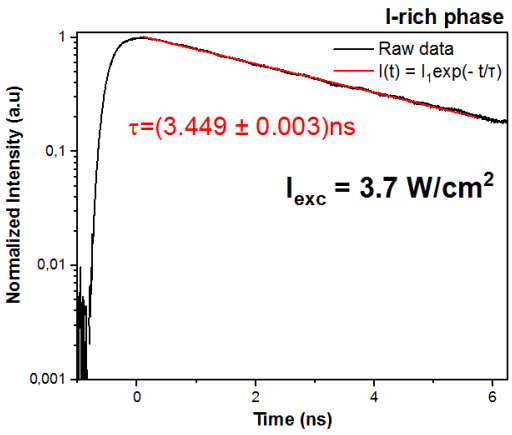
I-rich phase
Raw data
I(t) = I1exp(- t/τ)
τ=(3.449 ± 0.003)ns
Iexc = 3.7 W/cm2
Normalized Intensity (a.u)
Time (ns)

d)

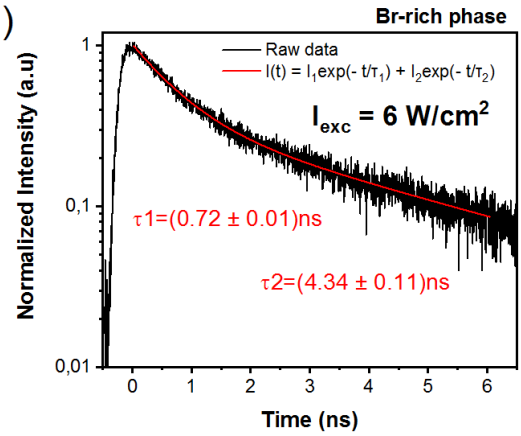
Br-rich phase
Raw data
I(t) = I1exp(- t/τ1) + I2exp(- t/τ2)
Iexc = 6 W/cm2
τ1=(0.72 ± 0.01)ns
τ2=(4.34 ± 0.11)ns
Normalized Intensity (a.u)
Time (ns)

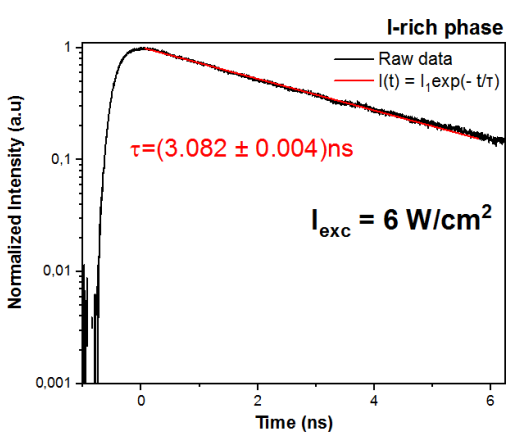
I-rich phase
Raw data
I(t) = I1exp(- t/τ)
τ=(3.082 ± 0.004)ns
Iexc = 6 W/cm2
Normalized Intensity (a.u)
Time (ns)

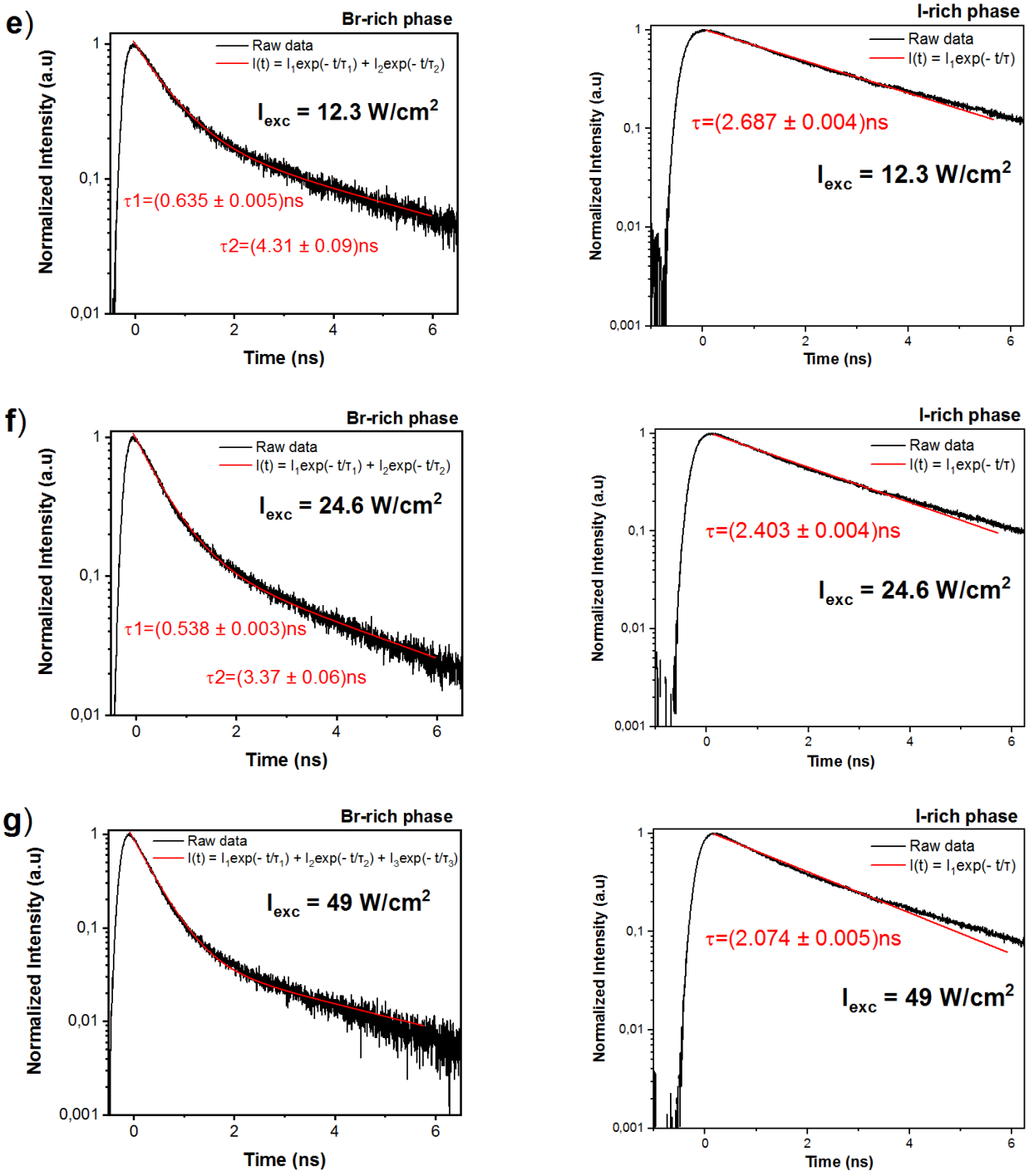

Figure 7.15: Experimental PL data of the Br-rich and I-rich phases accompanied by exponential fitting, for a) 0.6W/cm^2, b) 1.2W/cm^2, c) 3.7W/cm^2, d) 6W/cm^2, e) 12.3W/cm^2, f) 24.6W/cm^2, g) 49W/cm^2 excitation intensities, respectively.

7.7 Photoluminescence (PL) Imaging

In the final part of this work, we present photoluminescence images of the phase-segregated $FA_{0.5}MA_{0.5}Pb(I_{0.5}Br_{0.5})_3$ perovskite thin film. We illuminate a random area on the perovskite sample (the spot diameter is 90μm) using a 385nm UV Lamp with excitation intensity of I_{exc}= 40W/cm^2, for a certain time, in order to induce halide phase segregation. The UV Lamp is coupled with a PL camera, which is used to acquire images of the sample's luminescent emission. Afterwards, we periodically acquire PL spectra and PL images, during the phase segregation process. Additionally, we use a shortpass filter with cut-off at 532nm and a longpass filter with cut-off at 600nm in order to acquire PL images from the Br-rich phase emission and from the mixed, I-rich phase emission, respectively. Then, we use the ImageJ application in order to overlap the two distinct, spectrally separated PL images into a single PL image. The results are shown in Figures 7.16 and 7.17. Figure 7.16 depicts the procedure that was followed in order to extract a single PL image. In Figures 7.17a and 7.17e, we observe the PL quenching of the red (mixed halide phase, I-rich phase) emission. Interestingly, in Figures (b,d) and (f,h), we observe that with increasing irradiation time ($t_2 > t_1$), the emission of the Br-rich perovskite phase originates from smaller and smaller individual bright spots within the film, indicating that the temporary PL peak originates from small nano-domains. Finally, we observe that at long irradiation times, using high excitation intensity, there is only one perovskite phase within the film, emitting light, due to the PL quenching of the perovskite phases with a lower energy band gap, compared to the energy band gap of the Br-rich phase.

In conclusion, the results of the current experiment reveal that the green spots, which correspond to the Br-rich perovskite phase, are more localized than the red spots, which correspond to the I-rich phase, suggesting that Br-rich spots have a tendency to localize whereas the I-rich areas are widespread on the surface of the sample.

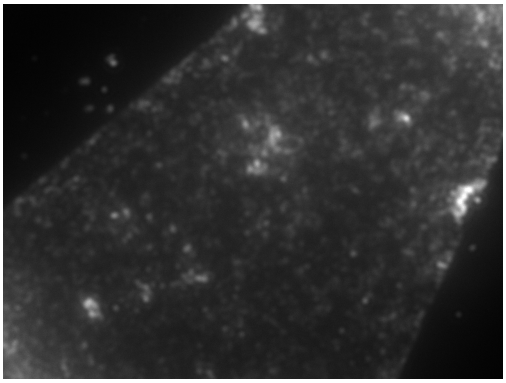

(a) Emission in red

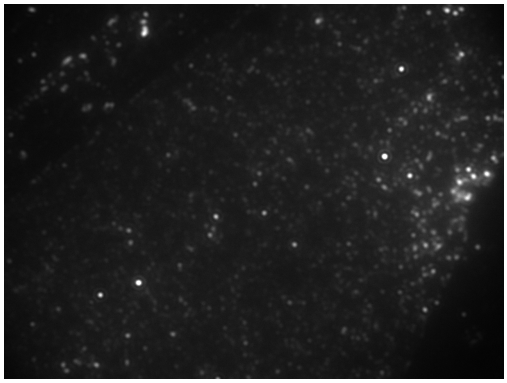

(b) Emission in green

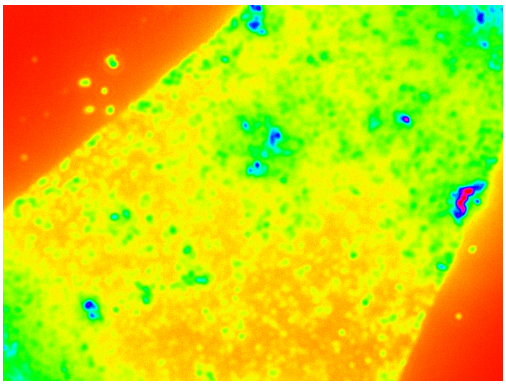

(c) Emission in red

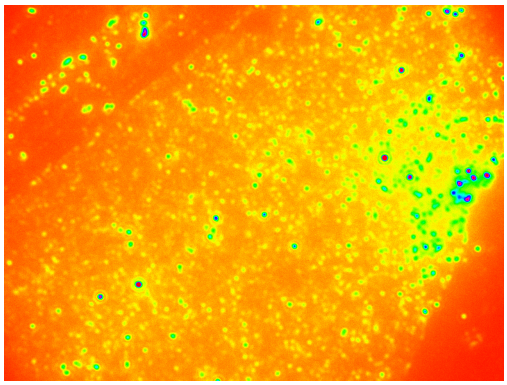

(d) Emission in green

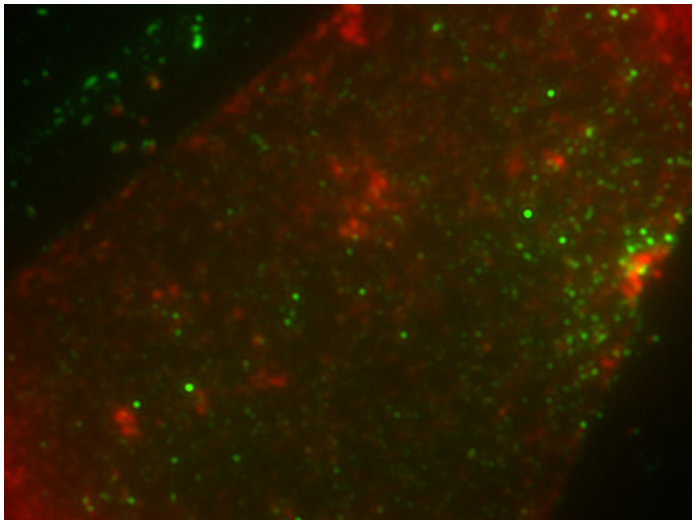

(e)

Figure 7.16: PL image of the phase-segregated perovskite film, excited with a 385nm UV Lamp with I_{exc} = 40W/cm^2. a) PL image using a longpass filter (cut-off at 600nm) which depicts the sample's emission in red. b) PL image using a shortpass filter (cut-off at 532nm) which depicts the sample's emission in green. (c,d): Spectrally-resolved PL images with the intensity scale bar ranging from zero (red) to one (purple). e) Combination of the PL images in a) and b), using the ImageJ application. The images depict the 90x90µm^2 exposed area. The green spots are roughly 2µm.

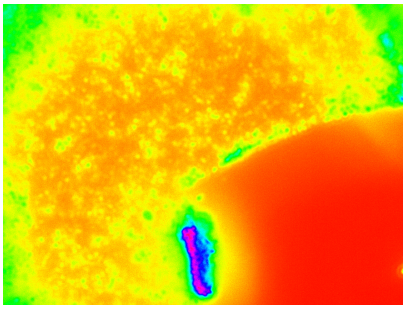

(a) Emission in red at t=t_1

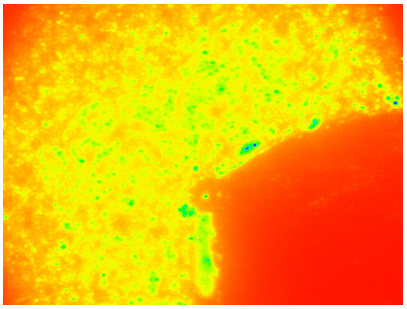

(b) Emission in green at t=t_1

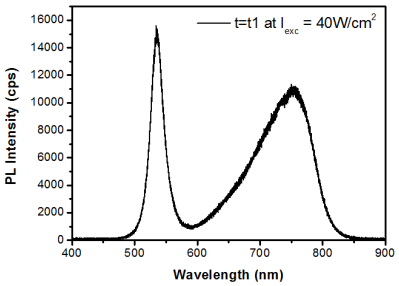

(c) t=t_1

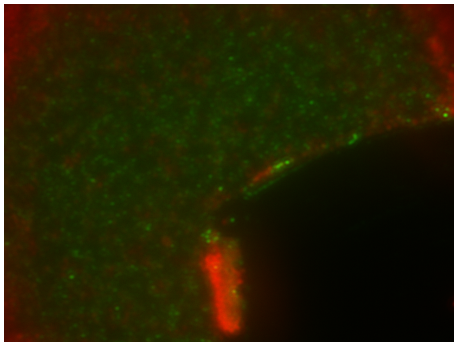

(d) t=t_1

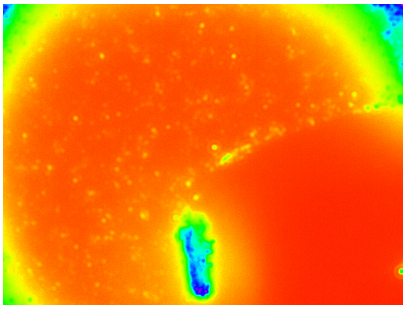

(e) Emission in red at t=t_2

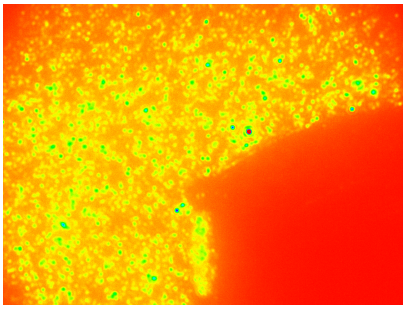

(f) Emission in green at t=t_2

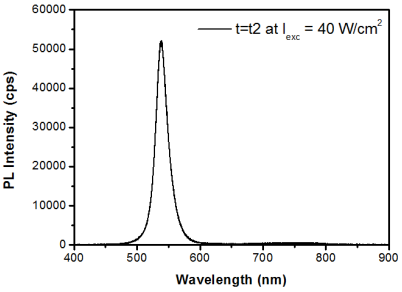

(g) t=t_2

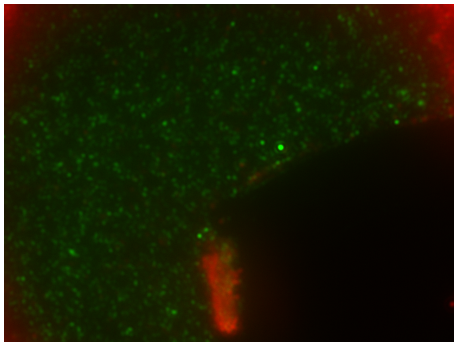

(h) t=t_2

Figure 7.17: (a-b,e-f): Spectrally-resolved PL images with the intensity scale bar ranging from zero (red) to one (purple) at exposure time: (a,b) t=t_1 and (e,f) t=t_2. c) PL emission spectrum at t=t_1. PL image containing red and green spectral components: d) at t=t_1, h) at t=t_2, with $t_2 > t_1$. g) PL emission spectrum at t=t_2. The images depict a 90x90µm^2 area.

Chapter 8

Conclusions and Future Work

Concluding this research, we investigated the light-induced phase segregation in a $FA_{0.5}MA_{0.5}Pb(I_{0.5}Br_{0.5})_3$ perovskite thin film by monitoring spectral changes in emission and absorption. The emission dynamics of the mixed-halide perovskite at various excitation levels showed that partial substitution of methylammonium (MA^+) with formamidinium (FA^+) suppresses the phase segregation by more than one order of magnitude, and also revealed the existence of a mechanism that quenches the PL of the iodide-rich phase with illumination time, and this is accompanied by an increase in the emission of the bromide-rich phase. Furthermore, we investigated the emission behavior of the phase-segregated perovskite at room temperature in vacuum, where an initial PL enhancement of the I-rich phase was observed. Moreover, we managed to monitor the phase segregation recovery kinetics of the mixed-halide perovskite, which was phase-segregated with relatively high excitation intensity for a certain irradiation time, until the emission of the Br-rich and I-rich phases was prominent in the PL spectra, and it was observed that strong excitation intensities for long irradiation times (strong PL quenching of the I-rich phase) could affect the reversibility of phase segregation, which is evidence for iodine expulsion or loss of iodine in the phase-segregated region of the thin film. Additionally, we investigated the charge carrier recombination dynamics of the phase-segregated $FA_{0.5}MA_{0.5}Pb(I_{0.5}Br_{0.5})_3$ perovskite, and it was found that band-to-band radiative recombination is the dominant charge carrier recombination process in these inclusions, but further research on this subject is needed in order to obtain more insights. Finally, we obtained PL images of the phase-segregated region of the perovskite thin film using a PL camera to track the spatial distribution of the corresponding PL

spectra of the sample with irradiation time, and it was observed that with increasing irradiation time, the emission of the Br-rich phase was originating from smaller and brighter localized green spots whereas the emission of the I-rich (and mixed) phase was originating from more extensive areas on the surface of the sample.

For future work, the emission dynamics of the $FA_{0.5}MA_{0.5}Pb(I_{0.5}Br_{0.5})_3$ perovskite at the low excitation intensity regime should be investigated in order to determine the power threshold for PL quenching. Moreover, it is essential to monitor the changes in absorption spectra at different irradiation times, in order to get more insights about the changes in emission spectra and the PL quenching effect. Also important is examining if the PL quenching of the I-rich phase in ambient air originates from light-induced chemical reactions between the I-rich perovskite phase and molecules that are present in the atmosphere. A proposed experiment is to add polymethyl methacrylate (PMMA) on top of the film in order to exclude the atmospheric effect and study the emission behavior or even the absorption spectra over time. Furthermore, evaluating the phase segregation rates as well as the phase segregation recovery rates under constant $I_{exc} \cdot t_{irrad}$ products would provide us more information on how exactly these parameters affect the aforementioned rates and if they both have the same dependence on the excitation intensity and irradiation time. At last, the temperature-dependence of the PL spectra of the phase-segregated mixed-halide perovskites, as well as the time-decays of each PL peak, which correspond to the Br-rich and I-rich phases, versus temperature and irradiation time, would provide us additional insights about the charge carrier recombination dynamics of this system, which is consisted of three different perovskite phases, and could shed light on the clarification of the PL quenching mechanism, which quenches the emission of the I-rich phase.

Bibliography

[1] Akihiro Kojima, Kenjiro Teshima, Yasuo Shirai, and Tsutomu Miyasaka. Organometal halide perovskites as visible-light sensitizers for photovoltaic cells. *Journal of the american chemical society*, 131(17):6050–6051, 2009.

[2] Samuel D Stranks, Giles E Eperon, Giulia Grancini, Christopher Menelaou, Marcelo JP Alcocer, Tomas Leijtens, Laura M Herz, Annamaria Petrozza, and Henry J Snaith. Electron-hole diffusion lengths exceeding 1 micrometer in an organometal trihalide perovskite absorber. *Science*, 342(6156):341–344, 2013.

[3] Dane W DeQuilettes, Susanne Koch, Sven Burke, Rajan K Paranji, Alfred J Shropshire, Mark E Ziffer, and David S Ginger. Photoluminescence lifetimes exceeding 8 μs and quantum yields exceeding 30% in hybrid perovskite thin films by ligand passivation. *ACS Energy Letters*, 1(2):438–444, 2016.

[4] K Xerxes Steirer, Philip Schulz, Glenn Teeter, Vladan Stevanovic, Mengjin Yang, Kai Zhu, and Joseph J Berry. Defect tolerance in methylammonium lead triiodide perovskite. *ACS Energy Letters*, 1(2):360–366, 2016.

[5] David P McMeekin, Golnaz Sadoughi, Waqaas Rehman, Giles E Eperon, Michael Saliba, Maximilian T Hörantner, Amir Haghighirad, Nobuya Sakai, Lars Korte, Bernd Rech, et al. A mixed-cation lead mixed-halide perovskite absorber for tandem solar cells. *Science*, 351(6269):151–155, 2016.

[6] Rachel E Beal, Daniel J Slotcavage, Tomas Leijtens, Andrea R Bowring, Rebecca A Belisle, William H Nguyen, George F Burkhard, Eric T Hoke, and Michael D McGehee. Cesium lead halide perovskites with improved

stability for tandem solar cells. *The journal of physical chemistry letters*, 7(5):746–751, 2016.

[7] Bryan A Rosales, Michael P Hanrahan, Brett W Boote, Aaron J Rossini, Emily A Smith, and Javier Vela. Lead halide perovskites: Challenges and opportunities in advanced synthesis and spectroscopy. *ACS Energy Letters*, 2(4):906–914, 2017.

[8] Peng Qin, Soichiro Tanaka, Seigo Ito, Nicolas Tetreault, Kyohei Manabe, Hitoshi Nishino, Mohammad Khaja Nazeeruddin, and Michael Grätzel. Inorganic hole conductor-based lead halide perovskite solar cells with 12.4% conversion efficiency. *Nature communications*, 5(1):1–6, 2014.

[9] Prashant V Kamat. Hybrid perovskites for multijunction tandem solar cells and solar fuels. a virtual issue. *ACS Energy Letters*, 3(1):28–29, 2017.

[10] Joseph S Manser, Makhsud I Saidaminov, Jeffrey A Christians, Osman M Bakr, and Prashant V Kamat. Making and breaking of lead halide perovskites. *Accounts of chemical research*, 49(2):330–338, 2016.

[11] Ian L Braly, Ryan J Stoddard, Adharsh Rajagopal, Alexander R Uhl, John K Katahara, Alex K-Y Jen, and Hugh W Hillhouse. Current-induced phase segregation in mixed halide hybrid perovskites and its impact on two-terminal tandem solar cell design. *ACS Energy Letters*, 2(8):1841–1847, 2017.

[12] Wolfgang Tress, Juan Pablo Correa Baena, Michael Saliba, Antonio Abate, and Michael Graetzel. Inverted current–voltage hysteresis in mixed perovskite solar cells: polarization, energy barriers, and defect recombination. *Advanced Energy Materials*, 6(19):1600396, 2016.

[13] Christopher Eames, Jarvist M Frost, Piers RF Barnes, Brian C O'regan, Aron Walsh, and M Saiful Islam. Ionic transport in hybrid lead iodide perovskite solar cells. *Nature communications*, 6(1):1–8, 2015.

[14] Yuchuan Shao, Yanjun Fang, Tao Li, Qi Wang, Qingfeng Dong, Yehao Deng, Yongbo Yuan, Haotong Wei, Meiyu Wang, Alexei Gruverman, et al. Grain boundary dominated ion migration in polycrystalline

organic–inorganic halide perovskite films. *Energy & Environmental Science*, 9(5):1752–1759, 2016.

[15] Wolfgang Tress, Nevena Marinova, Thomas Moehl, Shaik Mohammad Zakeeruddin, Mohammad Khaja Nazeeruddin, and Michael Grätzel. Understanding the rate-dependent j–v hysteresis, slow time component, and aging in ch 3 nh 3 pbi 3 perovskite solar cells: the role of a compensated electric field. *Energy & Environmental Science*, 8(3):995–1004, 2015.

[16] Federico Brivio, Clovis Caetano, and Aron Walsh. Thermodynamic origin of photoinstability in the ch3nh3pb (i1–x br x) 3 hybrid halide perovskite alloy. *The journal of physical chemistry letters*, 7(6):1083–1087, 2016.

[17] Eric T Hoke, Daniel J Slotcavage, Emma R Dohner, Andrea R Bowring, Hemamala I Karunadasa, and Michael D McGehee. Reversible photo-induced trap formation in mixed-halide hybrid perovskites for photovoltaics. *Chemical Science*, 6(1):613–617, 2015.

[18] Xiao Yang, Xiaoliang Yan, Wei Wang, Xiangxiang Zhu, Heng Li, Wanli Ma, and ChuanXiang Sheng. Light induced metastable modification of optical properties in ch3nh3pbi3- xbrx perovskite films: Two-step mechanism. *Organic Electronics*, 34:79–83, 2016.

[19] Seog Joon Yoon, Sergiu Draguta, Joseph S Manser, Onise Sharia, William F Schneider, Masaru Kuno, and Prashant V Kamat. Tracking iodide and bromide ion segregation in mixed halide lead perovskites during photoirradiation. *ACS Energy Letters*, 1(1):290–296, 2016.

[20] Connor G Bischak, Craig L Hetherington, Hao Wu, Shaul Aloni, D Frank Ogletree, David T Limmer, and Naomi S Ginsberg. Origin of reversible photoinduced phase separation in hybrid perovskites. *Nano letters*, 17(2):1028–1033, 2017.

[21] Daniel J Slotcavage, Hemamala I Karunadasa, and Michael D McGehee. Light-induced phase segregation in halide-perovskite absorbers. *ACS Energy Letters*, 1(6):1199–1205, 2016.

[22] Sergiu Draguta, Onise Sharia, Seog Joon Yoon, Michael C Brennan, Yurii V Morozov, Joseph S Manser, Prashant V Kamat, William F

Schneider, and Masaru Kuno. Rationalizing the light-induced phase separation of mixed halide organic–inorganic perovskites. *Nature communications*, 8(1):1–8, 2017.

[23] Xi Wang, Yichuan Ling, Xiujun Lian, Yan Xin, Kamal B Dhungana, Fernando Perez-Orive, Javon Knox, Zhizhong Chen, Yan Zhou, Drake Beery, et al. Suppressed phase separation of mixed-halide perovskites confined in endotaxial matrices. *Nature communications*, 10(1):1–7, 2019.

[24] Gergely F Samu, Csaba Janáky, and Prashant V Kamat. A victim of halide ion segregation. how light soaking affects solar cell performance of mixed halide lead perovskites. *ACS Energy Letters*, 2(8):1860–1861, 2017.

[25] Michael C Brennan, Sergiu Draguta, Prashant V Kamat, and Masaru Kuno. Light-induced anion phase segregation in mixed halide perovskites. *ACS Energy Letters*, 3(1):204–213, 2017.

[26] Seog Joon Yoon, Masaru Kuno, and Prashant V Kamat. Shift happens. how halide ion defects influence photoinduced segregation in mixed halide perovskites. *ACS Energy Letters*, 2(7):1507–1514, 2017.

[27] Wei Li, Mathias Uller Rothmann, Amelia Liu, Ziyu Wang, Yupeng Zhang, Alexander R Pascoe, Jianfeng Lu, Liangcong Jiang, Yu Chen, Fuzhi Huang, et al. Phase segregation enhanced ion movement in efficient inorganic cspbibr2 solar cells. *Advanced Energy Materials*, 7(20):1700946, 2017.

[28] Ute B Cappel, Sebastian Svanstrom, Valeria Lanzilotto, Fredrik OL Johansson, Kerttu Aitola, Bertrand Philippe, Erika Giangrisostomi, Ruslan Ovsyannikov, Torsten Leitner, Alexander Fohlisch, et al. Partially reversible photoinduced chemical changes in a mixed-ion perovskite material for solar cells. *ACS applied materials & interfaces*, 9(40):34970–34978, 2017.

[29] Anthony Ruth, Michael C Brennan, Sergiu Draguta, Yurii V Morozov, Maksym Zhukovskyi, Boldizsar Janko, Peter Zapol, and Masaru Kuno. Vacancy-mediated anion photosegregation kinetics in mixed halide hy-

brid perovskites: coupled kinetic monte carlo and optical measurements. *ACS Energy Letters*, 3(10):2321–2328, 2018.

[30] Alex J Barker, Aditya Sadhanala, Felix Deschler, Marina Gandini, Satyaprasad P Senanayak, Phoebe M Pearce, Edoardo Mosconi, Andrew J Pearson, Yue Wu, Ajay Ram Srimath Kandada, et al. Defect-assisted photoinduced halide segregation in mixed-halide perovskite thin films. *ACS Energy Letters*, 2(6):1416–1424, 2017.

[31] Zhen Li, Mengjin Yang, Ji-Sang Park, Su-Huai Wei, Joseph J Berry, and Kai Zhu. Stabilizing perovskite structures by tuning tolerance factor: formation of formamidinium and cesium lead iodide solid-state alloys. *Chemistry of Materials*, 28(1):284–292, 2016.

[32] Nam-Gyu Park. Halide perovskite photovoltaics: History, progress, and perspectives. *MRS Bulletin*, 43(7):527–533, 2018.

[33] Giles E Eperon, Samuel D Stranks, Christopher Menelaou, Michael B Johnston, Laura M Herz, and Henry J Snaith. Formamidinium lead trihalide: a broadly tunable perovskite for efficient planar heterojunction solar cells. *Energy & Environmental Science*, 7(3):982–988, 2014.

[34] H El-Ghtami, A Laref, and S Laref. Electronic and optical behaviors of methylammonium and formamidinium lead trihalide perovskite materials. *Journal of Materials Science: Materials in Electronics*, 30(1):711–720, 2019.

[35] Yiting Liu, Haizhou Lu, Jiaxin Niu, Huotian Zhang, Shitao Lou, Chunlei Gao, Yiqiang Zhan, Xiaolei Zhang, Qingyuan Jin, and Lirong Zheng. Temperature-dependent photoluminescence spectra and decay dynamics of mapbbr3 and mapbi3 thin films. *AIP Advances*, 8(9):095108, 2018.

[36] Yucheng Liu, Zhou Yang, and Shengzhong Liu. Recent progress in single-crystalline perovskite research including crystal preparation, property evaluation, and applications. *Advanced Science*, 5(1):1700471, 2018.

[37] Marcel Aebli, Laura Piveteau, Olga Nazarenko, Bogdan M Benin, Franziska Krieg, René Verel, and Maksym V Kovalenko. Lead-halide

scalar couplings in 207pb nmr of apbx3 perovskites (a= cs, methylammonium, formamidinium; x= cl, br, i). *Scientific reports*, 10(1):1–9, 2020.

[38] Jun Hong Noh, Sang Hyuk Im, Jin Hyuck Heo, Tarak N Mandal, and Sang Il Seok. Chemical management for colorful, efficient, and stable inorganic–organic hybrid nanostructured solar cells. *Nano letters*, 13(4):1764–1769, 2013.

[39] Constantinos C Stoumpos and Mercouri G Kanatzidis. The renaissance of halide perovskites and their evolution as emerging semiconductors. *Accounts of chemical research*, 48(10):2791–2802, 2015.

[40] Alexander J Knight, Jay B Patel, Henry J Snaith, Michael B Johnston, and Laura M Herz. Trap states, electric fields, and phase segregation in mixed-halide perovskite photovoltaic devices. *Advanced Energy Materials*, 10(9):1903488, 2020.

[41] Se-Yun Kim, Weon-Sik Chae, Yong-Jae Na, Sang-Hyub Kim, Sangwook Lee, Joon-Hyung Lee, and Young-Woo Heo. Excitation dynamics of mapb (i1-xbrx) 3 during phase separation by photoirradiation: Evidence of sink, band filling, and br-rich phase coarsening. *Journal of Alloys and Compounds*, 806:1180–1187, 2019.

[42] Zhibin Yang, Adharsh Rajagopal, Sae Byeok Jo, Chu-Chen Chueh, Spencer Williams, Chun-Chih Huang, John K Katahara, Hugh W Hillhouse, and Alex K-Y Jen. Stabilized wide bandgap perovskite solar cells by tin substitution. *Nano letters*, 16(12):7739–7747, 2016.

[43] Carolin M Sutter-Fella, Quynh P Ngo, Nicola Cefarin, Kira L Gardner, Nobumichi Tamura, Camelia V Stan, Walter S Drisdell, Ali Javey, Francesca M Toma, and Ian D Sharp. Cation-dependent light-induced halide demixing in hybrid organic–inorganic perovskites. *Nano letters*, 18(6):3473–3480, 2018.

[44] Joseph S Manser and Prashant V Kamat. Band filling with free charge carriers in organometal halide perovskites. *Nature Photonics*, 8(9):737–743, 2014.

[45] Kevin G Stamplecoskie, Joseph S Manser, and Prashant V Kamat. Dual nature of the excited state in organic–inorganic lead halide perovskites. *Energy & Environmental Science*, 8(1):208–215, 2015.

[46] Guichuan Xing, Nripan Mathews, Shuangyong Sun, Swee Sien Lim, Yeng Ming Lam, Michael Grätzel, Subodh Mhaisalkar, and Tze Chien Sum. Long-range balanced electron-and hole-transport lengths in organic-inorganic ch3nh3pbi3. *Science*, 342(6156):344–347, 2013.

[47] Miao Hu, Cheng Bi, Yongbo Yuan, Yang Bai, and Jinsong Huang. Stabilized wide bandgap mapbbrxi3–x perovskite by enhanced grain size and improved crystallinity. *Advanced Science*, 3(6):1500301, 2016.

[48] The Duong, Hemant Kumar Mulmudi, YiLiang Wu, Xiao Fu, Heping Shen, Jun Peng, Nandi Wu, Hieu T Nguyen, Daniel Macdonald, Mark Lockrey, et al. Light and electrically induced phase segregation and its impact on the stability of quadruple cation high bandgap perovskite solar cells. *ACS applied materials & interfaces*, 9(32):26859–26866, 2017.

[49] Klara Suchan, Justus Just, Pascal Becker, Carolin Rehermann, Aboma Merdasa, Roland Mainz, Ivan G Scheblykin, and Eva Unger. Multistage phase-segregation of mixed halide perovskites under illumination: A quantitative comparison of experimental observations and thermodynamic models. *arXiv preprint arXiv:2205.10867*, 2022.

[50] Connor G Bischak, Erin M Sanehira, Jake T Precht, Joseph M Luther, and Naomi S Ginsberg. Heterogeneous charge carrier dynamics in organic–inorganic hybrid materials: nanoscale lateral and depth-dependent variation of recombination rates in methylammonium lead halide perovskite thin films. *Nano letters*, 15(7):4799–4807, 2015.

[51] Letian Dou, Andrew B Wong, Yi Yu, Minliang Lai, Nikolay Kornienko, Samuel W Eaton, Anthony Fu, Connor G Bischak, Jie Ma, Tina Ding, et al. Atomically thin two-dimensional organic-inorganic hybrid perovskites. *Science*, 349(6255):1518–1521, 2015.

[52] Chuanxiao Xiao, Zhen Li, Harvey Guthrey, John Moseley, Ye Yang, Sarah Wozny, Helio Moutinho, Bobby To, Joseph J Berry, Brian Gorman, et al. Mechanisms of electron-beam-induced damage in perovskite

thin films revealed by cathodoluminescence spectroscopy. *The Journal of Physical Chemistry C*, 119(48):26904–26911, 2015.

[53] Dane W Dequilettes, Kyle Frohna, David Emin, Thomas Kirchartz, Vladimir Bulovic, David S Ginger, and Samuel D Stranks. Charge-carrier recombination in halide perovskites: Focus review. *Chemical reviews*, 119(20):11007–11019, 2019.

[54] Michael B Johnston and Laura M Herz. Hybrid perovskites for photovoltaics: charge-carrier recombination, diffusion, and radiative efficiencies. *Accounts of chemical research*, 49(1):146–154, 2016.

[55] Jiajun Qin, Xiao-Ke Liu, Chunyang Yin, and Feng Gao. Carrier dynamics and evaluation of lasing actions in halide perovskites. *Trends in Chemistry*, 3(1):34–46, 2021.

[56] Waqaas Rehman, David P McMeekin, Jay B Patel, Rebecca L Milot, Michael B Johnston, Henry J Snaith, and Laura M Herz. Photovoltaic mixed-cation lead mixed-halide perovskites: links between crystallinity, photo-stability and electronic properties. *Energy & Environmental Science*, 10(1):361–369, 2017.

[57] Hoang X Dang, Kai Wang, Masoud Ghasemi, Ming-Chun Tang, Michele De Bastiani, Erkan Aydin, Emilie Dauzon, Dounya Barrit, Jun Peng, Detlef-M Smilgies, et al. Multi-cation synergy suppresses phase segregation in mixed-halide perovskites. *Joule*, 3(7):1746–1764, 2019.

[58] Yang Zhou, Yong-Heng Jia, Hong-Hua Fang, Maria Antonietta Loi, Fang-Yan Xie, Li Gong, Min-Chao Qin, Xin-Hui Lu, Ching-Ping Wong, and Ni Zhao. Composition-tuned wide bandgap perovskites: From grain engineering to stability and performance improvement. *Advanced Functional Materials*, 28(35):1803130, 2018.

[59] Eline M Hutter, Loreta A Muscarella, Francesca Wittmann, Jan Versluis, Lucie McGovern, Huib J Bakker, Young-Won Woo, Young-Kwang Jung, Aron Walsh, and Bruno Ehrler. Thermodynamic stabilization of mixed-halide perovskites against phase segregation. *Cell Reports Physical Science*, 1(8):100120, 2020.

[60] Jixian Xu, Caleb C Boyd, Zhengshan J Yu, Axel F Palmstrom, Daniel J Witter, Bryon W Larson, Ryan M France, Jérémie Werner, Steven P Harvey, Eli J Wolf, et al. Triple-halide wide–band gap perovskites with suppressed phase segregation for efficient tandems. *Science*, 367(6482):1097–1104, 2020.

[61] Mojtaba Abdi-Jalebi, Zahra Andaji-Garmaroudi, Stefania Cacovich, Camille Stavrakas, Bertrand Philippe, Johannes M Richter, Mejd Alsari, Edward P Booker, Eline M Hutter, Andrew J Pearson, et al. Maximizing and stabilizing luminescence from halide perovskites with potassium passivation. *Nature*, 555(7697):497–501, 2018.

[62] R Geetha Balakrishna, Steven M Kobosko, and Prashant V Kamat. Mixed halide perovskite solar cells. consequence of iodide treatment on phase segregation recovery. *ACS Energy Letters*, 3(9):2267–2272, 2018.

[63] Simon A Bretschneider, Jonas Weickert, James A Dorman, and Lukas Schmidt-Mende. Research update: physical and electrical characteristics of lead halide perovskites for solar cell applications. *APL Materials*, 2(4):155204, 2014.

[64] Simone Meloni, Thomas Moehl, Wolfgang Tress, Marius Franckevičius, Michael Saliba, Yong Hui Lee, Peng Gao, Mohammad Khaja Nazeeruddin, Shaik Mohammed Zakeeruddin, Ursula Rothlisberger, et al. Ionic polarization-induced current–voltage hysteresis in ch3nh3pbx3 perovskite solar cells. *Nature communications*, 7(1):1–9, 2016.

[65] Junichiro Mizusaki, Kimiyasu Arai, and Kazuo Fueki. Ionic conduction of the perovskite-type halides. *Solid State Ionics*, 11(3):203–211, 1983.

[66] Tae-Youl Yang, Giuliano Gregori, Norman Pellet, Michael Grätzel, and Joachim Maier. The significance of ion conduction in a hybrid organic–inorganic lead-iodide-based perovskite photosensitizer. *Angewandte Chemie*, 127(27):8016–8021, 2015.

[67] Jon M Azpiroz, Edoardo Mosconi, Juan Bisquert, and Filippo De Angelis. Defect migration in methylammonium lead iodide and its role in perovskite solar cell operation. *Energy & Environmental Science*, 8(7):2118–2127, 2015.

[68] Zehua Chen, Geert Brocks, Shuxia Tao, and Peter A Bobbert. Unified theory for light-induced halide segregation in mixed halide perovskites. *Nature communications*, 12(1):1–10, 2021.

[69] A Sher, Mark van Schilfgaarde, An-Ban Chen, and William Chen. Quasi-chemical approximation in binary alloys. *Physical Review B*, 36(8):4279, 1987.

[70] Martin A Green, Anita Ho-Baillie, and Henry J Snaith. The emergence of perovskite solar cells. *Nature photonics*, 8(7):506–514, 2014.

[71] Nakita K Noel, Samuel D Stranks, Antonio Abate, Christian Wehrenfennig, Simone Guarnera, Amir-Abbas Haghighirad, Aditya Sadhanala, Giles E Eperon, Sandeep K Pathak, Michael B Johnston, et al. Lead-free organic–inorganic tin halide perovskites for photovoltaic applications. *Energy & Environmental Science*, 7(9):3061–3068, 2014.

[72] Samuel D Stranks and Henry J Snaith. Metal-halide perovskites for photovoltaic and light-emitting devices. *Nature nanotechnology*, 10(5):391–402, 2015.

[73] Nam Joong Jeon, Jun Hong Noh, Woon Seok Yang, Young Chan Kim, Seungchan Ryu, Jangwon Seo, and Sang Il Seok. Compositional engineering of perovskite materials for high-performance solar cells. *Nature*, 517(7535):476–480, 2015.

[74] Tor Elmelund, Brian Seger, Masaru Kuno, and Prashant V Kamat. How interplay between photo and thermal activation dictates halide ion segregation in mixed halide perovskites. *ACS Energy Letters*, 5(1):56–63, 2019.

[75] Adam D Wright, Carla Verdi, Rebecca L Milot, Giles E Eperon, Miguel A Pérez-Osorio, Henry J Snaith, Feliciano Giustino, Michael B Johnston, and Laura M Herz. Electron–phonon coupling in hybrid lead halide perovskites. *Nature communications*, 7(1):1–9, 2016.

[76] Krzysztof Galkowski, Anatolie Mitioglu, Atsuhiko Miyata, Paulina Plochocka, Oliver Portugall, Giles E Eperon, Jacob Tse-Wei Wang, Thomas Stergiopoulos, Samuel D Stranks, Henry J Snaith, et al. Determination

of the exciton binding energy and effective masses for methylammonium and formamidinium lead tri-halide perovskite semiconductors. *Energy & Environmental Science*, 9(3):962–970, 2016.

[77] George Whitfield and Peter B Shaw. Interaction of electrons with acoustic phonons via the deformation potential in one dimension. *Physical Review B*, 14(8):3346, 1976.

[78] Jarvist M Frost, Keith T Butler, Federico Brivio, Christopher H Hendon, Mark Van Schilfgaarde, and Aron Walsh. Atomistic origins of high-performance in hybrid halide perovskite solar cells. *Nano letters*, 14(5):2584–2590, 2014.

[79] Adrian Francisco-Lopez, Bethan Charles, M Isabel Alonso, Miquel Garriga, Mariano Campoy-Quiles, Mark T Weller, and Alejandro R Goñi. Phase diagram of methylammonium/formamidinium lead iodide perovskite solid solutions from temperature-dependent photoluminescence and raman spectroscopies. *The Journal of Physical Chemistry C*, 124(6):3448–3458, 2020.

[80] M Ibrahim Dar, Gwénolé Jacopin, Simone Meloni, Alessandro Mattoni, Neha Arora, Ariadni Boziki, Shaik Mohammed Zakeeruddin, Ursula Rothlisberger, and Michael Grätzel. Origin of unusual bandgap shift and dual emission in organic-inorganic lead halide perovskites. *Science advances*, 2(10):e1601156, 2016.

[81] Sheng Chen, Xiaoming Wen, Shujuan Huang, Fuzhi Huang, Yi-Bing Cheng, Martin Green, and Anita Ho-Baillie. Light illumination induced photoluminescence enhancement and quenching in lead halide perovskite. *Solar Rrl*, 1(1):1600001, 2017.

[82] Alessandro Senocrate, Tolga Acartürk, Gee Yeong Kim, Rotraut Merkle, Ulrich Starke, Michael Grätzel, and Joachim Maier. Interaction of oxygen with halide perovskites. *Journal of Materials Chemistry A*, 6(23):10847–10855, 2018.

[83] Sushu Wan, Yajie Zhu, Daocheng Hong, and Yuxi Tian. Controllable introduction of surface defects on ch3nh3pbi3 perovskite. *Nanomaterials*, 12(6):1002, 2022.

[84] Preethi Susan Mathew, Gergely F Samu, Csaba Janáky, and Prashant V Kamat. Iodine (i) expulsion at photoirradiated mixed halide perovskite interface. should i stay or should i go? *ACS Energy Letters*, 5(6):1872–1880, 2020.

[85] Gergely F Samu, Ádám Balog, Filippo De Angelis, Daniele Meggiolaro, Prashant V Kamat, and Csaba Janáky. Electrochemical hole injection selectively expels iodide from mixed halide perovskite films. *Journal of the American Chemical Society*, 141(27):10812–10820, 2019.

[86] Gergely F Samu and Csaba Janaky. Photocorrosion at irradiated perovskite/electrolyte interfaces. *Journal of the American Chemical Society*, 142(52):21595–21614, 2020.